A&A, 687, A163 (2024)
https://doi.org/10.1051/0004-6361/202347856

Astronomy & Astrophysics

ALMA-IMF

XI. The sample of hot core candidates: A rich population of young high-mass protostars unveiled by the emission of methyl formate

M. Bonfand[1,2], T. Csengeri[2], S. Bontemps[2], N. Brouillet[2], F. Motte[3], F. Louvet[3], A. Ginsburg[4], N. Cunningham[3], R. Galván-Madrid[5], F. Herpin[2], F. Wyrowski[6], M. Valeille-Manet[2], A. M. Stutz[7,8], J. Di Francesco[9], A. Gusdorf[10,11], M. Fernández-López[12], B. Lefloch[2], H-L. Liu[7,13], P. Sanhueza[14,15], R. H. Álvarez-Gutiérrez[7], F. Olguin[16], T. Nony[5], A. Lopez-Sepulcre[3,17], P. Dell'Ova[10,11], Y. Pouteau[3], D. Jeff[4], H.-R. V. Chen[16], M. Armante[10,11], A. Towner[18], L. Bronfman[19], and N. Kessler[2]

(Affiliations can be found after the references)

Received 1 September 2023 / Accepted 22 February 2024

ABSTRACT

Context. The star formation process leads to an increased chemical complexity in the interstellar medium. Sites associated with high-mass star and cluster formation exhibit a so-called hot core phase, characterized by high temperatures and column densities of complex organic molecules.

Aims. We aim to systematically search for and identify a sample of hot cores toward the 15 Galactic protoclusters of the ALMA-IMF Large Program and investigate their statistical properties.

Methods. We built a comprehensive census of hot core candidates toward the ALMA-IMF protoclusters based on the detection of two CH_3OCHO emission lines at 216.1 GHz. We used the source extraction algorithm GExt2D to identify peaks of methyl formate (CH_3OCHO) emission, a complex species commonly observed toward sites of star formation. We performed a cross-matching with the catalog of thermal dust continuum sources from the ALMA-IMF 1.3 mm continuum data to infer their physical properties.

Results. We built a catalog of 76 hot core candidates with masses ranging from ~0.2 $M_\odot$ to ~80 $M_\odot$, of which 56 are new detections. A large majority of these objects, identified from methyl formate emission, are compact and rather circular, with deconvolved full width at half maximum (FWHM) sizes of ~2300 au on average. The central sources of two target fields show more extended, but still rather circular, methyl formate emission with deconvolved FWHM sizes of ~6700 au and 13 400 au. About 30% of our sample of methyl formate sources have core masses above 8 $M_\odot$ and range in size from ~1000 au to 13 400 au, which is in line with measurements of archetypical hot cores. The origin of the CH_3OCHO emission toward the lower-mass cores may be explained as a mixture of contributions from shocks or may correspond to objects in a more evolved state (i.e., beyond the hot core stage). We find that the fraction of hot core candidates increases with the core mass, suggesting that the brightest dust cores are all in the hot core phase.

Conclusions. Our results suggest that most of these compact methyl formate sources are readily explained by simple symmetric models, while collective effects from radiative heating and shocks from compact protoclusters are needed to explain the observed extended CH_3OCHO emission. The large fraction of hot core candidates toward the most massive cores suggests that they rapidly enter the hot core phase and that feedback effects from the forming protostar(s) impact their environment on short timescales.

Key words. astrochemistry – catalogs – stars: formation – stars: massive – ISM: molecules – submillimeter: ISM

1. Introduction

Star formation plays a key role in building the complex inventory of interstellar chemical species in various astronomical sources, which in turn serve as powerful diagnostic tools that can be used to study their surrounding environment (see, e.g., Jørgensen et al. 2020; Ceccarelli et al. 2022, and references therein). Through the observation of molecular emission lines, it is possible to investigate the still poorly constrained physical conditions and chemical processes that connect the different stages of star formation. In comparison to low-mass stars, the formation process of high-mass stars ($M_\star > 8\,M_\odot$) is less well understood (Tan et al. 2013; Motte et al. 2018a). The early evolutionary stage of high-mass star formation is expected to be short. For example, Motte et al. (2007) estimate a pre-stellar phase of $<10^4$ yr based on the core population in Cygnus-X, Bonfand et al. (2017) estimated a lifetime of 6×10^4 yr for the hot core phase in the Galactic center molecular cloud Sgr B2(N), and Csengeri et al. (2014) estimate $\sim 7.5 \times 10^4$ yr for the phase prior to the emergence of strong infrared emission, corresponding to stars of type B0 or earlier, based on the statistics of massive clumps uncovered by the ATLASGAL[1] survey. In addition, both mechanical and radiative feedback effects from already formed (proto)stars in a clustered environment further complicate the physical and chemical structure of high-mass star-forming regions. As a consequence, the evolutionary sequence for high-mass star formation remains inadequately

[1] The APEX Telescope Large Area Survey of the Galaxy; see https://atlasgal.mpifr-bonn.mpg.de

tested. Nevertheless, different observational signatures can be used to characterize the deeply embedded protostar, such as hot molecular cores as well as hyper-compact (HC-) and ultra-compact (UC-) HII regions that are exclusively associated with sites of high-mass star and cluster formation. HC- and UC-HII regions are characterized by free-free emission from ionized gas, which indicates a (proto)stellar mass >8–15 $M_\odot$ (Hosokawa & Omukai 2009). Free-free emission can also arise from an ionizing jet component (for a review, see, e.g., Anglada et al. 2018). Hot molecular cores are identified based on associations with a variety of complex organic molecules (COMs[2]), relatively high excitation temperatures (>100 K), high gas densities (n_{H_2} = 10^5–10^8 cm^{-3}), compact sizes (<0.1 pc), high bolometric luminosities (>10^4 $L_\odot$), and high core masses (10–1000 $M_\odot$; see, e.g., Kurtz et al. 2000; Cesaroni 2005; Bonfand et al. 2019).

The exact origin of COMs – be it grain-surface production (see, e.g., Garrod & Herbst 2006; Garrod 2013) or gas-phase production (see, e.g., Charnley et al. 1992; Balucani et al. 2015, 2018; Vasyunin & Herbst 2013) – is still strongly debated. However, over the past few decades, they have been detected and studied in great detail toward several prominent hot cores, such as the well-known Galactic center source SgrB2(N) (Belloche et al. 2013, 2016, 2019; Bonfand et al. 2017) and the nearby star-forming region Orion KL (Brouillet et al. 2015; Cernicharo et al. 2016; Tercero et al. 2018), where many of the first detections of interstellar molecules at radio and (sub)millimeter wavelengths were made (see McGuire 2022, and references therein). COMs have also been identified toward the low-mass counterparts of hot cores, so-called hot corinos (Bottinelli et al. 2004; Ceccarelli 2004), that are Class 0 protostars, such as NGC 1333-IRAS 2A and -IRAS 4A (Taquet et al. 2015) and IRAS 16293-2422 (Jørgensen et al. 2012; Richard et al. 2013). Regardless of where COMs are detected, their spectra carry information on the chemical and physical properties of their envelopes, their morphologies, and probably their evolutionary stages (see, e.g., Allen et al. 2018; Bonfand et al. 2019; Jørgensen et al. 2020; Gieser et al. 2021). Investigating the chemical composition of star-forming cores in different environments and at different evolutionary stages is crucial to understanding the formation and early evolution of high-mass stars as well as the pathways for the chemical enrichment of the star-forming gas.

Here we analyze observational data obtained with the Atacama Large Millimeter/submillimeter Array (ALMA) for the ALMA-IMF Large Program called "ALMA transforms our view of the origin of stellar masses" (Motte et al. 2022; Ginsburg et al. 2022, hereafter Paper I and Paper II, respectively). ALMA-IMF has uncovered a large population of star-forming cores over various evolutionary stages and galactic environments. It is a survey of 15 massive nearby Galactic protoclusters that aims to statistically investigate the properties of a large sample of star-forming cores to understand the link between the core mass function (CMF) and the initial mass function (IMF, Pouteau et al. 2022, 2023; Nony et al. 2023, hereafter Paper III Paper VI Paper V, respectively). The 15 target regions were identified based on the ATLASGAL survey (Schuller et al. 2009; Csengeri et al. 2014) and the Csengeri et al. (2017) catalog, which describes the 200 brightest clumps of the survey. They were selected to probe massive protoclusters at different evolutionary stages within a distance of 2–5.5 kpc. Paper I gives an overview of the selected targets; the ALMA-IMF protoclusters were classified into three types of regions based on the amount of dense gas in the cloud, which has potentially been impacted by HII region(s): (i) young protoclusters devoid of internal ionizing sources, (ii) intermediate protoclusters that harbor a few HC- or UC-HII regions, which are seen as small, localized bubbles of ionized gas, or (iii) evolved protoclusters that contain bright and extended HII regions and hence where gas removal has started. Some of the targeted clouds host several well-known high-mass star-forming regions associated with strong radio continuum emission originating from UC-HII regions, such as G008.67 (Hernández-Hernández et al. 2014), G010.62 (Liu et al. 2019; Law et al. 2021), G012.80 (Immer et al. 2014), G333.60 (Lo et al. 2015), W51-E (Mehringer 1994; Zhang et al. 1998; Ginsburg et al. 2016; Rivilla et al. 2017), and W51-IRS2 (Henkel et al. 2013). Other regions are known to harbor some of the brightest hot cores in the Galactic plane: G327.29 (Wyrowski et al. 2008; Bisschop et al. 2013, and references therein), G351.77 (Leurini et al. 2008), and the W51e1/e2 hot cores of the W51-E protocluster (Zhang & Ho 1997; Ginsburg et al. 2017). G328.25 is a well-studied hot core precursor that is isolated down to ~400 au scales (Csengeri et al. 2018, 2019; Bouscasse et al. 2022). Finally, Brouillet et al. (2022, hereafter, Paper IV) identified eight hot cores toward the young protocluster W43-MM1; it was studied as part of the pilot project (2013.1.01365.S) that served as a preparation for the ALMA-IMF Large Program.

With a ~6.7 GHz noncontinuous bandwidth, the ALMA-IMF data have already started to reveal the rich molecular content of several young star-forming cores. From a first-look analysis of the data, we show in Paper I that emission lines of COMs are detected over multiple spectral windows (spw) of the observational setup, suggesting that the dataset can be efficiently used to investigate the hot core phenomenon. Among the detected COMs within the ALMA-IMF band, we focus here on methyl formate (CH_3OCHO), which is commonly detected toward both low- and high-mass star-forming regions over a broad range of column densities. For instance, Coletta et al. (2020) investigated data obtained with the 30 m single-dish telescope of the Institut de Radioastronomie Millimétrique (IRAM 30 m) in three bands (3, 2, and 0.9 mm), toward 39 star-forming regions, and derived column densities for methyl formate ranging from ~4×10^{15} up to 4×10^{18} cm^{-2}.

In the current chemical models of hot cores, CH_3OCHO is formed at early times during the star formation process, primarily through solid-phase radical-addition reactions that occur at around 20–40 K (see, e.g., Garrod & Herbst 2006; Garrod et al. 2022). Experimental studies led by Ishibashi et al. (2021) show that methyl formate can also be formed efficiently on water ice at 10 K, via the photolysis of methanol. Then, radiative heating from the central protostar leads to the thermal sublimation of water ices from the grain surfaces. CH_3OCHO is released into the gas phase when the temperature reaches ~120 K (Garrod et al. 2022), and significant thermal desorption still occurs up to ~160 K (Bonfand et al. 2019; Garrod et al. 2022). Bouscasse et al. (2022, 2024), and Busch et al. (2022) have found increased abundances of several O-bearing COMs, including CH_3OCHO, at lower temperatures of $\lesssim$100 K toward Sgr B2(N1), the cold extended envelope of G328.25, and other infrared quiet massive clumps, suggesting that other desorption processes are at work below the thermal desorption temperature. One possible explanation proposed by Busch et al. (2022) is a partial thermal desorption of molecules from the outer, CO-rich layers of the ice mantles at the end of the cold collapse. Given its low binding energy, CO would desorb at much lower temperatures (20–30 K).

[2] Complex organic molecules are carbon-bearing molecules that are composed of at least six atoms (Herbst & van Dishoeck 2009).

Table 1. 15 massive protoclusters targeted by ALMA-IMF.

Field	Cube center [IRCS - J2000] RA[h:m:s]	Dec[°:′:″]	V_{LSR} [km s^{-1}]	d [kpc]	Evolutionary stage	M_{cloud} [$\times 10^3 M_\odot$]
G008.67	18:06:21.12	−21:37:16.7	+37.6	3.4	I	3.1
G010.62	18:10:28.80	−19:55:48.3	−2.0	5.0	E	6.7
G012.80	18:14:13.37	−17:55:45.2	+37.0	2.4	E	4.6
G327.29	15:53:08.13	−54:37:08.6	−45.0	2.5	Y	5.1
G328.25	15:57:59.68	−53:57:59.8	−43.0	2.5	Y	2.5
G333.60	16:22:09.36	−50:05:59.2	−47.0	4.2	E	12.0
G337.92	16:41:10.62	−47:08:02.9	−40.0	2.7	Y	2.5
G338.93	16:40:34.42	−45:41:40.6	−62.0	3.9	Y	7.1
G351.77	17:26:42.62	−36:09:20.5	−3.0	2.0	I	2.5
G353.41	17:30:26.28	−34:41:49.7	−17.0	2.0	I	2.5
W43-MM1	18:47:47.00	−01:54:26.0	+97.0	5.5	Y	13.4
W43-MM2	18:47:36.61	−02:00:51.7	+97.0	5.5	Y	11.6
W43-MM3	18:47:41.46	−02:00:28.2	+97.0	5.5	I	5.2
W51-E	19:23:44.18	+14:30:28.9	+55.0	5.4	I	32.7
W51-IRS2	19:23:39.81	+14:31:02.9	+55.0	5.4	E	20.6

Notes. The central positions of the mosaics are taken from the CH_3OCHO cube headers. The rest velocities (V_{LSR}), distances to the Sun (d), evolutionary stages (Young, Intermediate, Evolved), and cloud mass (M_{cloud}) computed from the 870 μm integrated flux, are from Paper I.

As a result, COMs that are also abundant in these layers may be able to co-desorb at temperatures <100 K. Once the upper layers, which are rich in CO, desorb along with some COMs, COMs would still be present in the water-rich layers beneath, to be released at higher temperatures when water ice desorbs. Burke et al. (2015) undertook detailed experimental studies and show that methyl formate can also desorb from ices as a pure desorption feature; therefore, in typical hot core conditions it would desorb at lower temperatures, starting at 77 K, or 108 K for mixed ices (i.e., methyl formate:H_2O ices).

Methyl formate has also been observed in the cold gas phase toward pre-stellar cores and other cold environments (Bacmann et al. 2012; Cernicharo et al. 2012; Vastel et al. 2014), suggesting that low-temperature mechanisms are needed to explain the presence of CH_3OCHO in the gas phase. The UV-driven photo desorption of surface molecules was shown to have only a limited ability to desorb molecules at visual extinction values >1 under the assumption of the standard interstellar radiation field and cosmic-ray ionization rate (Jin & Garrod 2020). On the other hand, chemical desorption (i.e., desorption induced by the release of chemical energy upon the formation of a molecule; Garrod et al. 2007) is able to drive substantial COM desorption at low temperatures. Balucani et al. (2015) show that CH_3OCHO can also efficiently form via the gas-phase oxidation of CH_3OCH_2. This reaction does not have an activation barrier, and it is triggered by a series of gas-phase reactions following the nonthermal desorption (i.e., cosmic-ray-induced heating of grains and/or chemical desorption; Hasegawa & Herbst 1993; Garrod et al. 2007, respectively) of solid-phase methanol, meaning it may be efficient even at low temperatures. Finally, several O-bearing COMs, including methyl formate, have been detected in accretion shocks toward both high-mass (Csengeri et al. 2018, 2019) and low-mass objects (Imai et al. 2022). In addition, methyl formate has been detected toward shocks related to outflow activity by Palau et al. (2017). In these cases, sputtering may play a role in breaking the grains and liberating CH_3OCHO into the gas phase.

In the present paper we aim to systematically identify intermediate- to high-mass protostars associated with emission from CH_3OCHO toward the 15 ALMA-IMF protoclusters. Our goal is to provide a catalog of hot core candidates from various cloud environments that are undergoing different dynamical events (e.g., gas inflow, protostellar outflows, and expanding HII regions). In Sect. 2 we present the observational data and the continuum core catalog used for our analysis. The method for identifying and extracting the hot core candidates from the ALMA-IMF data is described in Sect. 3, and the resulting catalog of hot core candidates is presented in Sect. 4. In Sect. 5 we derive the physical properties of the hot core candidates, and the chemical origin of the methyl formate emission, as well as the exact nature of the sources, is discussed in Sect. 6. Finally, our results are summarized in Sect. 7. Additional material, such as the spectra extracted toward the hot core candidates, the continuum maps, the $H_{41\alpha}$ maps, and detailed explanations of the methods for estimating the free-free contamination and for deconvolving beam sizes are provided in Appendices A–E.

2. Observations and core catalogs

The ALMA-IMF Large Program (2017.1.01355.L, PIs: Motte, Ginsburg, Louvet, Sanhueza) was undertaken to image 15 of the most massive Galactic protoclusters over the same physical scale, sensitivity, and spectral coverage, allowing for a homogeneous characterization of these star-forming regions. The overview of the scientific goals of the ALMA-IMF program, and the target selection is described in Paper I; the detailed description of the observing setup, data reduction pipeline, and the subsequent data quality assessment is detailed in Paper II. The data reduction of the ALMA-IMF spw is described in Cunningham et al. (2023, hereafter, Paper VII).

2.1. Spectral line datacubes

The ALMA-IMF dataset consists of 15 mosaics covering a field of view of 1–8 pc^2 obtained with the ALMA 12-m array. Table 1 provides an overview of the 15 targeted protoclusters, with the cube centers, the rest velocities (V_{LSR}) of the protoclusters, their distances to the Sun and their evolutionary stages. The full spectral setup is composed of 12 spw: eight at 1.3 mm

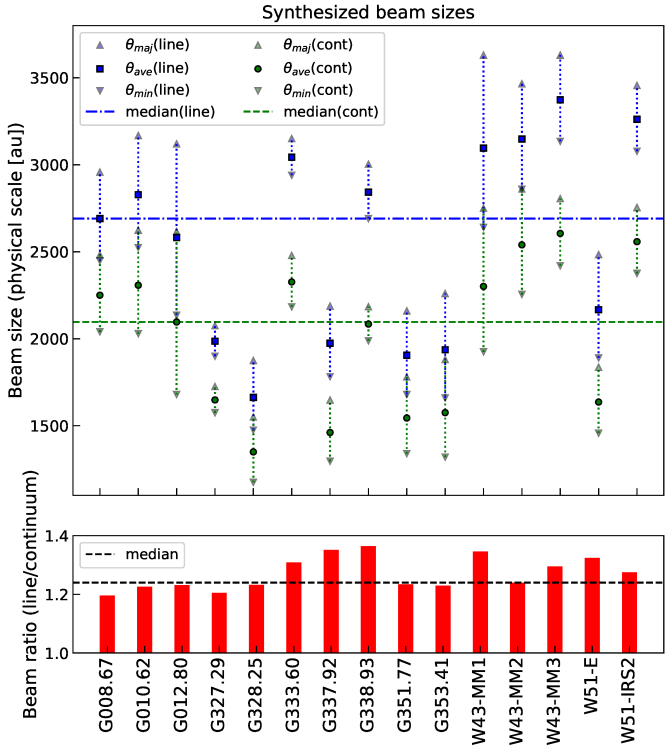

Fig. 1. Comparison of line cube and continuum map synthesized beam sizes for the 15 ALMA-IMF fields. (Top panel) Line cube and continuum map synthesized beam sizes are shown in blue and green, respectively. For each field, the average beam size is defined as $\theta_{\rm ave} = \sqrt{\theta_{\rm maj} \times \theta_{\rm min}}$, where $\theta_{\rm maj}$ and $\theta_{\rm min}$ are expressed in physical scales (au). The horizontal dashed blue and green lines show the median beam sizes for the 15 line cubes and continuum maps, respectively. (Bottom panel) Ratio of the average line cube to continuum map beam size for the 15 ALMA-IMF fields. The horizontal dashed line shows the median.

(ALMA band 6, hereafter B6) and four at 3 mm (ALMA band 3, hereafter B3), which represent a ∼6.7 GHz noncontinuous bandwidth per protocluster. The detailed characteristics of these 12 spw are given in Table 2 of Paper I, including an overview of the main spectral lines they cover. In Paper VII we provide the full spectral line data products for the 15 protoclusters. They were produced using the custom ALMA-IMF imaging pipeline[3] originally developed to process the continuum data as described in Paper II, and subsequently adapted to process the spectral line datacubes as described in Paper VII. In short, up to two different ALMA 12-m array configurations were combined in the uv-plane for each field, and corrected for system temperature and spectral data normalization (see Section 2 of Paper II for more details). Then, the pipeline performs a line cleaning with parameters optimized for each field, and applies the Jorsater-van-Moorsel (JvM; Jorsater & van Moorsel 1995) correction. The deconvolved datacubes have a constant beam over all the channels. Finally, we used the STATCONT software (Sánchez-Monge et al. 2018) with the sigma-clipping algorithm to systematically remove the continuum emission in the image plane and produce datacubes containing only spectral line emission.

In the present paper, we focus our analysis on the 234 MHz-wide spw centered on 216.2 GHz, at 1.3 mm (B6–spw0), which contains four strong emission lines of methyl formate, as well as DCO^+ (3–2) and $OC^{33}S$ (18–17), with a spectral resolution of 0.17 km s^{-1} (i.e., 122 kHz). The angular resolution of the observations was chosen to achieve a physical resolution of about 2500 au for each individual protocluster considering their different distances. The resulting angular resolution of the B6–spw0 line cubes, using a robust weighting of 0, ranges from ∼0.4″ to 1.1″, depending on the distance of the protocluster. The synthesized beams of the datacubes, given by the geometric mean of the major and minor axes ($\theta_{\rm ave} = \sqrt{\theta_{\rm maj} \times \theta_{\rm min}}$), are shown in Fig. 1 and listed in Table 2. The flux densities, S, measured per beam (in Jy beam^{-1}) in the datacubes are converted to effective brightness temperatures ($T_{\rm B}$, in K) as follows:

$$T_{\rm B}\,[{\rm K}] = S\,[{\rm Jy\,beam^{-1}}] \times \frac{c^2}{2k_{\rm b}\nu^2} \times \frac{1}{\Omega_{\rm beam}}, \quad (1)$$

where c is the speed of light, $k_{\rm b}$ is the Boltzmann constant, ν the central frequency of the considered spw (see Table 2), and $\Omega_{\rm beam}$ the beam solid angle of the line cubes given by $\Omega_{\rm beam} = \theta^2_{\rm ave} \times \frac{\pi}{4ln(2)}$. Finally, in order to estimate the noise in a homogeneous manner, we used the line cubes prior to the correction for the primary beam response. For each field, we measured the rms noise within a polygon that is defined as a region devoid of emission. The rms noise levels estimated in this way are given in Table 2 in units of mJy per clean beam and K.

The ALMA-IMF spectral coverage includes other potential tracers of heated gas, such as high $E_{\rm up}/k$ transitions of CH_3OH and CH_3CN lines. However, several of their transitions exhibit a considerably more extended morphology and hence provide a potentially more confused view of hot cores compared to that of the selected spectrally well-resolved CH_3OCHO lines (see Paper IV). A more detailed comparison of these tracers will be subject for further studies.

2.2. Continuum maps and core catalogs

The first data release of the ALMA-IMF continuum images at 1.3 mm and 3 mm, along with a complete description of the data reduction and imaging process, are presented in Paper II. The exact central frequency of the 1.3 and the 3 mm continuum maps, along with the average synthesized beam sizes are given for each field in Table 2. Figure 1 shows that the average synthesized beam size of the line cubes is systematically larger than that of the continuum maps at 1.3 mm, with a median ratio (line cube over continuum map beam) of ∼1.24, and a difference ranging from 20% to 36%, depending on the protocluster.

Louvet et al. (2024, hereafter, Paper XII) present the catalogs of dust continuum cores extracted from the continuum images at 1.3 mm, computed using maps that consider only the line-free channels, also referred to as "cleanest" maps. Two sets of cleanest continuum maps were used for the source extraction: the continuum maps at their native angular resolution (1400–2700 au), also referred to as unsmoothed data, and the continuum maps that were all smoothed to the same physical resolution of 2700 au; this implies a reduced angular resolution compared to the Briggs 0 weighted gridding of the spw used here. For the current analysis we focus exclusively on the unsmoothed continuum data, thus benefiting from the original angular resolution of the data. In Paper XII, the multi-scale source and filament extraction method "getsf" (Men'shchikov 2021) was used to separate the compact source-like peaks from their backgrounds, using spatial decomposition before extracting sources, that are defined as relatively round emission peaks, significantly stronger than the local surrounding fluctuations of background and noise. In total 807 compact continuum cores were extracted from the 15

[3] https://github.com/ALMA-IMF/reduction

Table 2. Observational characteristics of the B6-spw0 line cubes and the 1.3 and 3 mm continuum maps used in the present study.

	Line cubes				Continuum maps					
					1.3 mm			3 mm		
Protocluster name	$\theta_{maj} \times \theta_{min}$ [″ × ″]	PA [deg]	rms [mJy beam^{-1}]	[K]	$\theta_{maj} \times \theta_{min}$ [″ × ″]	PA [deg]	$\nu_{1.3mm}$ [GHz]	$\theta_{maj} \times \theta_{min}$ [″ × ″]	PA [deg]	ν_{3mm} [GHz]
G008.67	0.87 × 0.72	−82	8.6	0.36	0.73 × 0.60	−82	228.732	0.51 × 0.40	+72	100.526
G010.62	0.64 × 0.51	−74	2.4	0.19	0.53 × 0.41	−78	229.268	0.39 × 0.32	−80	100.704
G012.80	1.30 × 0.89	+77	13.2	0.30	1.09 × 0.70	+75	229.080	1.48 × 1.26	+89	100.680
G327.29	0.83 × 0.76	−53	10.0	0.41	0.69 × 0.63	−41	229.507	0.43 × 0.37	+70	101.776
G328.25	0.75 × 0.59	−13	16.7	0.99	0.62 × 0.47	−112	227.575	0.62 × 0.44	−83	101.500
G333.60	0.75 × 0.70	−37	3.4	0.17	0.59 × 0.52	−33	229.062	0.46 × 0.44	+50	100.756
G337.92	0.81 × 0.66	−51	4.2	0.21	0.61 × 0.48	−56	227.503	0.46 × 0.41	+78	101.602
G338.93	0.77 × 0.69	+80	4.0	0.20	0.56 × 0.51	−85	229.226	0.41 × 0.39	+84	100.882
G351.77	1.08 × 0.84	+88	15.1	0.44	0.89 × 0.67	+87	227.991	1.52 × 1.30	+89	100.228
G353.41	1.13 × 0.83	+86	15.3	0.43	0.94 × 0.66	+85	229.431	1.46 × 1.27	+77	100.547
W43-MM1	0.66 × 0.48	−81	2.2	0.18	0.50 × 0.35	−77	229.680	0.56 × 0.34	−73	99.795
W43-MM2	0.63 × 0.52	−80	2.1	0.17	0.52 × 0.41	−76	227.597	0.31 × 0.24	−72	101.017
W43-MM3	0.66 × 0.57	+86	2.3	0.16	0.51 × 0.44	+90	228.931	0.41 × 0.29	−83	100.911
W51-E	0.46 × 0.35	+30	2.1	0.34	0.34 × 0.27	+26	228.918	0.29 × 0.27	+71	101.426
W51-IRS2	0.64 × 0.57	−19	2.3	0.16	0.51 × 0.44	−26	228.530	0.29 × 0.27	−57	101.263

Notes. The synthesized beam sizes are read from the header of the line cubes and continuum maps (see Paper I, Paper II, and Paper VII). The central frequencies of the continuum maps, $\nu_{1.3mm}$ and ν_{3mm}, are from Paper XII. The rms noise level is measured in the JvM-corrected cubes in units of mJy per clean beam, for channels that are free of strong emission, and within a subregion that is free of thermal emission. See Paper VII for more details on how to recover the noise in units of Jy per dirty beam.

ALMA-IMF protoclusters using getsf, including 140 sources that are largely contaminated by free-free emission, according to the spectral index calculations presented in Paper XII. The core catalogs can be found on the ALMA-IMF large program website[4] and in Paper XII.

3. Identification of hot core candidates

We present here a simple approach, independent from the continuum core identification, to extract hot core candidates toward the 15 massive protoclusters, based on the spatial distribution of a single COM, methyl formate (CH_3OCHO). A deeper search for hot cores using other spectral lines from the complete ALMA-IMF dataset will be presented in a forthcoming paper.

3.1. CH_3OCHO integrated intensity (moment 0) maps

The ALMA-IMF spectral setup covers four strong transitions of CH_3OCHO in its B6-spw0 at 216.2 GHz (see the exact rest frequencies listed in Table 3). The four transitions share the same upper level energy, E_{up}/k = 109 K, so they most likely trace the same region within the source envelope and also exhibit similar line profiles. Figure 2 shows the spectra observed between 216.08 and 216.32 GHz (i.e., 234 MHz wide), spatially averaged over the full field of view of the 15 ALMA-IMF fields. The four transitions of CH_3OCHO are gathered into two pairs of lines. The spectral resolution of 0.17 km s^{-1} is sufficient to resolve the lines with at least 11 channels, considering the full width at half maximum (FWHM) of the lines ranging between ∼2 and 6 km s^{-1}, depending on the protocluster. However, in each pair, the two transitions are separated by ∼5.7 km s^{-1}, meaning that, depending on the linewidth of each CH_3OCHO transition, they may be partially blended. Except in the case of G327.29, G351.77, and W51-E, the averaged spectrum shows a relatively low contamination from other molecules, such that CH_3OCHO lines are easy to identify.

In most cases, the two CH_3OCHO pairs have similar shapes and intensities. However, in the cases of G010.62, G012.80, G333.60, W43-MM1, W43-MM3, W51-E, and W51-IRS2, the first pair of CH_3OCHO lines, centered at 216.113 GHz, is strongly contaminated by the DCO^+ (3–2) line (see Table 3). Furthermore, most fields exhibit complex spectra, with multiple velocity features, which either may come from multiple sources detected in the field with different V_{LSR} (see the different rest velocities of the sources in Table 4) or result from multiple velocity components of CH_3OCHO spatially centered on the same core but slightly shifted in velocity. Therefore, we created moment 0 maps of methyl formate by integrating the spectral intensity over a broad velocity range of ∼35 km s^{-1} (i.e., 206 channels), which covers the CH_3OCHO pair of lines that is not contaminated by DCO^+ (see the vertical dashed lines in Fig. 2). This velocity range was selected as the best compromise to take into account that different sources may have different V_{LSR} (>10 km s^{-1} dispersion in the core V_{LSR}; see Fig. 2 of Paper VII, and also Sect. 3.4), and excluding emission from other species. In the case of G012.80 and W43-MM2, we used a custom, tighter, velocity range of ∼15 km s^{-1} (i.e., 88 channels) to increase the signal-to-noise ratio (S/N) of the very faint CH_3OCHO emission lines.

Figures 3–6 display the moment 0 maps of the methyl formate line pair 2 and shows that the emission from CH_3OCHO traces a diversity of structures across the 15 ALMA-IMF protoclusters. We can mainly distinguish two types of structures:

– Extended structures (>5000 au) that may contain one or more sources. This is the case of five ALMA-IMF protoclusters: G010.62, G327.29, G337.92, G351.77, and W51-E, two of which are young, two are intermediate, and one is evolved, according to Paper I. In the case of G010.62, G337.92, and G351.77, the methyl formate emission exhibits

[4] https://www.almaimf.com/

Table 3. Properties of the investigated transitions.

Species	Freq [MHz]	E_{up}/k [K]	A_{ij} [s^{-1}]	$J_{up}(K_a,K_c) - J_{low}(K_a,K_c)$
		Line pair 1		
CH_3OCHO, vt = 0	216 109.780	109.3	1.49×10^{-4}	19(2, 18) – 18(2, 17) E
DCO^+,v = 0	216 112.582	20.7	7.66×10^{-4}	3 – 2
CH_3OCHO, vt = 0	216 115.572	109.3	1.49×10^{-4}	19(2, 18) – 18(2, 17) A
		Line pair 2		
CH_3OCHO, vt = 0	216 210.906	109.3	1.49×10^{-4}	19(1, 18) – 18(1, 17) E
CH_3OCHO, vt = 0	216 216.539	109.3	1.49×10^{-4}	19(1, 18) – 18(1, 17) A

Notes. The spectroscopic predictions (frequencies, upper energy levels and Einstein coefficients) are taken from the JPL catalog (Pearson et al. 2010).

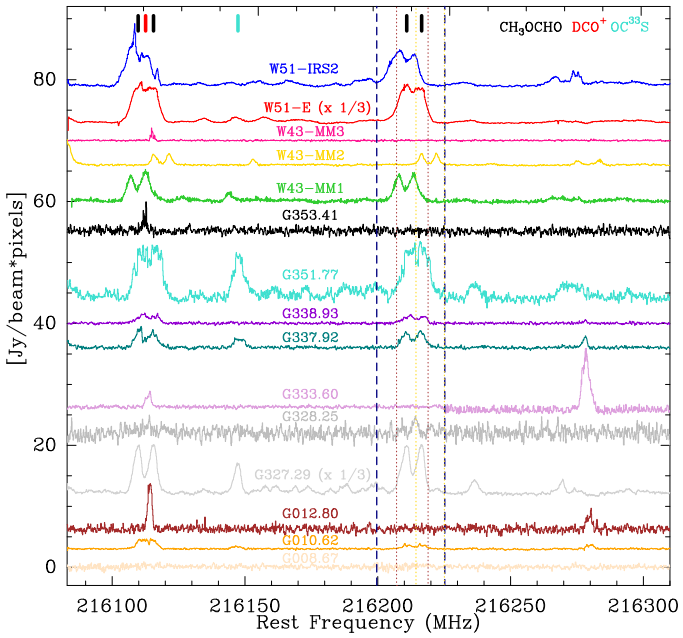

Fig. 2. Continuum-subtracted spectra integrated over the full field of view of the 15 ALMA-IMF B6-spw0 line cubes. The value in parentheses (if any) indicates the scaling factor applied to the spectrum. The vertical dashed dark blue lines show the channel range used to compute the moment 0 maps of methyl formate for all protoclusters except G012.80 and W43-MM2, for which tighter velocity ranges, shown with dotted brown and yellow lines, respectively, were used. The vertical colored bars on top of the plot show the rest frequencies of the corresponding species, indicated in the top-right corner.

a more complex spatial structure that is not axisymmetric (i.e., not circular).
– The ten other protoclusters harbor individual objects. They have rather compact, elliptical or circular emission, with an extent of a few thousand au, that may be clustered or isolated.

3.2. Source extraction

Given the large dataset used for this analysis, with varying dynamic range and morphology across the different fields, the method used for the source extraction must be as homogeneous and automatic as possible. Therefore, in order to extract in a systematic way compact and centrally peaked methyl formate sources from the 15 moment 0 maps, we used the source extraction algorithm "GExt2D" (Bontemps, in prep.), which is based on a Gaussian fitting of the strongest curvature points in intensity maps and optimized for compact source identification, similar to the CutEX algorithm of Molinari et al. (2011). The source extraction and characterization is made in two steps:

– In a first step, GExt2D computes the second derivative of the CH_3OCHO moment 0 map and looks for local maxima in the curvature map, which indicate the presence of compact sources, from which it extracts the coordinates of the central position.
– In the second step, source sizes (FWHM) and the peak values of the integrated intensity maps (Jy $beam^{-1}$ km s^{-1}) are measured for each individual source by fitting 2D Gaussians to its central position, in the primary-beam corrected CH_3OCHO moment 0 map.

In order to facilitate the source detection in the first step, we used the moment 0 maps prior to the correction for the primary beam response, which exhibit a homogeneous noise level in the entire field. However, since we cover some of the brightest Galactic protoclusters, some maps are affected by dynamic range limitations. This is particularly an issue for the G327.29 protocluster (see Fig. 3) and leads to a significantly larger average noise over the map, due to the central, brightest source being surrounded by strong sidelobes. In order to prevent GExt2D from detecting spurious sources (i.e., bright emission associated with strong sidelobes), we manually identified in each map a region in which the noise is the most representative of the whole field, which is different from the polygon we used to measure the rms noise level in the line cubes in Sect. 2.1. The source extraction starts with the strongest fluctuation in the map and proceeds to fainter fluctuations, finding local maxima down to noise-dominated curvature values. To be ultimately selected, a peak must be significant both in curvature and intensity. We set the detection threshold to a signal-to-noise ratio of 2.5, which is related to the local noise fluctuation in the curvature map. The detection thus stops when it reaches a $S/N = 2.5$ in curvature for a single pixel. We note that for the faintest sources, an offset of 1–2 pixels with respect to the real peak of emission may occur, which can be explained by an inhomogeneous noise distribution in the image or because of the background subtraction.

In order to remove spurious sources from our catalog, we visually inspected the single-pixel spectra extracted toward the peak position of all the sources identified with GExt2D. As some spectra may show strong fluctuations due to inhomogeneous noise or inaccurate continuum subtraction, only the sources for

Table 4. Catalog of the sources extracted from the moment 0 maps of methyl formate using the GExt2D algorithm.

ID	Name	RA[(a)] [h:m:s]	Dec[(a)] [°:′:″]	$S^{peak}_{MF^{(b)}}$ [mJy beam^{-1} km s^{-1}]	$S/N^{(c)}$	$\theta_{maj} \times \theta^{(d)}_{min}$ [″ × ″]	PA[(d)] [deg]	$\theta^{dec}_{maj} \times \theta^{dec(e)}_{min}$ [″ × ″]	$PA^{dec(e)}$ [deg]	$FWHM^{dec(f)}_{MF}$ [au]	$V^{(g)}_{LSR}$ [km s^{-1}]	%channels[(h)] [%]	Tentative classification[(i)]
						G008.67							
1	G008.67–MF1	18:06:19.01	−21:37:32.0	1696.2	35.9	1.11 × 0.88	85.2	_	_	1346.4	34.2 ± 0.1	13	HC*
2	G008.67–MF2	18:06:23.48	−21:37:10.5	850.9	25.6	1.12 × 0.87	107.8	_	_	1346.4	41.7 ± 0.1	8	
						G010.62							
1	G010.62–MF1	18:10:28.67	−19:55:49.2	745.7	28.3	1.12 × 0.87	93.9	0.99 × 0.59	−83.2	3811.5	−0.8 ± 0.1	18	
2	G010.62–MF2	18:10:28.70	−19:55:50.2	524.4	19.0	0.93 × 0.83	78.5	0.76 × 0.54	−88.8	3212.5	−3.2 ± 0.1	16	
3	G010.62–MF3	18:10:28.62	−19:55:49.3	391.6	12.7	0.77 × 0.69	126.5	0.57 × 0.28	−64.9	2019.6	1.6 ± 0.1	26	HC*
4	G010.62–MF4	18:10:28.66	−19:55:48.6	372.6	12.3	1.01 × 0.71	86.0	0.87 × 0.33	−89.6	2653.2	−0.9 ± 0.1	9	
5	G010.62–MF5	18:10:28.78	−19:55:49.5	321.9	14.7	1.34 × 0.96	93.0	1.24 × 0.73	−85.0	4727.2	−4.7 ± 0.1	6	
6	G010.62–MF6	18:10:28.61	−19:55:47.7	216.9	12.4	0.84 × 0.76	119.1	0.66 × 0.41	−67.7	2613.6	−4.1 ± 0.1	6	
7	G010.62–MF7	18:10:29.24	−19:55:40.9	117.0	10.8	0.67 × 0.49	97.2	0.44 × 0.40	−78.9	2098.7	−0.2 ± 0.6	7	
8	G010.62–MF8	18:10:28.79	−19:55:51.0	50.6	4.8	0.62 × 0.60	95.5	_	_	1415.6	−3.4 ± 0.2	4	
9	G010.62–MF9	18:10:28.74	−19:55:51.3	46.6	3.9	0.64 × 0.46	17.5	_	_	1415.6	−4.3 ± 0.2	4	
10	G010.62–MF10	18:10:29.11	−19:55:45.4	46.5	6.1	0.62 × 0.62	−0.7	_	_	1415.6	−6.2 ± 0.1	3	
						G012.80							
1	G012.80–MF1	18:14:11.83	−17:55:32.4	2439.2	107.0	1.37 × 1.04	73.3	1.04 × 0.77	75.1	2160.0	37.8 ± 0.3	12	HC*
2	G012.80–MF2	18:14:13.74	−17:55:21.4	427.2	22.8	1.55 × 1.18	73.9	1.27 × 0.54	75.2	1994.4	36.8 ± 0.4	5	HC*
3	G012.80–MF3	18:14:13.13	−17:55:40.2	282.6	17.3	2.13 × 1.42	62.4	1.93 × 0.61	66.1	2611.2	36.9 ± 0.2	3	
4	G012.80–MF4	18:14:11.63	−17:55:34.1	162.7	6.1	1.40 × 0.93	90.4	1.06 × 0.89	84.2	2340.0	37.7 ± 0.3	1	
						G327.29							
1	G327.29–MF1	15:53:07.79	−54:37:06.4	20680.0	_	2.85 × 2.71	70.1	2.73 × 2.59	74.1	6665.0	−43.5 ± 0.3	77	HC
2	G327.29–MF2	15:53:09.48	−54:37:01.1	455.6	9.6	0.82 × 0.77	−3.8	_	_	992.5	−46.7 ± 0.2	5	HC*
3	G327.29–MF3	15:53:10.89	−54:36:46.4	260.0	10.0	1.00 × 0.77	97.4	0.64 × 0.27	−76.9	1047.5	−45.2 ± 0.4	1	
						G328.25							
1	G328.25–MF1	15:57:59.80	−53:58:00.7	2596.9	_	1.42 × 1.02	−74.1	1.23 × 0.80	−68.2	2490.0	−40.0 ± 0.1	14	HC*
_	G328.25–shock1[(*)]	15:57:59.83	−53:58:00.7										shock
_	G328.25–shock2[(*)]	15:57:59.76	−53:58:00.8										shock
						G333.60							
1	G333.60–MF1	16:22:11.05	−50:05:56.5	406.7	21.5	0.94 × 0.82	49.4	0.56 × 0.43	47.4	2091.6	−52.7 ± 0.1	14	HC*
2	G333.60–MF2	16:22:08.55	−50:06:12.4	79.8	6.4	0.77 × 0.51	125.5	0.32 × 0.53	−51.4	1755.6	−46.1 ± 0.7	4	HC*
						G337.92							
1	G337.92–MF1	16:41:10.42	−47:08:03.5	4899.7	50.1	1.31 × 0.96	116.0	1.12 × 0.53	−61.1	2095.2	−40.4 ± 0.1	62	HC
2	G337.92–MF2	16:41:10.49	−47:08:02.5	2124.8	28.5	1.15 × 1.08	23.4	0.87 × 0.80	−32.3	2270.7	−40.4 ± 0.1	18	
3	G337.92–MF3	16:41:10.37	−47:08:02.7	1946.7	24.6	1.06 × 0.96	6.4	0.77 × 0.60	−23.9	1852.2	−38.2 ± 0.1	22	HC*
4	G337.92–MF4	16:41:10.51	−47:08:03.4	1623.9	15.6	0.98 × 0.81	71.9	0.64 × 0.35	−86.2	1282.5	−42.8 ± 0.6	54	
5	G337.92–MF5	16:41:10.38	−47:08:04.7	806.0	6.8	1.10 × 0.85	−216.0	0.88 × 0.29	−40.6	1385.1	−41.0 ± 0.1	6	
6	G337.92–MF6	16:41:10.46	−47:08:01.6	612.0	12.0	1.12 × 0.75	72.8	0.83 × 0.21	81.9	1136.7	−38.7 ± 0.1	10	
7	G337.92–MF7	16:41:10.46	−47:08:05.8	223.2	6.7	0.79 × 0.75	40.9	_	_	988.2	−40.6 ± 0.1	4	
						G338.93							
1	G338.93–MF1	16:40:34.01	−45:42:07.3	3977.6	57.3	1.05 × 0.97	92.3	0.79 × 0.59	87.3	2675.4	−63.7 ± 0.1	25	HC*
2	G338.93–MF2	16:40:34.13	−45:41:36.3	2229.0	67.3	0.89 × 0.84	66.4	0.56 × 0.34	74.1	1727.7	−61.2 ± 0.3	17	HC
3	G338.93–MF3	16:40:33.54	−45:41:37.3	1046.0	51.1	1.12 × 0.99	53.6	0.87 × 0.63	61.2	2913.3	−61.4 ± 0.1	15	HC*
4	G338.93–MF4	16:40:34.25	−45:41:37.1	493.7	31.4	0.83 × 0.73	229.6	_	_	1419.6	−60.0 ± 0.2	10	HC*
5	G338.93–MF5	16:40:33.71	−45:42:09.8	121.5	4.8	1.00 × 0.67	64.7	0.72 × 0.35	67.4	1977.3	−63.5 ± 0.1	4	
						G351.77							
1	G351.77–MF1	17:26:42.58	−36:09:16.7	14392.7	27.9	2.05 × 1.54	92.9	1.87 × 1.10	−88.0	2882.0	−7.4 ± 0.1	54	HC*
2	G351.77–MF2	17:26:42.43	−36:09:18.8	9804.6	34.6	2.27 × 1.72	112.5	2.09 × 1.36	−71.4	3388.0	−2.4 ± 0.1	55	HC
3	G351.77–MF3	17:26:42.41	−36:09:17.4	8855.3	23.7	1.95 × 1.52	128.6	1.71 × 1.14	−59.4	2800.0	−1.9 ± 0.1	45	HC
4	G351.77–MF4	17:26:42.67	−36:09:18.5	8059.5	24.6	1.79 × 1.19	61.7	1.56 × 0.58	66.7	1904.0	−6.0 ± 0.1	21	
5	G351.77–MF5	17:26:42.80	−36:09:20.5	302.1	2.4	0.76 × 0.53	61.8	0.91 × 0.40	77.9	1212.0	−4.8 ± 0.3	2	
						G353.41							
1	G353.41–MF1	17:30:28.44	−34:41:47.7	360.1	6.1	1.09 × 0.74	−228.0	0.72 × 0.56	−69.7	1288.0	−19.1 ± 3.6	3	

Notes. The peak position[(a)], peak intensity[(b)], signal-to-noise ratio[(c)], major and minor axes[(d)] as well as position angle[(d)] of the 2D Gaussian, are derived using GExt2D, except for the brightest source of G327.29, G328.25 and W51-E, where the peak position of the methyl formate emission is set as the position of the brightest compact continuum core. In the cases of G328.25, G328–shock1, and G328–shock2, the asterisk indicates the peak positions of the methyl formate emission initially extracted by GExt2D, which correspond to accretion shocks (see Fig. 4, as well as Csengeri et al. 2018). The major and minor axes[(e)] and position angle[(e)] deconvolved from the line cube beam size as explained in Appendix E. The mean deconvolved source size[(f)] of the methyl formate emission is computed at the distance of each protocluster. When the deconvolved source size falls below the minimum size set for each protocluster (see Sect. 5.3), then the deconvolved major and minor axes, as well as the position angle values are left blank, and the mean deconvolved source size of the methyl formate emission ($FWHM^{dec}_{MF}$) is set to half the synthesized beam size of the line cube. The rest velocity[(g)] of the source is derived from the fits to the three CH_3OCHO lines that are not contaminated by DCO^+ and the uncertainty represents the standard deviation. Percentage of the total number of channels[(h)] per spw that contain emission above the 3σ noise level (Sect.3.3). The last column[(i)] indicates the methyl formate sources tentatively classified as hot cores (HC) based on their mass >8 $M_\odot$. The sources with their lowest estimated mass <8 $M_\odot$ are marked with a star (HC*). The sources previously identified toward W43-MM1 in Paper IV are indicated in parentheses in the second column after the source name.

Table 4. continued.

ID	Name	RA[(a)] [h:m:s]	Dec[(a)] [°:′:″]	$S^{peak}_{MF(b)}$ [mJy beam^{-1} km s^{-1}]	$S/N^{(c)}$	$\theta_{maj} \times \theta^{(d)}_{min}$ [″ × ″]	PA[(d)] [deg]	$\theta^{dec}_{maj} \times \theta^{dec(e)}_{min}$ [″ × ″]	PA$^{dec(e)}$ [deg]	$FWHM^{dec(f)}_{MF}$ [au]	$V^{(g)}_{LSR}$ [km s^{-1}]	%channels[(h)] [%]	Tentative classification
						W43-MM1							
1	W43-MM1–MF1(4)	18:47:46.99	−01:54:26.4	8661.5	76.3	1.09 × 0.95	66.2	0.96 × 0.71	79.2	4576.0	101.8 ± 0.1	76	HC
2	W43-MM1–MF2(1)	18:47:47.03	−01:54:27.0	4822.0	33.5	0.91 × 0.78	58.6	0.75 × 0.48	77.7	3327.5	99.6 ± 0.1	53	HC
3	W43-MM1–MF3(2)	18:47:46.84	−01:54:29.3	3043.8	74.4	0.70 × 0.59	99.6	0.51 × 0.29	−80.8	2123.0	99.5 ± 0.2	70	HC
4	W43-MM1–MF4(3)	18:47:46.37	−01:54:33.5	1000.3	31.8	0.73 × 0.65	74.4	_	_	1545.5	97.2 ± 0.1	36	HC
5	W43-MM1–MF5(5)	18:47:46.76	−01:54:31.2	575.8	41.9	0.72 × 0.53	91.6	0.54 × 0.37	−85.0	2502.5	98.9 ± 1.0	22	HC*
6	W43-MM1–MF6(11)	18:47:46.51	−01:54:24.2	554.4	40.8	0.67 × 0.50	97.9	0.47 × 0.42	−81.6	2453.0	93.9 ± 0.2	34	
7	W43-MM1–MF7(10)	18:47:46.90	−01:54:30.0	212.6	12.8	0.84 × 0.56	136.5	0.65 × 0.24	−55.3	2205.5	100.6 ± 0.2	19	
8	W43-MM1–MF8(9)	18:47:46.47	−01:54:32.6	412.3	14.1	0.67 × 0.56	124.8	0.45 × 0.31	−71.2	2084.5	96.2 ± 0.3	20	HC*
9	W43-MM1–MF9	18:47:44.77	−01:54:45.2	128.5	12.1	0.64 × 0.44	102.1	0.49 × 0.42	−79.4	2519.0	95.2 ± 0.1	13	
10	W43-MM1–MF10	18:47:46.53	−01:54:23.1	90.9	7.0	0.62 × 0.41	89.4	0.50 × 0.39	−86.0	2475.0	97.1 ± 0.2	17	HC*
11	W43-MM1–MF11	18:47:47.00	−01:54:30.7	89.3	8.1	0.64 × 0.45	92.2	0.42 × 0.47	−84.4	2475.0	100.1 ± 0.3	15	HC*
12	W43-MM1–MF12	18:47:46.88	−01:54:25.8	88.2	3.6	0.52 × 0.42	216.8	_	_	1545.5	99.4 ± 0.1	11	
13	W43-MM1–MF13	18:47:46.25	−01:54:33.4	50.0	4.7	0.90 × 0.60	108.0	0.76 × 0.26	−74.8	2458.5	97.2 ± 0.1	11	
14	W43-MM1–MF14	18:47:46.96	−01:54:29.7	49.0	2.6	0.56 × 0.37	89.8	0.54 × 0.29	−85.3	2194.5	100.9 ± 0.3	16	
						W43-MM2							
1	W43-MM2–MF1	18:47:36.79	−02:00:54.2	4459.6	80.9	1.04 × 0.94	−33.2	0.88 × 0.73	−49.4	4444.0	88.6 ± 0.1	62	HC
2	W43-MM2–MF2	18:47:36.70	−02:00:47.6	71.3	16.4	0.82 × 0.55	93.9	0.64 × 0.30	−84.5	2420.0	89.9 ± 0.7	3	
3	W43-MM2–MF3	18:47:36.27	−02:00:50.7	46.3	6.3	0.63 × 0.42	110.9	0.46 × 0.36	−72.9	2255.0	91.0 ± 0.3	1	
						W43-MM3							
1	W43-MM3–MF1	18:47:39.26	−02:00:28.1	175.8	16.1	0.86 × 0.78	29.1	0.61 × 0.48	51.6	2981.0	94.8 ± 1.7	13	
2	W43-MM3–MF2	18:47:41.71	−02:00:28.6	76.7	16.8	0.78 × 0.64	103.1	_	_	1688.5	92.8 ± 0.3	10	HC*
3	W43-MM3–MF3	18:47:41.73	−02:00:27.5	23.0	4.9	0.87 × 0.58	98.4	0.65 × 0.30	−84.0	2464.0	93.2 ± 0.3	2	
						W51-E							
1	W51-E–MF1	19:23:43.97	14:30:34.5	4215.0	_	2.74 × 2.32	23.9	2.71 × 2.27	24.1	13435.2	56.3 ± 0.3	73	HC
2	W51-E–MF2	19:23:43.87	14:30:27.3	2119.5	40.9	1.14 × 0.95	114.6	1.04 × 0.89	−66.9	5211.0	54.9 ± 0.8	65	HC*
3	W51-E–MF3	19:23:43.88	14:30:27.9	1794.7	26.5	0.88 × 0.78	314.7	0.76 × 0.69	−33.1	3936.6	60.0 ± 0.5	72	HC
4	W51-E–MF4	19:23:43.74	14:30:21.4	81.5	10.7	0.67 × 0.45	24.5	0.57 × 0.08	25.9	1188.0	62.7 ± 0.1	7	
5	W51-E–MF5	19:23:43.84	14:30:24.5	73.6	8.6	0.83 × 0.74	−36.8	0.71 × 0.63	−18.3	3634.2	58.1 ± 0.5	9	HC*
6	W51-E–MF6	19:23:43.80	14:30:19.6	40.9	10.2	0.82 × 0.66	102.0	0.69 × 0.55	−86.4	3337.2	58.4 ± 0.1	3	
7	W51-E–MF7	19:23:43.82	14:30:23.3	31.9	3.1	0.75 × 0.56	81.1	0.63 × 0.39	70.6	2683.8	61.6 ± 0.8	4	HC*
						W51-IRS2							
1	W51-IRS2–MF1	19:23:40.00	14:31:05.5	10097.2	57.0	1.37 × 1.13	138.3	1.24 × 0.94	−39.0	5837.4	58.3 ± 0.3	73	HC
2	W51-IRS2–MF2	19:23:39.82	14:31:05.0	5162.1	47.8	0.96 × 0.89	57.2	0.72 × 0.68	38.5	3796.2	61.1 ± 0.1	73	HC
3	W51-IRS2–MF3	19:23:40.04	14:31:04.9	3049.0	15.8	1.25 × 1.01	69.9	1.08 × 0.84	69.7	5151.5	56.8 ± 0.5	72	HC
4	W51-IRS2–MF4	19:23:39.95	14:31:05.2	2933.2	15.4	1.1 × 0.83	2.8	0.94 × 0.54	0.5	3882.6	58.8 ± 0.1	48	HC
5	W51-IRS2–MF5	19:23:39.74	14:31:05.3	2716.2	29.5	0.89 × 0.83	−17.4	0.68 × 0.54	−18.0	3288.6	63.0 ± 0.4	40	HC
6	W51-IRS2–MF6	19:23:38.57	14:30:41.8	1720.5	91.2	0.71 × 0.64	−23.6	_	_	1630.8	62.6 ± 0.1	23	HC
7	W51-IRS2–MF7	19:23:39.50	14:31:03.3	105.3	8.5	0.65 × 0.59	−130.1	_	_	1630.8	63.7 ± 0.9	7	
8	W51-IRS2–MF8	19:23:41.81	14:30:54.9	84.7	5.4	0.71 × 0.47	−13.6	0.43 × 0.43	−14.8	2305.7	55.2 ± 0.6	9	
9	W51-IRS2–MF9	19:23:38.42	14:30:36.6	52.4	5.0	1.04 × 0.85	15.1	0.86 × 0.59	9.3	3850.2	60.8 ± 0.2	5	

which the two CH_3OCHO line pairs are detected above the 3σ noise level given in Table 2 are considered as robust detections and are used in the rest of our analysis. Their spectra are shown in Fig. A.1.

In the case of G327.29 and G351.77, a closer look at the spectra extracted toward the individual methyl formate sources, in particular G327.29–MF1, G351.77–MF1, MF2, and MF3, shows that the velocity range used for the moment 0 maps is marginally contaminated by emission from other spectral lines. Using a narrower velocity range for the moment 0 maps for these sources gives, however, consistent parameters for the peak position and deconvolved source size. The indicated velocity range is, however, necessary to extract all methyl formate emission observed toward the fainter sources G351.77–MF5, G327.29–MF1, and MF2. For this reason, for the rest of our analysis we use the same velocity range of 35 km s^{-1} for G327.29 and G351.77 as for the other regions.

3.3. Fraction of channels containing emission

We used the spectra shown in Fig. A.1 to assess the spectral line richness of each methyl formate source. To do so, we counted the number of channels that contain emission above the 3σ noise level, using the rms values listed in Table 2. The percentage of channels containing emission above 3σ in the spectrum observed toward each methyl formate source is shown in Table 4. These values range between 1 and 77%, where the sources with the highest percentage of channels containing emission above the threshold are expected to be the richest in emission lines. This percentage is well correlated with the peak intensity measured in the methyl formate moment 0 maps. However, because of the sensitivity limitation of the dataset, we may miss fainter emission lines from more compact sources (see also the discussion in Sect. 6.3). For this reason, the fraction of channels containing emission in B6-spw0 is not used as an additional quantitative criterion to classify potential hot cores in the rest of the paper.

3.4. V_{LSR} estimates

Using the position of the methyl formate sources identified with the GExt2D algorithm, we extracted single-pixel spectra to fit the CH_3OCHO lines. We derived the V_{LSR} of each methyl formate source by fitting a single component, 1D Gaussian to each of the three methyl formate lines that are not contaminated by

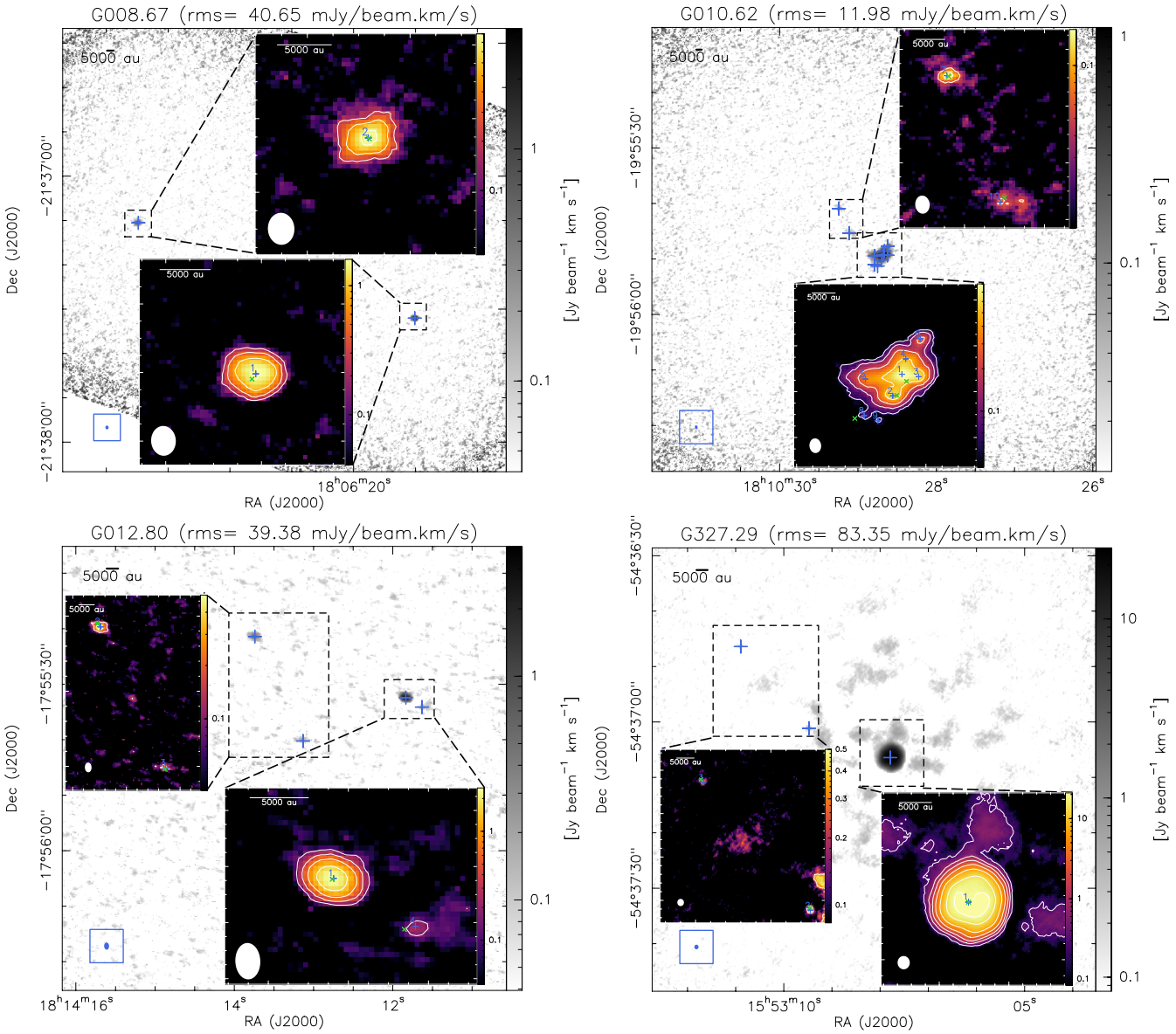

Fig. 3. Moment 0 maps of methyl formate obtained toward the ALMA-IMF protoclusters as described in Sect. 3.1. Contours start at 5σ (the 1σ rms noise level is indicated on top of each panel) and double in value thereafter. In each panel the blue crosses show the peak positions of the methyl formate sources extracted with GExt2D, while the green crosses show their associated continuum cores from the getsf-unsmoothed catalog (Paper XII). The blue or white ellipses in each panel represent the synthesized beam of the line cubes.

DCO$^+$ emission (see Table 3). The average $V_{\rm LSR}$ for each methyl formate source are provided in Table 4. We find that in most cases, the average centroid $V_{\rm LSR}$ of the methyl formate sources are consistent with the protocluster $V_{\rm LSR}$ given in Table 1, with velocity offsets $V_{\rm off} < 5$ km s^{-1}, where $V_{\rm off} = |V_{\rm LSR}$ (MF) $- V_{\rm LSR}$ (protocluster)|. In the cases of G333.60, W43-MM2, W51-E, and W51-IRS2, however, the velocity offset of some methyl formate sources is >5 km s^{-1}, and may be up to ~9 km s^{-1}.

In Paper VII we used the fits from a single DCN ($J = 3 - 2$) line observed toward the whole sample of continuum cores spectra. We found no obvious correlation between the spread of the core $V_{\rm LSR}$ and the evolutionary stage of the protocluster.

4. The catalog of hot core candidates

Hereafter, we define a hot core candidate as a peak of methyl formate emission extracted from the moment 0 maps with the GExt2D algorithm. In the following subsections we present the catalog of hot core candidates, including new detections, and we discuss in more details the identification of hot core candidates in regions with compact and extended CH_3OCHO emission.

4.1. Statistics of hot core candidates

All the 15 ALMA-IMF protoclusters, including the youngest ones, exhibit some emission in the investigated CH_3OCHO transitions and harbor at least one potential hot core candidate (see Figs. 3–6). Overall, we find a total of 76 methyl formate sources, which is about an order of magnitude fewer cores compared to the number of purely dust continuum cores, from the getsf-unsmoothed catalog (Paper XII; see also Sect. 2.2). The full list of methyl formate sources is given in Table 4, with their coordinates and peak values measured in the CH_3OCHO moment 0 maps with GExt2D. Important characteristics of the hot core

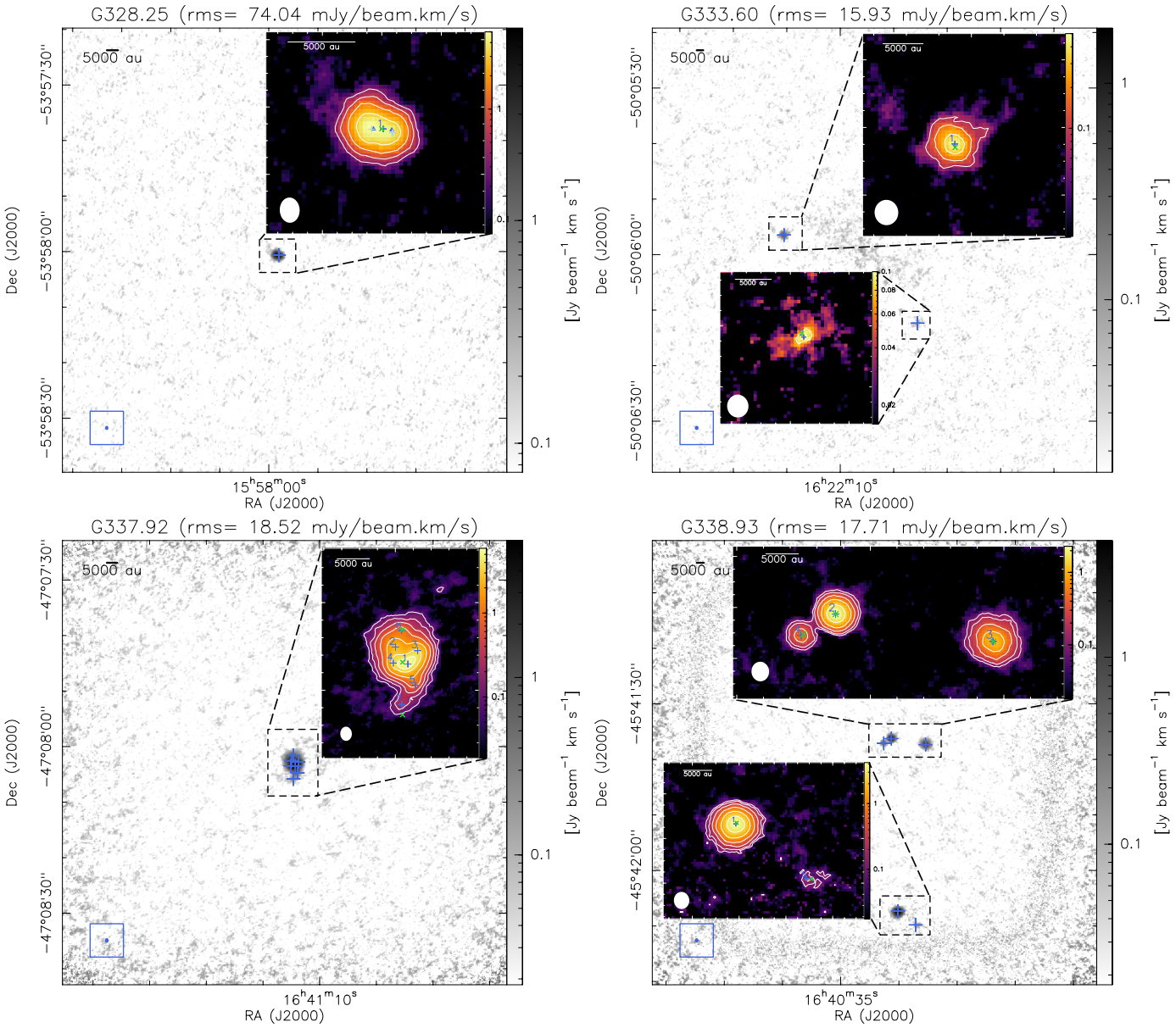

Fig. 4. Same as Fig. 3. In the case of G328.25, the two light blue crosses show the peak position of methyl formate initially extracted by GExt2D, which correspond to the position of the accretion shocks identified by Csengeri et al. (2018), of which the positions are marked with blue triangles.

candidates (FWHM sizes and total gas masses) are derived and discussed in Sect. 5.

In Fig. 7 we show the number of compact methyl formate sources per region, as a function of the number of dust continuum cores from the getsf-unsmoothed catalog presented in Paper XII, excluding free-free sources. We distinguish two groups of sources, one with the three evolved protoclusters, G012.80, G333.92, and W51-IRS2, as well as the intermediate region, G353.41, and the other one with the remaining 11 protoclusters. In both groups there is an increasing trend of the number of hot core candidates as a function of the number of continuum cores. The region with the largest number of hot core candidates is the young protocluster W43-MM1, with as many as 14 compact methyl formate sources in a single field. The young protocluster G328.25 and the intermediate one G353.41 both harbor only a single hot core candidate. Their particular cases are further discussed in Sects. 4.2 and 6.6.

In Fig. 8 we show for each ALMA-IMF protocluster, the ratio of the number of hot core candidates to the number of dust continuum cores, as a function of the mass of the protocluster, $M_{\rm cloud}$. It shows that in all cases, the number of hot core candidates per region never represents more than 25% the number of dust continuum cores. Furthermore, no clear trend emerges, neither as a function of clump mass nor of the evolutionary stage of the protocluster. Young, intermediate, and evolved protoclusters do not exhibit any clear difference, suggesting that the methyl formate source properties are independent of the evolutionary stage of their hosting clumps.

4.2. Hot core candidates detected in regions with compact CH_3OCHO emission

For nine out of the 15 ALMA-IMF protoclusters, the source identification is relatively straightforward since they mainly harbor

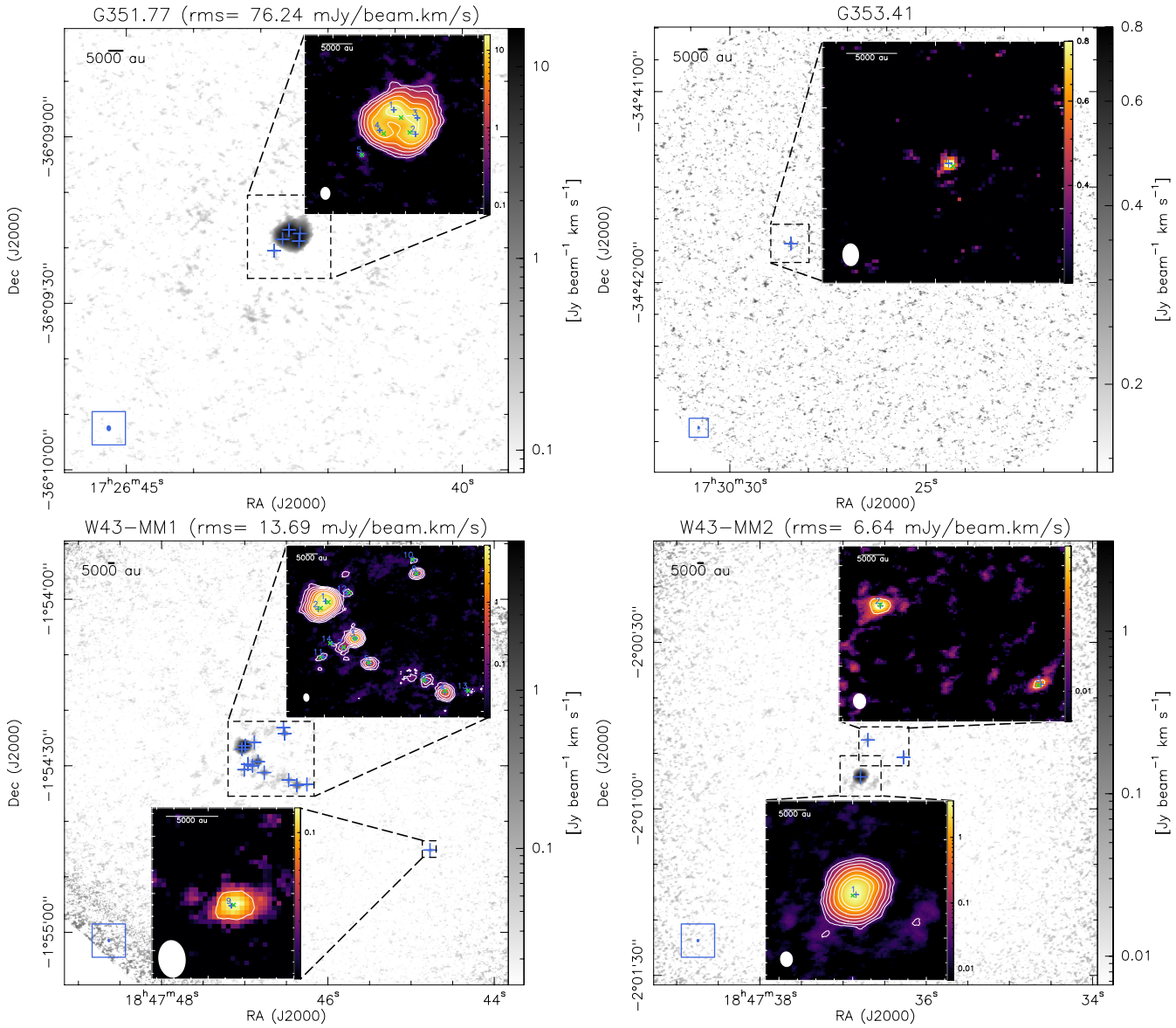

Fig. 5. Same as Fig. 3.

individual objects. These objects have rather compact, elliptical or circular emission, with an extent of a few thousand au.

In particular, G008.67 harbors two individual, elliptical, compact sources. Toward G012.80 we identified four individual, rather elliptical sources, two of which are well resolved, and two are compact sources. We identified two faint methyl formate sources toward G333.60 that is one of the most evolved regions in our sample. G338.93 is a young region that harbors 5 isolated, circular, compact sources. G353.41 is a more evolved region that is very bright in the continuum at 1.3 mm, and strongly affected by ionized gas coming from UC-HII regions (see Fig. 2 of Paper I). This region is a remarkable outlier of the ALMA-IMF sample as it hosts only one weak CH_3OCHO source, despite the fact that it hosts a large number of continuum cores, with 57 sources identified in the getsf-unsmoothed core catalog (see also Sect. 6.6). The largest number of methyl formate sources, 14, is found toward the young protocluster W43-MM1, where most of the sources are resolved and appear as isolated sources. We identified three individual compact methyl formate sources toward both W43-MM2 and W43-MM3, the larger ones of which are rather circular.

The case of G328.25 is somewhat particular because, according to Csengeri et al. (2019), it shows extended CH_3OCHO emission associated with accretion shocks (see the blue triangles in Fig. 4) that are resolved at an angular resolution of 0.23″ (~575 au at the distance of G328.25). These two distinct peaks have also been identified and extracted with the GExt2D algorithm from the ALMA-IMF CH_3OCHO moment 0 map (see the light blue crosses in Fig. 4), where the emission is marginally extended in CH_3OCHO at an angular resolution of 0.67″ (~1675 au). Based on an unbiased spectral line survey obtained with the Atacama Pathfinder Experiment (APEX) telescope toward G328.25, Bouscasse et al. (2022) analyzed the molecular composition of this region and extracted the excitation conditions for several species. Based on the properties of COMs, they suggest that this source corresponds to an emerging hot core. We thus report the peak positions of the CH_3OCHO emission in Table 4 (as G328.25–shock1 and shock2), but we

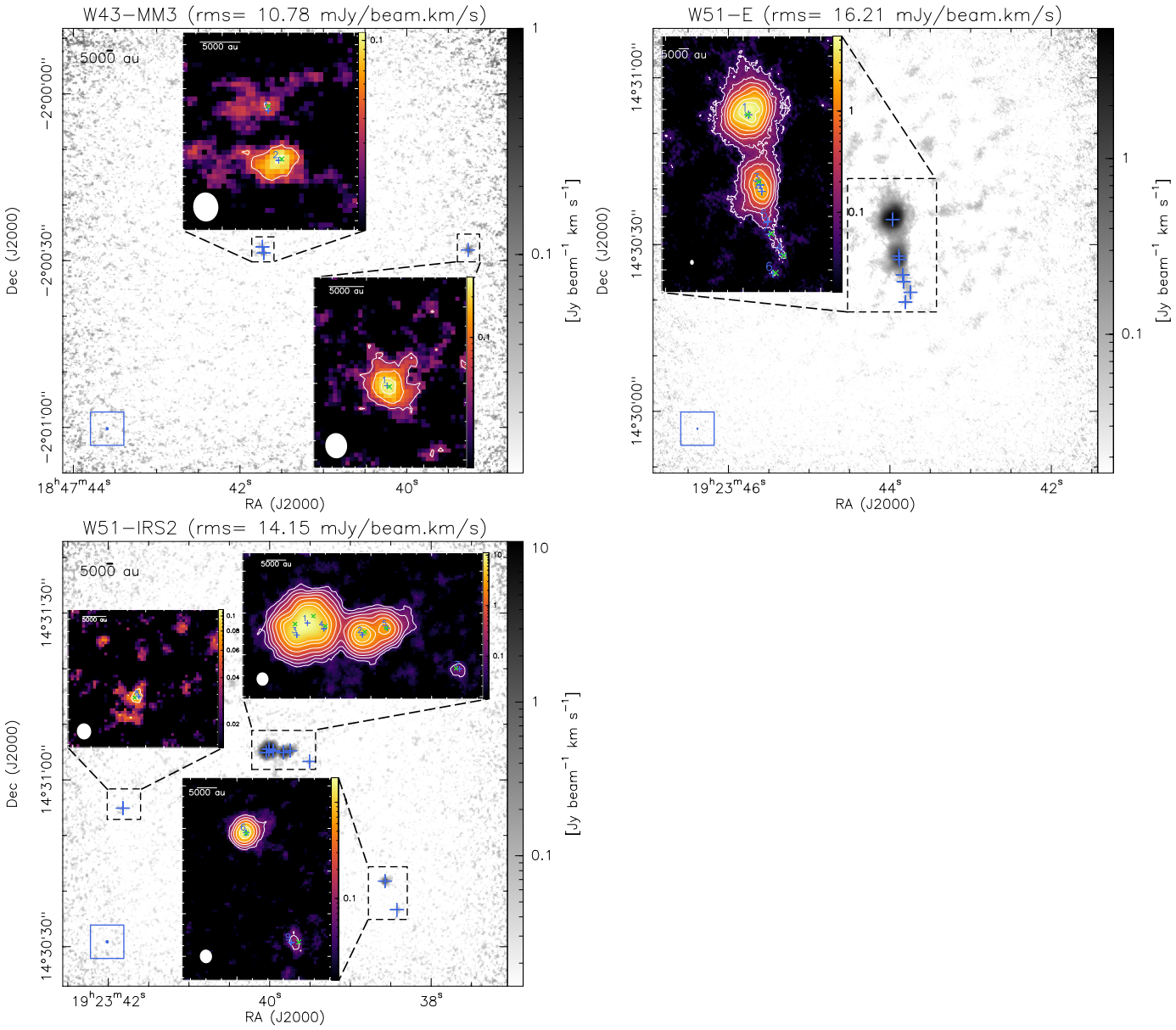

Fig. 6. Same as Fig. 3.

consider this source to be a single core, at the peak position of the continuum core.

4.3. Hot core candidates detected in regions with extended CH_3OCHO emission

The other six ALMA-IMF protoclusters exhibit both compact sources and extended emission of methyl formate. G327.29 and W51-E, are dominated by a central bright source, while the four other protoclusters exhibit extended, non axisymmetric emission.

The central source of G327.29 is dominated by extremely bright emission in methyl formate, in fact both the methyl formate and the continuum emission features are similar, circularly symmetric, except toward its central position (see Fig. 3), where an arc-like emission feature suggests that the lower part of the circle is brighter. Such features could be explained by intrinsic inhomogeneity in the CH_3OCHO emitting gas, but also by dust opacity. With a 2D Gaussian fit to the CH_3OCHO emission, we measure an extent of 2.7″ (deconvolved FWHM), which corresponds to a size of ∼6800 au at the distance of G327.29, and is >3 times larger that the synthesized beam of the line datacube. This size is considerably larger than most of the other methyl formate sources that are typically compact sources. For simplicity, we considered the bright source seen in methyl formate toward G327.29 to be a single, individual core (G327.29–MF1) associated with the peak position of the continuum emission, which is consistent with the results of Gibb et al. (2000), Bisschop et al. (2013), and Wyrowski et al. (2008). Two additional, individual, fainter methyl formate sources are detected toward G327.29, well offset from the central source.

We find another source similar to G327.29–MF1 that is in the W51-E protocluster, W51-E–MF1, also known in the literature as W51-e2. This central source is dominated by very bright circular emission, extended up to 2.5″, which corresponds to ∼13 400 au at the distance of the protocluster, and is >6 times larger that the synthesized beam of the line datacube. In this

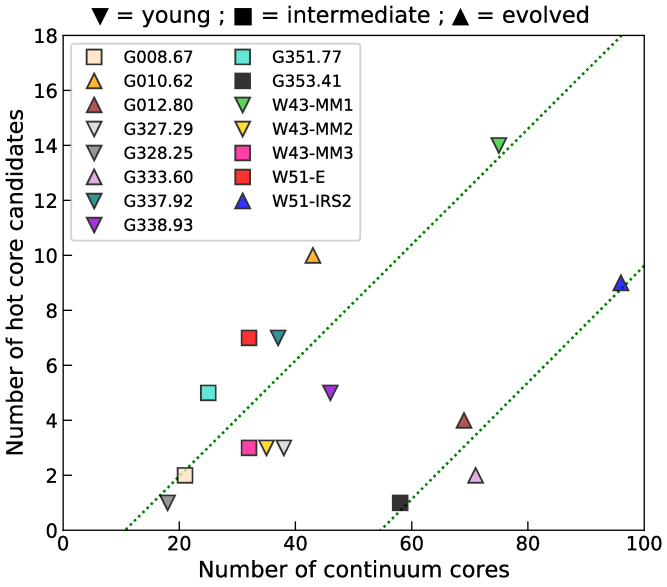

Fig. 7. Number of hot core candidates per ALMA-IMF protocluster as a function of the number of dust continuum cores from the unsmoothed core catalog presented in Paper XII, excluding free-free sources. The different symbols represent the different evolutionary stages of the protoclusters: young, intermediate and evolved, as indicated on top of the figure. The dashed lines show linear fits to the two distinct groups of protoclusters.

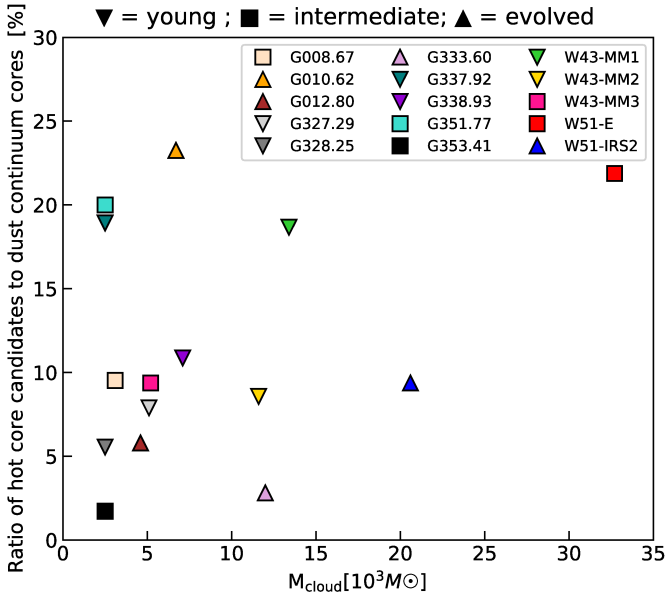

Fig. 8. Ratio of the number of hot core candidates to the number of dust continuum cores from the unsmoothed core catalog presented in Paper XII, excluding free-free sources, as a function of the mass of the protocluster ($M_{\rm cloud}$). The different symbols represent the different evolutionary stages of the ALMA-IMF protoclusters: young, intermediate and evolved, as indicated on top of the figure.

case, assuming a single source associated with the peak of the continuum emission is consistent with the results presented by Ginsburg et al. (2017) and Goddi et al. (2020) who argue that this source is powered by a single central massive star. In addition to the central source, two methyl formate sources have been identified in the bright emission south of the main one, which is elongated in the north-south direction. We could also identify in the same direction, four additional fainter, clustered sources.

Toward the W51-IRS2 protocluster, nine methyl formate sources have been identified that are rather circular. Five of them are particularly bright and clustered in the center of the field. These sources could easily be identified by our source-extraction algorithm, and they indeed correspond to the same peaks seen in methyl formate moment 0 maps obtained at higher angular resolution of 0.2″ by Ginsburg et al. (2017) (see their Fig. 4).

We find that three regions, G010.62, G351.77, and G337.92, exhibit extended CH_3OCHO emission with a complex clustered structure. In this case, the CH_3OCHO peaks are surrounded by non axisymmetric extended emission, and we report here only the peak positions extracted by GExt2D. In the cases of G351.77 and G337.92, we identified four and seven individual sources, respectively. In the case of G010.62, a well-known UC-HII region, we detected two isolated methyl formate sources, and eight more sources in a clustered blob in the center of the field. The nature of these sources, associated with the UC-HII region, is further discussed in Sect. 6.3.

4.4. Newly discovered hot core candidates

In this section we discuss the compact methyl formate sources identified with our analysis that were not qualified before as hot cores in the literature, and are thus newly discovered hot core candidates based on the ALMA-IMF Large Program. Overall, we find 56 sources that could be considered as new hot core candidates, which represents more than two thirds (76%) of the ALMA-IMF methyl formate source sample.

G008.67. harbors two compact methyl formate sources. One of them, G008.67–MF2, coincides with the compact hot core identified from CH_3CN observations conducted with the Submillimeter Array (SMA) at about 3″ resolution, which corresponds to >10 000 au at the distance of G008.67 (Hernández-Hernández et al. 2014). G008.67–MF1 is a new detection.

G012.80. harbors four compact methyl formate sources. Our hot core candidate G012.80–MF2, corresponds to the W33-Main North region, while G012.80–MF1 and G012.80–MF4 coincide with W33-Main West source in the SMA continuum map at 345 GHz from Immer et al. (2014) (see their Fig. 7 at 2.3″ resolution, which corresponds to 5500 au at the distance of G012.80). While they discuss the nature of these regions, these sources have not been qualified as hot cores. We thus consider four new hot core candidates toward G012.80.

G333.60. is known as a bright and extended HII region (Lo et al. 2015), for which we are not aware of dedicated observations to search for hot core emission at high angular resolution. We identified two faint methyl formate sources in the CH_3OCHO moment 0 maps obtained toward G333.60, which are new detections.

G338.93. harbors five compact methyl formate sources that had never before been reported as hot cores, to the best of our knowledge. We thus consider them as five new detections.

G351.77. has been previously recognized as a bright hot core by several authors, such as Leurini et al. (2008), Liu et al. (2020), and Taniguchi et al. (2023). Thanks to our improved angular resolution, we could split the bright emission in the central part of G351.77 and thus report four new detections in this region. Beuther et al. (2017) resolves the small-scale structure of

the G351.77 hot core down to 0.06″ angular resolution and find indication for multiplicity at such small scales.

G353.41. was recently covered by the ATOMS survey (Liu et al. 2020, at 1.6″, which corresponds to 3200 au at the distance of the protocluster). However, no hot core detection has been reported toward G353.41. Our hot core candidate is therefore a new detection in this region.

W43-MM1, W43-MM2, and W43-MM3. constitute a mini starburst region. We find 14 compact methyl formate sources toward W43-MM1, eight of which correspond to the positions identified by Paper IV (see also the second column of Table 4). One of our sources is outside their investigated field of view, and five are new detections. In this case, our approach using only the CH_3OCHO emission is more sensitive compared to their method, relying on line density estimates within a broader bandwidth (∼2 GHz) toward the peak positions of the continuum cores. Together with the six sources detected toward W43-MM2 and W43-MM3, we detect 11 new hot core candidates in the W43 protocluster.

G327.29. harbors a well known central hot core. In addition, we identified two other fainter sources, G327.29–MF2 and G327.29–MF3, well offset from the central source. Their positions coincide with the continuum peaks SMM2 and SMM4 identified by Leurini et al. (2017) in the SABOCA continuum emission map at 350 μm (see their Fig. 3). Since these sources were not qualified as hot cores by Leurini et al. (2017), we consider them as new detections.

W51-E and W51-IRS2. have been previously studied and recognized as hosting several bright hot cores (see, e.g., Ginsburg et al. 2017, and references therein). Only the fainter methyl formate sources extracted from the moment 0 maps are considered as new detections. It represents four sources toward W51-E (MF4 – MF7), and another four toward W51-IRS2 (MF6–MF9).

G337.92. has not been the subject detailed high angular-resolution studies on its chemical content before the ALMA-IMF program, and thus the seven individual methyl formate sources are considered as new detections.

G010.62. is another prominent hot core in the Galactic plane. Our hot core candidates G010.62–MF3 and G010.62–MF5 correspond to the well resolved individual objects MF1 and MF2 from (Law et al. 2021) based on ALMA observations at higher angular resolution compared to that of ALMA-IMF. G010.62–MF3 and G010.62–MF2 correspond to source 1 and 2 from Taniguchi et al. (2023). Furthermore, some of our remaining hot core candidates correspond to well identified peaks in CH_3OH in Law et al. (2021), although, they have not been identified and discussed as hot cores. Overall, we propose seven sources that we consider to be new detections in this region.

5. Properties of the methyl formate sources

In the following subsections, we investigate the physical properties of the 76 sources identified and extracted from the CH_3OCHO moment 0 maps using the GExt2D algorithm.

5.1. Continuum emission associated with methyl formate compact sources

In order to characterize the physical properties of hot core candidates, we use the thermal dust continuum emission

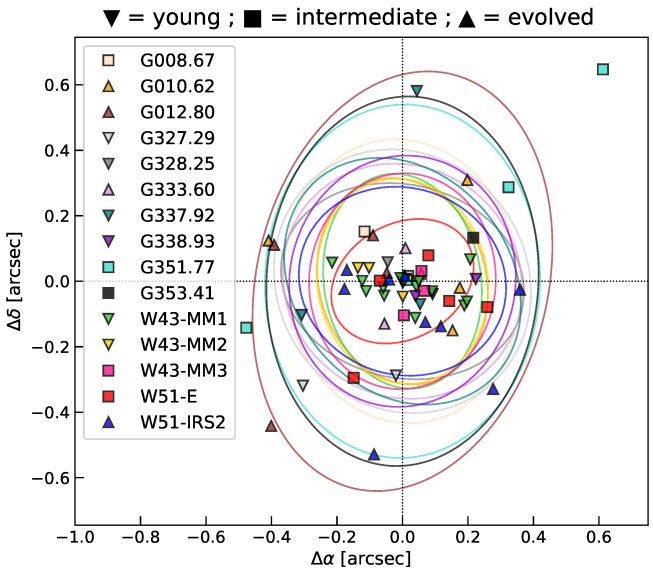

Fig. 9. 2D distribution of the angular offsets between the peak position of each CH_3OCHO source extracted with GExt2D and its associated continuum core extracted with getsf. The different symbols represent the different evolutionary stages of the protoclusters – young, intermediate, or evolved – as shown on top of the plot. The dashed vertical and horizontal lines indicate the $x = 0$ and $y = 0$ axes, respectively. The ellipses represent the synthesized beam sizes (FWHM) of the 15 ALMA-IMF B6-spw0 line cubes. The diameter of the corresponding ellipse (i.e., θ_{ave}) is used as a criterion to associate CH_3OCHO sources with continuum cores toward each protocluster. The methyl formate sources that are not associated with any compact continuum core are not shown in this figure.

associated with these sources. To this regard, we cross-matched our catalog of methyl formate sources with that of the continuum cores from Paper XII (see Sect. 2.2). We associate a methyl formate source with a continuum core if the angular offset between their respective peak positions is smaller than the diameter (FWHM) of the synthesized beam of the CH_3OCHO line datacube. Figure 9 shows the angular offsets computed between each methyl formate source and its closest continuum core from the getsf-unsmoothed catalog. We find that a large majority of the methyl formate sources have a good positional correspondence to that of the continuum cores, with in total 84% of the methyl formate sources having a counterpart in the unsmoothed continuum core catalog. These continuum cores are indicated with green crosses in the moment 0 maps of methyl formate shown in Figs. 3–6. On the other hand, 12 methyl formate sources (i.e., ∼16% of the total sample) do not coincide with any compact continuum core from the getsf-unsmoothed catalog. These sources are found toward four protoclusters, G010.62, G337.92, G351.77, and W51-E, which are two intermediate regions, a young, and an evolved one. In Figs. B.1–B.4 we compare the 1.3 mm continuum emission with the contours of the methyl formate integrated intensity. For the four protoclusters listed above, we find that the methyl formate compact sources that are not associated with any compact continuum core are exclusively found in regions of extended methyl formate emission, and also coincide with extended continuum emission at 1.3 mm. These cases are addressed in more details below.

In the intermediate stage protocluster W51-E, two methyl formate sources, W51-E–MF2 and W51-E–MF5, located in the extended north-south emission, could not be associated with any compact continuum core based on our position-match criterion. They fall, however, on the extended continuum emission that

exhibits some fluctuations in the vicinity of the methyl formate sources (see Fig. B.4). It is likely that both the complexity of the emission and a lower background to core emission contrast hinders the identification of their continuum counterpart.

In the other intermediate evolutionary stage region, G351.77, the overall continuum emission at 1.3 mm is extended in the west-east direction (see Fig. B.3), and does not resemble the shape of the CH_3OCHO emission. While G351.77–MF2 and G351.77–MF4 have a compact continuum core nearby, the brightest continuum core is somewhat in between G351.77–MF1 and G351.77–MF3. Our position-matching criterion associates the continuum core with G351.77–MF1, while G351.77–MF3 cannot be associated with any continuum core. Chemical segregation, blending of unresolved sources, or again the low contrast between the peak and the background could lead to such positional shifts between the continuum and the CH_3OCHO emission.

Toward the central part of the young protocluster G337.92 (see also Sect. 4.1) the CH_3OCHO emission exhibits an extended blob. Only sources G337.92–MF1, MF6, and MF7 seem to be associated with continuum peaks at 1.3 mm (see Fig. B.2). The other four sources G337.92–MF2, MF3, MF4, and MF5 do not closely coincide with any continuum peak and cannot be associated with any compact continuum core using our position-matching criterion. It is possible that these CH_3OCHO peaks correspond to inhomogeneities in extended emission heated by a single central source, or source blending prevents a firm association with continuum cores.

A similar case is observed toward the evolved region G010.62, where the CH_3OCHO spatial distribution is not symmetric, and exhibit a complex morphology that does not show a close correlation with the distribution of the 1.3 mm continuum emission (see Fig. B.1). This extended CH_3OCHO emission is unlikely to be attributed to a single source due to its spatial extent (see Sect. 4.3), and sources G010.62–MF3, MF4, MF5, MF6, and MF9 do not find any continuum counterpart in the getsf-unsmoothed continuum core catalog.

For the four ALMA-IMF regions mentioned above, where the methyl formate sources lie in the extended 1.3 mm continuum emission but cannot be associated with compact continuum cores, it is possible that the source extraction algorithm fails to disentangle and decompose the compact continuum cores on the top of a bright and extended background. The getsf definition of sources is the following (see also Sects. 1 and 3.2.2 of Men'shchikov 2021): sources are the relatively round emission peaks that are significantly stronger than the local surrounding fluctuations (of background and noise), indicating the presence of the physical objects in space that produced the observed emission. If a structure is too elongated or has a very complex shape, it is unlikely to be identified as a compact source. The nature of the 12 methyl formate sources listed above that could not be associated with a compact continuum core at 1.3, mm is further discussed in Sect. 6.3.

Table C.1 lists the peak positions, peak ($S^{\rm peak}$) and integrated fluxes ($S^{\rm int}$) measured in both the continuum maps at 1.3 and 3 mm, as well as the source sizes (FWHM) of all the continuum cores associated with methyl formate sources. For the 12 methyl formate sources that are not associated with compact continuum cores, their flux is measured within the beam size in the 1.3 mm continuum emission maps at the peak position of the CH_3OCHO emission. The flux is then corrected by subtracting the background emission estimated at this position during the source extraction process (see Sect. 2.2). Since no emission size is fitted for these sources, we use the average beam size of the continuum maps, $\theta_{\rm ave}^{\rm cont}$, as the continuum source size (i.e., $FWHM_{\rm cont} = \theta_{\rm ave}^{\rm cont}$); in this case, $S^{\rm peak} = S^{\rm int}$. The resulting values are listed in Table C.1. The methyl formate sources that are not associated with compact continuum cores are marked with a $*$ in the first column.

5.2. Free-free contamination

Reaching a certain stage in their evolution, high-mass (proto)stars develop ionizing radiation that leads to the emergence of HC-HII and UC-HII regions. Such sources exhibit free-free emission that may contribute to the observed continuum emission at 3 mm, and potentially even at 1.3 mm. The relative contribution of emission from ionized gas versus that of thermal dust continuum emission, however, depends on several factors, such as the source size of the ionizing emission and its optical depth. Since the ALMA-IMF fields cover massive protoclusters in a range of evolutionary stages, the contamination from free-free emission cannot be ignored for the total gas mass estimates for several sources.

The ALMA-IMF dataset covers the $H_{41\alpha}$ recombination line at 92.0 GHz, which originates from ionized gas coming from HII regions (see, e.g., Fig. 2 of Paper I), and we refer for a detailed analysis to Galván-Madrid et al. (2024). Using this information we identify 17 methyl formate sources that lie in intermediate and evolved regions containing free-free emission, these are G008.67, G010.62, G012.80, G333.60, W51-E, and W51-IRS2 (see Figs. D.1, D.2, and D.4). For these regions, in order to determine the contribution of free-free emission to the 1.3 mm flux densities, we rely on the dual band approach of ALMA-IMF and exploit the dust continuum emission at 1.3 mm, and 3 mm, like done in Paper III and Paper XII. First the 3 mm integrated fluxes are rescaled to the 1.3 mm sizes to allow a direct comparison of these fluxes as described in Paper III. Then we compute the theoretical flux ratio expected for thermal dust emission ($\gamma_{\rm th}^{\rm dust}$) as explained in Appendix D. Figure 10 shows the flux ratio ($S^{\rm int}_{\rm 1.3mm}/S^{\rm int}_{\rm 3mm}$) measured toward the 17 sources potentially affected by free-free emission, compared to the theoretical ratio computed assuming dust temperatures ranging from 50 K to 150 K (see Sect. 5.4) and a dust emissivity exponent α ranging from 3.2 to 3.8 (green shaded area). For each source with a flux ratio $<\gamma_{\rm th}^{\rm dust}$, a correction factor ($\rm frac_{ff}$) must be applied to both its peak and integrated flux measured at 1.3 mm to take into account the free-free contribution, as described in Appendix D. These correction factors are listed in the last column of Table C.1. The correction factor indicates the fraction of the flux initially measured that is due to free-free emission for each continuum core. We note that the 1.3 mm continuum emission measured toward G010.62–MF1 and G010.62–MF2 shows in both cases a level of free-free contamination, $\rm frac_{ff}$, of 100%. It suggests that their millimeter continuum emission is entirely due to ionized gas, which calls into question the nature of these two sources; we further discuss this in Sect. 6.3.

5.3. Source size

We estimate the size of the methyl formate sources from the FWHMs of the 2D Gaussian fitting to the CH_3OCHO moment 0 maps using GExt2D, as described in Sect. 3.2. The resulting minor ($\theta_{\rm min}$) and major axes ($\theta_{\rm maj}$) are deconvolved from the synthesized beam size of the line cube, considering the ellipticity of the sources and of the synthesized beam, as described in Appendix E. We set a minimum deconvolved size for each region to half the synthesized beam of the line cube, in order to limit

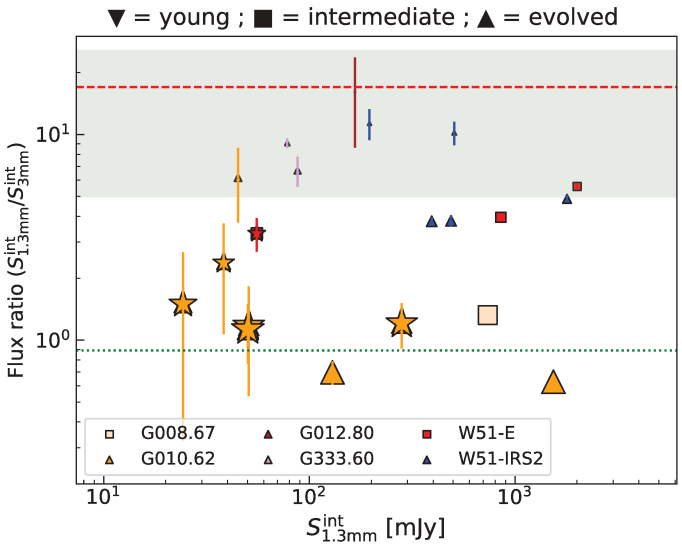

Fig. 10. Flux ratio ($S^{\rm int}_{1.3{\rm mm}}/S^{\rm int}_{3{\rm mm}}$) measured toward the methyl formate sources whose positions coincide with the $H_{41\alpha}$ emission in six ALMA-IMF protoclusters (see Figs. D.1–D.4). The different symbols represent the different evolutionary stages of the protoclusters: young, intermediate, or evolved, as shown on top of the figure. The methyl formate sources that are not associated with compact continuum cores are shown with stars. The size of each marker is proportional to the level of free-free contamination (e.g., the biggest markers correspond to G010.62–MF1 and G010.62–MF2 for which 100% of the flux measured at 1.3 mm is expected to be due to free-free emission). The green shaded area shows the theoretical ratio expected for dust cores, computed for a dust emissivity exponent α ranging from 2 to 4, for optically thin and thick dust emission, respectively. The dashed red line shows the theoretical ratio obtained using $\alpha = 3.5$ (as in Paper III), while the green dotted line shows the theoretical ratio expected for optically thin HII regions, corresponding to $\alpha = -0.1$.

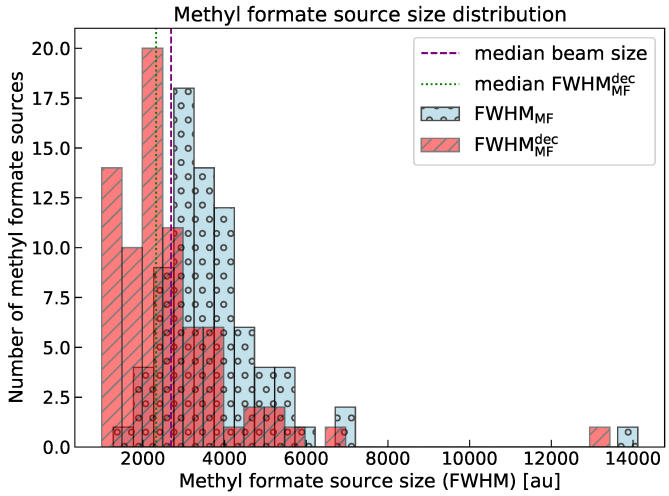

Fig. 11. Methyl formate source size distribution derived fitting 2D Gaussians to the CH_3OCHO moment 0 maps using GExt2D. The non-deconvolved ($FWHM_{MF}$) and deconvolved sizes ($FWHM^{dec}_{MF}$) are shown in blue and red, respectively. The green dotted line shows the median of the deconvolved source sizes, while the dashed purple line shows the median beam size of the line cubes.

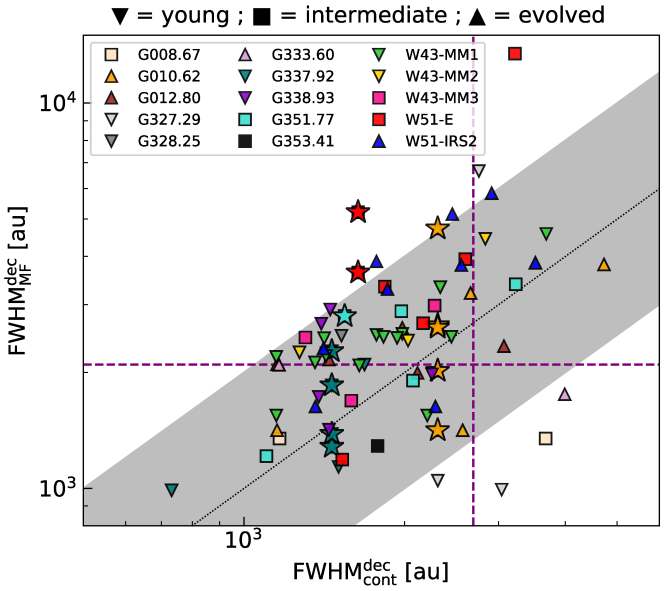

Fig. 12. Methyl formate source sizes derived with GExt2D compared to the associated continuum core sizes taken from the unsmoothed core catalog from Paper XII. All sizes are deconvolved from the beam sizes. The black dotted line shows the one to one ratio, while the gray shaded area shows where the $FWHM^{dec}_{MF}$ sizes are within a factor of 2 of their associated $FWHM^{dec}_{cont}$ sizes. The different symbols represent the different evolutionary stages of the protoclusters: young, intermediate, or evolved, as shown on top of the figure. The methyl formate sources that are not associated with compact continuum cores are shown with stars. For these sources we assumed $FWHM^{dec}_{cont} = \theta^{cont}_{ave}$. The vertical and horizontal dashed lines show the median beam sizes of the line cubes and the continuum maps, respectively.

deconvolution effects that may give excessively small and thus unrealistic sizes. The sizes before ($\theta_{maj} \times \theta_{min}$) and after deconvolution ($\theta^{dec}_{maj} \times \theta^{dec}_{min}$) are listed for each methyl formate source in Table 4, along with physical sizes at the distance of the respective protocluster ($FWHM^{dec}_{MF}$ in au). Figure 11 shows the distribution of the physical sizes before ($FWHM_{MF}$) and after ($FWHM^{dec}_{MF}$) beam deconvolution. The methyl formate sources exhibit deconvolved source sizes ranging from ~990 au to 13400 au, with a median size of about 2300 au. The two outliers of the distribution correspond to W51-E–MF1 and G327.29–MF1. The majority of the sources are marginally resolved, with a handful of sources staying unresolved (i.e., $FWHM^{dec}_{MF}$ < median beam size of the line cubes).

In Figs. 12 and D.1–D.4 we compare the methyl formate deconvolved source sizes to that of their associated continuum cores. While about 74% of the methyl formate sources are found to be more extended than their associated continuum core, overall, for ~87% of the sources, both their methyl formate and continuum emission deconvolved source sizes agree within a factor of 2.

5.4. Temperature estimates

In order to obtain mass estimates of the cores from the thermal dust continuum emission (see Sect. 5.5), the dust temperature, T_d, is a critical parameter. Since for the current analysis we relied only on the CH_3OCHO lines, we needed to adopt an estimate of the temperature that best characterizes the methyl formate sources. CH_3OCHO has a lower binding energy (4210 K; Burke et al. 2015) compared to water (4815 K, Jin et al. in prep.), meaning it is trapped in water ices until the temperature exceeds ~120 K. If the observed methyl formate emission originates only from thermal desorption, CH_3OCHO is released into the gas phase via co-desorption with water above 120 K. At that point we expect a rise in CH_3OCHO abundance within the thermal sublimation radius, which corresponds to the extent of the heated gas traced by CH_3OCHO. Significant thermal desorption still

occurs up to ∼160 K (Bonfand et al. 2019; Garrod et al. 2022). However, as mentioned already in the Introduction, CH_3OCHO has already been observed in the gas phase below the thermal desorption temperature (e.g., Busch et al. 2022; Bouscasse et al. 2024), and shocks from accretion-ejection processes (Palau et al. 2017; Csengeri et al. 2019) can also lead to enhancements of some gas-phase COMs, including methyl formate.

Both gas- and dust-based temperature estimates have been previously performed for the W43 protocluster from the ALMA-IMF data (see Motte et al. 2018b and Paper III). Dust-based temperature estimates using *Herschel* and APEX data with the resolution-improving Point Process Mapping Procedure (PPMAP, Marsh et al. 2015), provided temperatures below 65 K for our sample of methyl formate sources in W43-MM2 and W43-MM3. For the W43-MM1 region, Motte et al. (2018b) derived dust temperatures of 21–93 K for the 14 continuum cores associated with methyl formate sources, while gas-based temperature estimates in Paper IV suggest excitation temperatures of 120–160 K using CH_3CN lines detected toward the seven most massive hot cores. Discrepancies between the dust and gas based temperature estimates may suggest strong temperature gradients toward our compact methyl formate sources and hence the adopted temperatures may be subject to significant uncertainties. For the cold continuum sources, we used here dust-based temperature estimates made using PPMAP by Dell'ova et al. (2024), which allows us to probe the dust temperature at scales larger than 2.5″. These temperature values are, however, not adequate for hot core sources that have deeply embedded internal heating sources on smaller scales.

A few other ALMA-IMF protoclusters have dedicated studies at the spatial resolution of individual cores (see Sect. 4.1). Taniguchi et al. (2023) derived excitation temperatures of ∼200 K toward G010.62, from the analysis of CH_3CN lines observed at 0.3″ resolution (i.e., ∼1500 au at the distance of the protocluster). Law et al. (2021) report higher temperatures, up to 400 K from the analysis of CH_3OH transitions (see their Fig. 6). These results were obtained from ALMA data at the very high angular resolution of 0.14″, which corresponds to a physical scale of ∼700 au at the distance of the protocluster, much smaller than the deconvolved FWHM sizes we derived from the methyl formate emission (i.e., 1400–3800 au); as such, we expect this temperature to be diluted at the resolution of the ALMA-IMF data.

Rotational temperatures of 100 and 165 K have been derived based on the analysis of CH_3OCHO and CH_3OH lines, respectively, detected toward G351.77 in the ATOMS survey (Liu et al. 2021). Furthermore, several 6.7 GHz class II methanol masers have been detected toward G351.77 (see, e.g., Beuther et al. 2009), which suggests gas temperatures ≥100 K (Sobolev et al. 1997; Cragg et al. 2005). Similar to the case of the central bright source of G327.29, which also exhibit a 6.7 GHz class II methanol maser (see, e.g., Wyrowski et al. 2008).

Based on the results listed above, we adopted a canonical dust temperature of 100 ± 50 K for all methyl formate sources, which takes the discrepancies in the temperature estimates previously made toward some of the ALMA-IMF protoclusters into account. There are six exceptions to this assumption where a higher temperature is warranted. In particular, the central bright emission observed in both continuum and COMs toward W51-E has been investigated in detail by Ginsburg et al. (2017), who report a peak excitation temperature >350 K based on the analysis of CH_3OH emission lines (see their Fig. 6) detected in their 0.3″ resolution data, which corresponds to 1800 au at the distance of the protocluster. We assume that this emission mostly comes from the three main, brightest methyl formate sources, W51-E–MF1, MF2, and MF3, for which we adopted a higher dust temperature of 300±100 K.

In the case of W51-IRS2, the bright emission seen toward the northern cores seems to be dominated by the methyl formate sources we have identified as W51-IRS2–MF1 and W51-IRS2–MF3 (see Fig. 4 of Ginsburg et al. 2017). Similar to the W51-E main sources, we adopt a higher dust temperature of 300±100 K for these two objects. This is consistent with the detection of several ammonia (NH_3) masers in this region, which suggests temperatures as high as 300 K (Henkel et al. 2013).

Finally, the central source of G327.29 is somewhat similar to the extreme methyl formate sources in the W51 regions, in terms of its spatial extent and brightness, and it is also associated with several 6.7 Class II methanol masers. Vibrationally excited state transitions of COMs further suggest more elevated temperatures ($T_{\rm rot}$ > 180 K; see Gibb et al. 2000), and hence we also adopt here 300±100 K for the central G327.29–MF1 source.

5.5. Mass estimates

Masses are computed from the 1.3 mm flux density from the getsf-unsmoothed catalog from Paper XII. We take into account potential contamination for free-free emission (Sect. 5.2) and use source specific dust temperature estimates (Sect. 5.4). A previous analysis of the ALMA-IMF data has shown that the most massive objects may reach high densities, for example up to 2×10^8 cm^{-3} in the W43 protocluster (Paper III), and thus the dust thermal continuum emission may become optically thick (see Table C.1). In order to take dust opacities into account in the mass estimates, we used the following equation (Motte et al. 2018b; Pouteau et al. 2022):

$$M_{\rm core} = -\frac{\Omega_{\rm beam} \times d^2}{\kappa_{1.3\rm mm}} \frac{S^{\rm int}_{1.3\rm mm}}{S^{\rm peak}_{1.3\rm mm}} ln\left(1 - \frac{S^{\rm peak}_{1.3\rm mm}}{\Omega_{\rm beam} \times B_{1.3\rm mm}(\rm T_d)}\right), \quad (2)$$

where the 1.3 mm peak and integrated flux, $S^{\rm peak}_{1.3\rm mm}$ and $S^{\rm int}_{1.3\rm mm}$, respectively, are corrected for the free-free contamination (see Sect. 5.2). Following Paper III, we adopted a dust opacity coefficient per unit of mass $\kappa_{1.3\rm mm}$ = 0.01 cm^2 g^{-1} (assuming a gas-to-dust ratio of 100), which is adapted to dense cores (see Ossenkopf & Henning 1994). The distance of the source to the Sun, d is given in Table 1. The solid angle of the continuum beam is given by $\Omega_{\rm beam} = \frac{\pi}{4 \ln 2} \times \theta^{\rm cont\ 2}_{\rm ave}$. Finally, $B_{1.3\rm mm}(T_d)$ is the Planck function at the dust temperature T_d (see Sect. 5.4).

We list in Table C.1 the mass estimates obtained for all methyl formate sources, with dust temperatures ranging from 50 to 150 K (or 200 to 400 K for the most extreme sources; see Sect. 5.4). A factor of 3 of difference in the assumed dust temperature leads to at most a factor of 4.5 of difference in the mass estimates.

Figure 13 shows the distribution of masses of the 76 methyl formate sources computed using a dust temperature of 100 K for all sources, except the most extreme ones for which we used 300 K (see Sect. 5.4). In the top panel of Fig. 13 we also show the mass distribution of all the ALMA-IMF cores, meaning the methyl formate sources plus the compact dust continuum cores from the getsf-unsmoothed catalog (Paper XII), for which the masses were computed using dust temperatures ranging from ∼19–73 K provided by the PPMAP temperature maps built for each protocluster (Dell'ova et al. 2024; see Sect. 5.4). While the methyl formate sources range in mass from ∼0.2 $M_\odot$ to ∼80 $M_\odot$,

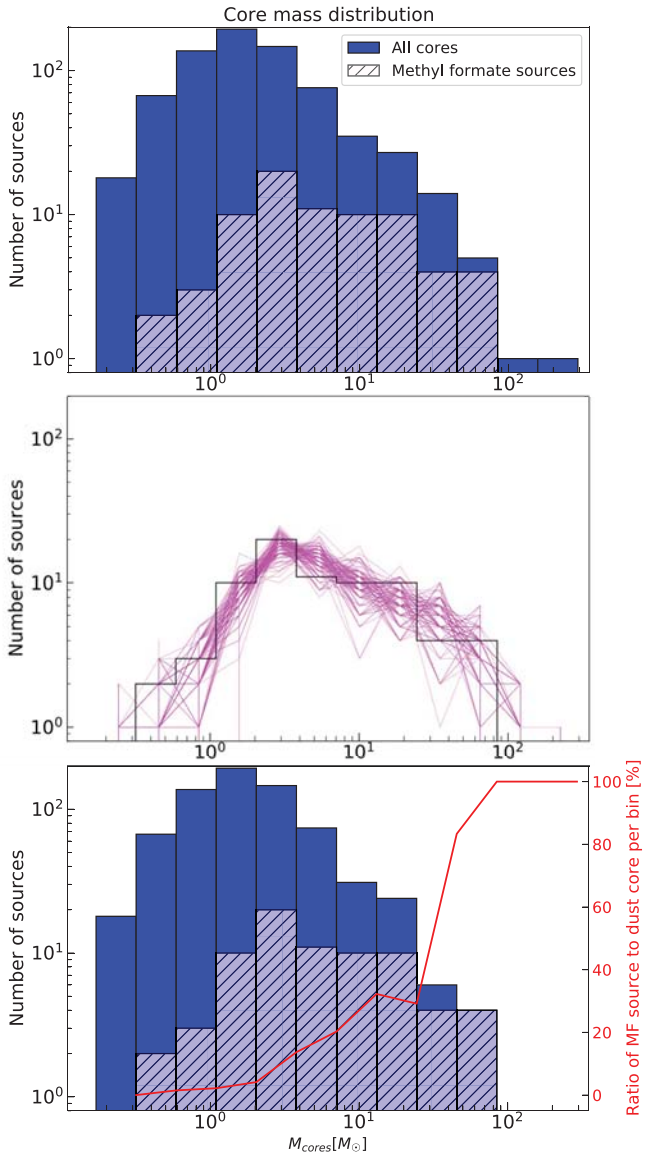

Fig. 13. Mass distribution of the methyl formate sources (black hatched histogram) computed using T_d = 100 K for all sources except the six most extreme ones, for which we used 300 K instead. The magenta lines in the middle panel show in comparison the mass distributions obtained for 100 realizations of randomly sampled temperatures between 50 and 150 K (or 200 and 400 K for the six most extreme sources). The blue histogram in the top panel shows the mass distribution of all cores, i.e., all compact dust continuum cores (without free-free contaminated sources) plus all the methyl formate sources. In the bottom panel we removed from the blue histogram 22 compact dust continuum cores for which the PPMAP method does not provide robust temperature estimates. The red line shows the ratio of methyl formate sources to the total number of cores per bin.

with a median mass of ~3.8 $M_\odot$, the dust continuum cores without methyl formate emission reach masses as high as ~293 $M_\odot$, albeit with a lower median mass of 1.6 $M_\odot$. In the bottom panel of Fig. 13 we also show a mass distribution where we removed 22 dust continuum cores that spatially coincide with extended methyl formate emission, and hence their temperatures estimates could have more significant uncertainties. The PPMAP temperature maps have a 2.5″ angular resolution (Dell'ova et al. 2024), which is insufficient to properly trace the temperature of compact heating sources close to other internally heated sources. These sources are found toward the young protoclusters G327.29, G338.93, W43-MM1, and W43-MM2, the intermediate ones G351.77 and W51-E, and finally the evolved protocluster W51-IRS2 (see the green triangles in Figs. B.1–B.4).

We investigate the fraction of continuum cores associated with compact methyl formate emission with respect to the total population of dust cores. The red line in the bottom panel of Fig. 13 shows that the fraction of compact continuum cores that are associated with methyl formate emission is higher for the most massive cores. Among all the continuum cores that have masses above 8 $M_\odot$, about 41% of are associated with compact methyl formate emission. This ratio increases to 90% if we consider the cores with masses >39 $M_\odot$. Clearly, uncertainty in the temperature estimates for the most massive cores impacts this fraction. To mitigate this, we used 1000 realizations of randomly sampled temperatures from a uniform distribution between 50 and 150 K for all methyl formate sources, and between 200 and 400 K for the six most extreme sources. The middle panel of Fig. 13 shows 100 of the 1000 realizations for the comparison. We find that 38–48% of the dust continuum cores with masses above 8 $M_\odot$ are associated with methyl formate emission, and this ratio increases to 90% for the cores with masses that range between ~30 and 40 $M_\odot$.

6. Discussion

6.1. Chemical origin of the CH_3OCHO emission

CH_3OCHO is expected to form at early times during the star formation process, mainly on the surface of cold interstellar dust grains (20–40 K), through radical-addition reactions (see, e.g., Garrod & Herbst 2006; Garrod et al. 2022). In the classical picture of hot core related chemistry, where we consider hot cores as chemically enhanced regions radiatively heated by a central high-mass, still accreting protostar, the chemical species frozen out onto dust grain ice mantles co-desorb with water into the gas phase when the dust temperature reaches ~120 K (Garrod et al. 2022). As mentioned in Sect. 1, other mechanisms may also be responsible for the presence of CH_3OCHO in the gas phase, in particular at lower temperatures, such as chemical desorption, and grain sputtering due to shocks related to accretion and outflow activity.

In Fig. 14 we compare the 1.3 mm continuum peak flux density to the peak flux measured in the moment 0 maps of methyl formate. We find that the continuum and methyl formate intensity appears to be relatively well correlated, with a Pearson's coefficient $\rho = 0.7$ and assorted with a $P_{value} < 0.001$. About 70% of the methyl formate sources have fluxes within a factor of 2 from the expected value given by a weighted linear fit. This correlation suggests that the methyl formate emission for this sample is likely to share similar chemical origin, assuming that the methyl formate flux densities are directly related to the CH_3OCHO gas-phase abundance. For the rest of the sources, larger discrepancies, up to a factor of 5, are observed (green shaded area). In particular, a group of 26 sources with low peak continuum flux densities, $I^{peak}_{1.3mm}$ = 10–20 mJy beam^{-1}, turn out to have methyl formate fluxes, I^{peak}_{MF}, spread over more than one order of magnitude. For these 26 sources, which are among the faintest methyl formate emitting sources and the faintest continuum sources, the methyl formate detected in the gas phase toward them could thus have a different chemical origin than the rest of the sources.

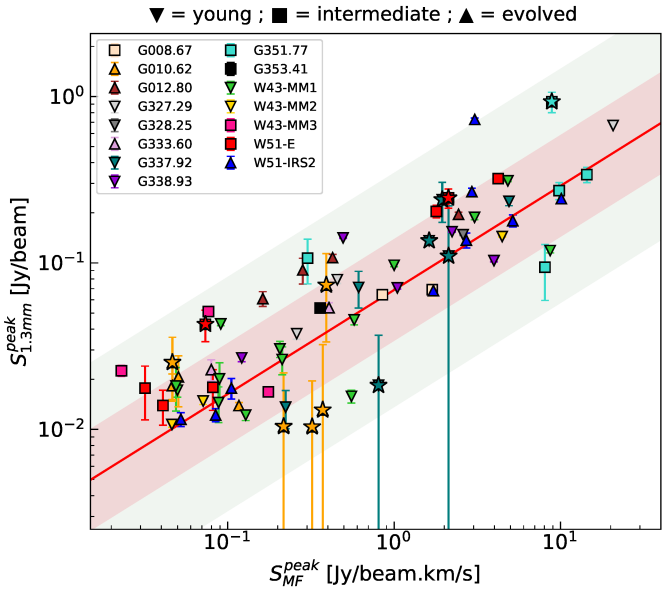

Fig. 14. Peak continuum flux density at 1.3 mm vs. peak flux extracted in the moment 0 maps of CH_3OCHO by GExt2D. The different symbols represent the different evolutionary stages of the protoclusters: young, intermediate and evolved, as indicated on top of the figure, while the stars shows the methyl formate sources that are not associated with any compact dust continuum core. The red line shows a weighted linear fit, while the red an green shaded regions show a factor of 2 and 5 deviation from this fit, respectively.

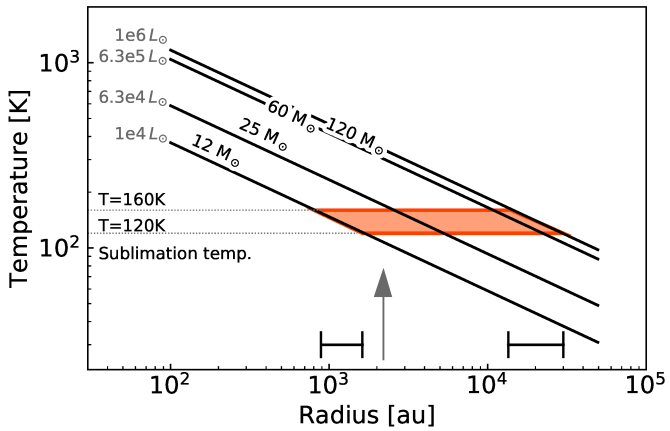

Fig. 15. Temperature profiles as a function of radius for centrally illuminated dusty cores from 12 $M_\odot$ to 120 $M_\odot$, following Wilner et al. (1995). The red shaded area shows the interval that corresponds to the sublimation temperature of the ices (120–160 K). The two horizontal black lines represent the range of radii expected for a heating source with a luminosity of 10^4 $L_\odot$ (12 $M_\odot$) and 10^6 $L_\odot$ (120 $M_\odot$). The gray arrow indicates the median size of the methyl formate sources in our sample.

6.2. Heating sources of hot cores?

Analytical expressions to describe the temperature distribution of a spherically symmetric, centrally illuminated core have been proposed in the literature (Goldreich & Kwan 1974; Wilner et al. 1995). Here we used the relation from Rowan-Robinson (1980), Wolfire & Cassinelli (1986), and Wilner et al. (1995) for a bolometric luminosity (L_{bol}) range between 1 $L_\odot$ and 6×10^6 $L_\odot$:

$$T_d(R) = 37\,\mathrm{K} \times \left(\frac{L}{L_\odot}\right)^{0.25} \times \left(\frac{R}{100\,\mathrm{au}}\right)^{-0.4}. \quad (3)$$

If we assume that the observed CH_3OCHO emission traces the thermal sublimation radius with T_d = 120–160 K (see Sect. 5.4), we can use the measured CH_3OCHO emission sizes to estimate the bolometric luminosity of the heating source and infer the type of the embedded (proto)star. Figure 15 shows that for a heating source with a luminosity of 10^4 $L_\odot$, the minimum radius is about 800–1600 au for CH_3OCHO sublimation at 120–160 K. The smallest deconvolved FWHM sizes for our sample of CH_3OCHO sources are about 990 au. Taking the measured deconvolved FWHM as a radius here, this would correspond to heating sources with $L_{bol} \sim 10^4$ $L_\odot$. This suggests that the population of methyl formate sources could be explained by deeply embedded heating sources corresponding to emerging B0 or earlier type zero-age main-sequence (ZAMS) stars. On the other hand, the most extended, circularly symmetric CH_3OCHO sources (the central sources of G327.29 and W51-E) reaching about 13 400 au sizes could also be consistent with a very luminous single embedded source, because a 10^6 $L_\odot$ heating source would have its CH_3OCHO sublimation radius at 14 000–30 000 au. This size range corresponds well to the largest deconvolved FWHM sizes of CH_3OCHO emitting regions of the ALMA-IMF sample. The population of circularly symmetric isolated CH_3OCHO emission could thus be explained by individual heating sources with $L_{bol} \sim 10^4$–10^6 $L_\odot$. Protostellar evolutionary tracks show that when an emerging protostar reaches about $\sim 10^4$ $L_\odot$, the total luminosity is principally dominated by the protostellar luminosity (Hosokawa & Omukai 2009). Although in these models the ZAMS luminosity and the corresponding mass are highly dependent on the accretion rate, we can tentatively convert these luminosities to stellar masses bearing in mind that our understanding of stars with $M_\star > 60$ $M_\odot$ is very limited. Stellar evolutionary models predict a ZAMS stellar mass of 12 $M_\odot$ for a stellar luminosity of 10^4 $L_\odot$ (Ekström et al. 2012), while a ZAMS stellar mass of 70 $M_\odot$ to a luminosity of 10^6 $L_\odot$. Stellar models, however, have a scatter between 60 $L_\odot$ and 100–120 $M_\odot$ for the high luminosity range (Meynet & Maeder 2000; Martins et al. 2005). Should the methyl formate emission trace gas beyond the sublimation radius (i.e., corresponding to lower temperatures), as suggested by Busch et al. (2022), and Bouscasse et al. (2022, 2024), the inferred luminosities are overestimated by our assumptions here, and consequently also the mass of the central protostar.

Overall, the inferred luminosities likely probe embedded heating sources that could well correspond to high-mass protostars (i.e., precursors of O and early B stars). The most extended sources could be explained by a single luminous protostar with a current stellar mass of about 70–120 $M_\odot$ for the central objects of G327.29 and W51-E, although multiplicity cannot be excluded.

6.3. Nature of the methyl formate sources

To further investigate the nature of the methyl formate sources, we show in Fig. 16 the mass-to-size distribution of our sample of hot core candidates, where the mass corresponds to the core mass inferred from the dust thermal emission (see Sect. 5.5) and the size is derived from the CH_3OCHO emission (see Sect. 5.3). Assuming a 30–100% efficiency for the core mass being converted to stellar mass (see, e.g., Louvet et al. 2014; Könyves et al. 2015), cores with total gas mass above 8–28 $M_\odot$ are expected to form high-mass stars, and thus are excellent candidates for hot cores and their precursors. In total, 38 sources have their highest estimated mass (i.e., for T_d = 50 or 200 K) above 8 $M_\odot$, which

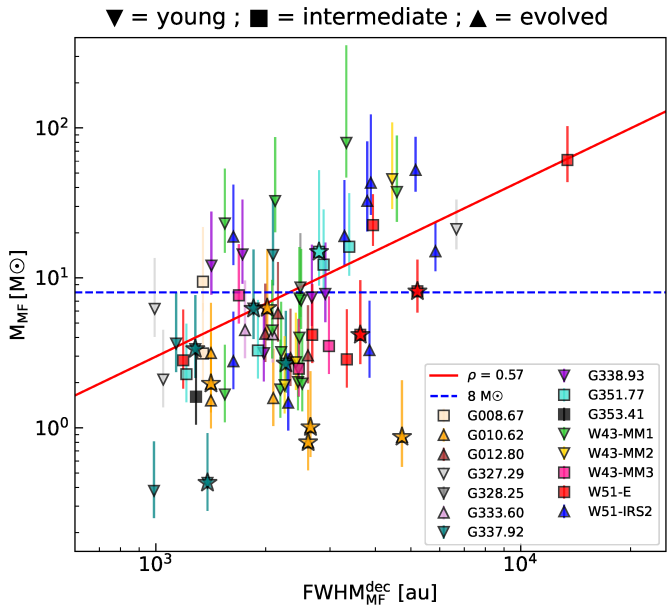

Fig. 16. Mass-to-size plot for the 76 methyl formate sources extracted from the moment 0 maps (Figs. 3–6). The different symbols represent the different evolutionary stages of the protoclusters: young, intermediate and evolved, as indicated on top of the figure, while the stars shows the methyl formate sources that are not associated with any compact dust continuum core. The error bars show the range of masses obtained considering the uncertainties on T_d (300 ± 100K for the most extreme objects and 100 ± 50K for the rest; see Sect. 5.4). The weighted fit to the data points (red line) shows that the most massive cores tend to harbor a more extended emission of methyl formate.

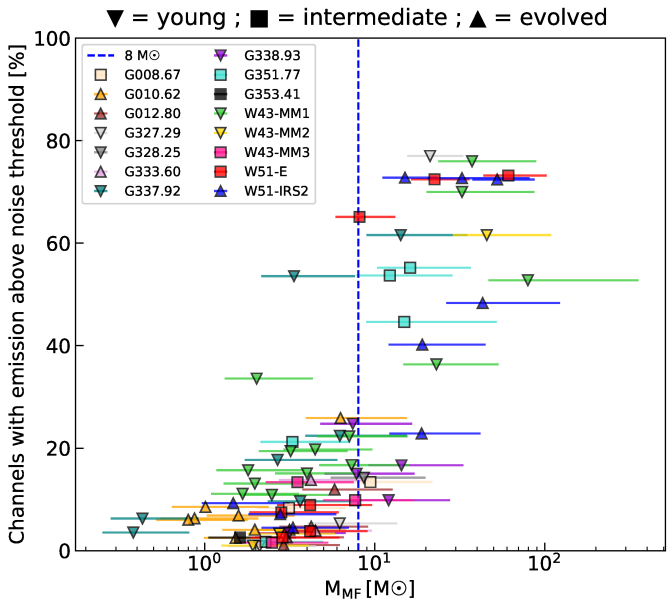

Fig. 17. Number of channels that contain emission above the 3σ noise level in the observed spectrum (Table 4) as a function of the masses of the methyl formate sources. The different symbols represent the different evolutionary stages of the protoclusters: young, intermediate and evolved, as indicated on top of the figure, while the stars shows the methyl formate sources that are not associated with any compact dust continuum core. The horizontal dashed blue line shows the mass threshold of 8 $M_\odot$.

represents about 50% of our sample. This number drops to 22% (i.e., 17 sources) if we consider only a 30% efficiency for converting core mass into stellar mass. The fraction of sources with masses above 8 $M_\odot$ decreases to 24% (i.e., 18 sources), if we consider the lowest estimated mass (i.e., for T_d = 150 or 400 K). This suggests that the majority of the methyl formate sources correspond to low- and intermediate-mass cores.

The 38 methyl formate sources with masses >8 $M_\odot$ in Fig. 16 span a range of deconvolved sizes of over one order of magnitude, from ~1300 au to 13 400 au. This range of masses and sizes correspond to archetypical hot cores (see Table 5) and are >10 times larger compared to hot corinos. These sources are indicated in the last column of Table 4 as HC, or HC* for those whose lowest estimated mass is <8 $M_\odot$. The latest could be interpreted as hot cores around intermediate-mass objects (see, e.g., Fuente et al. 2014). Four of the 38 sources, G010.62–MF3, G337.92–MF3, W51-E–MF2, and G351–MF3, are not associated with any 1.3 mm compact continuum core from the getsf-unsmoothed catalog (see the sources marked with stars in Fig. 16). We also note that five ALMA-IMF protoclusters do not contain any emerging hot cores, which are three evolved clusters, G010.62, G012.80, and G333.60, and two intermediate ones, G353.41 and W43-MM3, where the identified methyl formate sources have low associated core masses.

The rest of the compact methyl formate sources (i.e., 53 sources, which corresponds to ~70% of the sample) have masses <8 $M_\odot$. Such masses would correspond to intermediate-mass and low-mass cores (see Table 5), that is to say, to hot corinos (i.e., chemically active Class 0/I sources). However, these objects have sizes ranging from ~1000 to 4700 au that is still a factor of at least 3 and up to 15 larger than the sizes typically found for hot corinos (see Table 5) and would require sources >10^4 $L_\odot$ as a heating source. The nature of these sources is therefore unclear. Based on the sensitivity of the dataset, we estimated in Paper I that a hot core, like Orion-KL, with spectral lines as bright as ~20–30 K in a 2000 au beam (e.g., Brouillet et al. 2015; Pagani et al. 2017) would be detected in ALMA-IMF, but our sensitivity is insufficient to detect hot corinos like IRAS 16293 (Cazaux et al. 2003) or IRAS 2A (Bottinelli et al. 2007) and IRAS 4B with compact sizes of at most 100 au (Bottinelli et al. 2004). Hence, these detections cannot correspond to the compact, radiatively heated hot gas phase of a hot corino population surrounding low-mass protostars. Instead, such cores could correspond to already formed intermediate to high-mass protostars with a stellar mass of 5–12 $M_\odot$, where most of the core material has been accreted already.

An alternative explanation is that a significant contribution to the observed extended CH_3OCHO emission could originate from spatially extended shocks due to either the ejection or infall

Table 5. Main properties of archetypical hot cores and hot corinos, compared to our source sample.

Source type	Size [au]	M [$M_\odot$]
Hot cores	>2000	8–1000
Hot corinos	<300	<8
Our sources	990–13 400	0.25–263

Notes. See, e.g., Cesaroni et al. (1998); Cesaroni (2005); Widicus Weaver et al. (2017); Sánchez-Monge et al. (2014); Bonfand et al. (2017, 2019) for hot core properties, and Ceccarelli et al. (2000, 2007); Lee et al. (2022); Okoda et al. (2022); Chahine et al. (2022) for hot corinos.

of material. In this scenario the cores would accrete more material from their surroundings. Spatially resolved ALMA observations confirm this scenario for the principal hot core precursor of the G328.25 protocluster, where the extended CH_3OCHO emission, here decomposed into two peak positions, correspond to accretion shocks (see also Csengeri et al. 2018).

In Fig. 17 we present the source line richness as a function of core mass. We show that there is a general trend of more massive cores harboring spectra with more channels with emission above the noise threshold (i.e., being more line rich). All but one sources with more than 36% channels containing emission in their spectra are identified as hot cores (i.e., with masses $>8\,M_\odot$). For the rest of the methyl formate sources, their spectra are found to contain 9–25% of channels with emission. Figure 17 shows that there is no clear threshold between hot cores and lower-mass objects for the sources that have around 20% of their channels containing emission. For this reason, in the current paper we base our source classification on the mass threshold only, while the trends with line richness will be further discussed in a subsequent paper (Csengeri et al., in prep.).

As seen in Sect. 5.2, 19 compact CH_3OCHO sources are associated with extended free-free emission (see Figs. D.1, D.2, and D.4), calling into question the nature of several sources. In particular, toward the G010.62 protocluster, we have estimated that ∼9–100% of the flux measured at 1.3 mm toward the methyl formate sources is due to free-free emission. These sources are spatially coincident with the bright central HII region, suggesting that these sources are more evolved than the two other more isolated sources in the same field (G010.62–MF7 and G010.62–MF10). In particular, the 1.3 mm continuum emission measured toward the sources G010.62–MF1 and G010.62–MF2 is estimated to be 100% due to free-free emission, suggesting that they are entirely surrounded by ionized gas. Visual inspection of their spectra using the ALMA-IMF spw7 in B6 (centered at 232.45 GHz, with a bandwidth of ∼2 GHz), has revealed plenty of strong molecular lines confirming the presence of hot gas rich in COMs, despite the presence of ionized gas. Since the emission of molecular gas is necessarily associated with the presence of dust, this may suggest that our method somewhat overestimates the free-free contribution toward these sources. In fact, for UC-HII regions the emission is often optically thick, while we assumed optically thin emission, and the emitting region for the ionized gas could also be smaller compared to the dust continuum emission. Alternatively, a complex mixture of ionized and molecular gas along the line of sight could also explain our observations. Emission of COMs in the vicinity, or in partial overlap with UC-HII regions has already been observed, for instance toward the Galactic center cloud Sgr B2(N) (see Bonfand et al. 2017). It is also possible that in this field the different observed structures (i.e., methyl formate extended emissions and HII regions) are not part of the same spatially coherent structure; in other words, it is possible that the HII region shell is just expanding and therefore the molecular emission comes from the outside.

Overall, we propose that we see the CH_3OCHO emission arising from different population of sources, with the most massive cores corresponding to hot cores where radiative heating has liberated CH_3OCHO into the gas phase. The origin of CH_3OCHO emission for the lower-mass cores is uncertain. It could be explained either by a continuous accretion and a shock origin related to infall and accretion processes or by having the cores in a more evolved stage where most of the core mass has already been accreted. Cores associated with free-free emission warrant a more precise understanding of the amount of free-free contribution, and represent the latest stages of high-mass star formation where the (proto)star already ionizes its surroundings, and the molecular core material is being exhausted.

6.4. Emergence and lifetime of hot cores

Using the relative fraction of hot cores versus the total number of continuum cores, we can provide a rough estimate for the timescale required for the emergence of hot cores. Similar timescale estimates have been done using source counts to compare hot core to HII region timescales in Wilner et al. (2001). We rely on the assumption that the CH_3OCHO emission originates from the same mechanism over the sample (see, however, Sect. 6.1), and that all objects following the same evolutionary path will develop into radiatively heated hot cores. This is unlikely to hold for the entire sample of CH_3OCHO sources, especially the lower core mass population; therefore, we considered only the highest-mass cores that are the most robust hot core candidates. Figure 13 shows that the relative fraction of dust cores with and without hot core emission increases with the core mass, which supports the picture where all massive cores go through the hot core stage. We notice that above a mass threshold of $\sim 8\,M_\odot$, this fraction increases from ∼20 to 100% increasing with core mass. We assume a timescale for the protostellar phase of 3×10^5 yr based on Duarte-Cabral et al. (2013) and also used in Csengeri et al. (2014). For a core mass range between 30 and 50 $M_\odot$, the fraction of hot cores to the total number of dust cores rapidly increases to 30–80%. Adopting a constant 3×10^5 yr timescale for the protostellar phase over this mass range, we find that the timescales for the hot core phase is between 0.9×10^5 yr and 2.4×10^5 yr. Uncertainties only due to the mass estimates and the protostellar lifetime itself can lead to variations of a factor of a few. Since we do not have a full statistics of the more evolved HC-UC-HII stages, this estimate does not account for a potential overlap in the hot core and HC-UC-HII phase.

6.5. What type of clouds host massive hot cores?

Figure 8 shows that the highest ratios of methyl formate sources to continuum cores (≤25%) are found toward the five following protoclusters: G351.77, G337.92, G010.62, W43-MM1, and W51-E, with no obvious correlation with their evolutionary stage. They all contain at least one massive (i.e., $>8\,M_\odot$) hot core, except for G010.62, the brightest central region of which is strongly contaminated by free-free emission. In particular, 100% of the continuum flux measured at 1.3 mm toward the two brightest methyl formate sources, G010.62–MF1 and MF2 have been attributed to free-free emission (see Sect. 6.3), preventing us from computing mass estimates for these sources. Furthermore, we found five methyl formate sources without an associated compact continuum core in this region, which may lead to inaccurate extraction of the flux from the continuum maps, and thus inaccurate mass estimates (see Sect. 5.1 and Table C.1). In addition to G010.62, we find four other ALMA-IMF protoclusters that do not contain any massive hot cores, the two evolved clusters, G012.80 and G333.60, and two intermediate ones, G353.41 and W43-MM3.

Figure 18 highlights the hot cores with masses above $8\,M_\odot$, which are found toward ten ALMA-IMF protoclusters, with no obvious correlation with their evolutionary stage. The ten clouds span a mass range from $2.5 \times 10^3\,M_\odot$ to $32.7 \times 10^3\,M_\odot$, suggesting that the presence of massive hot cores does not depend on the total mass of the protocluster either.

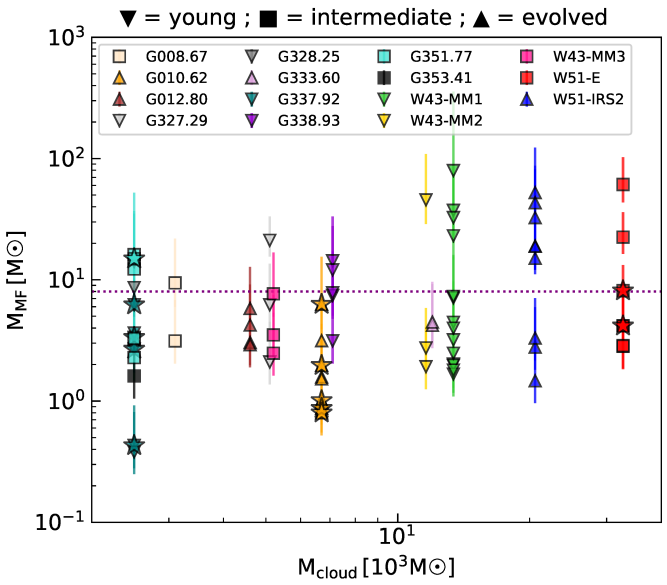

Fig. 18. Mass distribution of the methyl formate sources as a function of their parent cloud mass. The different symbols represent the different evolutionary stages of the protoclusters: young, intermediate and evolved, as indicated on top of the figure, while the stars shows the methyl formate sources that are not associated with any compact dust continuum core. The error bars show the range of masses obtained considering the uncertainties on T_d (300 ± 100K for the most extreme objects and 100 ± 50K for the rest; see Sect. 5.4). The horizontal dotted line shows the 8 $M_\odot$ mass threshold.

6.6. G353.41: A chemically inactive massive protocluster?

G353.41 is an intermediate evolutionary stage protocluster that is very bright in the continuum at 1.3 mm, and strongly affected by ionized gas coming from UC-HII regions (see Fig. 2 of Paper I). This region is a remarkable outlier of the ALMA-IMF hot core sample as it hosts only one weak, low-mass (<2 $M_\odot$) compact methyl formate source. Despite the fact that it hosts as many as 57 compact dust continuum cores, these are mainly low-to intermediate-mass cores, with masses that range from 0.2 to 9.8 $M_\odot$ (see Paper XII). A visual inspection of the ALMA-IMF spectra in B6 spw7 (centered at 232.45 GHz, with a bandwidth of ~2 GHz) extracted toward the three more massive cores (i.e., >7 $M_\odot$) did not reveal any strong molecular lines, confirming the lack of hot gas rich in COMs. It suggests that despite being massive, and qualifying for the ALMA-IMF selection, this protocluster is likely to form only low- to intermediate-mass stars, and lacks strong emission from COMs. It is yet unclear what physical conditions can explain this characteristics, a more complete investigation of the overall energetics of the protocluster is needed to discuss the potential origin of its chemically poor stage.

7. Summary

We have investigated the spatial distribution of methyl formate emission toward 15 massive protoclusters targeted by the ALMA-IMF Large Program. Methyl formate is a complex species commonly detected in star-forming regions, and we used it to search for hot core candidates in our dataset. We computed and analyzed moment 0 maps, combining two strong transitions of methyl formate at 216.2 GHz with E_{up}/k = 109 K. We used a source-extraction algorithm to extract and characterize the cores that have methyl formate emission. We cross-matched our catalog of methyl formate sources with that of the compact continuum cores of the ALMA-IMF dataset in order to derive and compare their physical properties and constrain their nature. Our main findings are summarized below:

1. We find that, in most cases, methyl formate traces compact sources, both clustered and isolated, with sizes (FWHM) between ~1000 and 6000 au and median extents of ~2300 au. There are two outliers in the two young protoclusters, G327.29 and W51-E, with more extended emission of methyl formate above 6000 au and reaching 13 400 au.
2. We built a catalog of 76 compact methyl formate sources, which is about an order of magnitude fewer compared to the number of purely dust continuum cores extracted from the ALMA-IMF dataset. We identified 56 of these methyl formate sources (i.e., 76% of the sample) as new detections.
3. We find an increasing trend in the number of methyl formate sources as a function of the number of continuum cores per protocluster, but the ratio of hot core candidates to dust continuum cores never exceeds 25% per protocluster. We find no clear correlation between the number of methyl formate sources and the clump mass, nor the evolutionary stage of the protocluster, suggesting that the number of hot core candidates is independent of the properties of their host protocluster.
4. Assuming a mean dust temperature of 100 K, we estimated core masses ranging from ~0.2 $M_\odot$ to 80 $M_\odot$ for the sources that have methyl formate emission. We find that the relative fraction of compact continuum cores with and without methyl formate emission increases with the core mass, which supports the idea that all massive cores go through the hot core stage.
5. We show that the population of hot core candidates could be explained by deeply embedded heating sources corresponding to high-mass protostars (i.e., emerging B0 or earlier-type ZAMS stars) with L_{bol} ~10^4–10^6 $L_\odot$. The most extended sources (i.e., the central sources G327.29 and W51-E, with sizes of about 13 400 au) can also be explained by a single, very luminous embedded source with 10^6 $L_\odot$, although multiplicity at smaller scales cannot be excluded.
6. We find that about 50% of the methyl formate sources have masses above 8 $M_\odot$ and span a range of sizes (FWHM) from 1300 to 13 400 au, which is in line with archetypical hot cores. The rest of the compact methyl formate sources have masses <8 $M_\odot$ and sizes ranging from 1000 to 4700 au, making them intermediate-mass objects; where a significant contribution from spatially extended shocks could also explain the observed CH_3OCHO emission.
7. Considering the fraction of cores with hot core emission and assuming a timescale for the protostellar phase of 3×10^5 yr, we find that massive cores spend at least 1.5×10^5 yr in the hot core phase.
8. We find that all protoclusters harbor at least one methyl formate source and that ten out of the 15 contain massive hot cores, suggesting that the presence of massive hot cores depends neither on the total mass of the protocluster nor on its evolutionary stage. We find one outlier, G353.41, that clearly lacks strong emission from COMs.

Overall, we propose that the methyl formate emission arises from different population of objects over the ALMA-IMF target regions, with the most massive cores corresponding to centrally heated hot cores. In these cores, CH_3OCHO is released into the gas phase via thermal desorption, and the origin of CH_3OCHO emission for the lower-mass cores could be explained either by

shocks related to infall and accretion processes or by the cores being in a more evolved stage, where most of the core mass has already been accreted to form intermediate- to high-mass protostars.

Acknowledgements. We thank the referee for the careful reading of the manuscript and providing useful comments. This paper makes use of the ALMA data ADS/JAO.ALMA2017.1.01355.L. ALMA is a partnership of ESO (representing its member states), NSF (USA) and NINS (Japan), together with NRC (Canada), MOST and ASIAA (Taiwan), and KASI (Republic of Korea), in cooperation with the Republic of Chile. The Joint ALMA Observatory is operated by ESO, AUI/NRAO and NAOJ. This project has received funding from the European Research Council (ERC) via the ERC Synergy Grant ECOGAL (grant 855130), from the French Agence Nationale de la Recherche (ANR) through the project COSMHIC (ANR-20-CE31-0009), and the French Programme National de Physique Stellaire and Physique et Chimie du Milieu Interstellaire (PNPS and PCMI) of CNRS/INSU (with INC/INP/IN2P3). The project leading to this publication has received support from ORP, that is funded by the European Union's Horizon 2020 research and innovation programme under grant agreement No 101004719 [ORP]. M.B. thanks R. T. Garrod for the fruitful discussions on the chemical origin of methyl formate. M.B. thanks J. Pety for providing the equations for the source size deconvolution. M.B. is currently a postdoctoral fellow in the University of Virginia's VICO collaboration and is funded by grants from the NASA Astrophysics Theory Program (grant number 80NSSC18K0558) and the NSF Astronomy & Astrophysics program (grant number 2206516). T.Cs. has received financial support from the French State in the framework of the IdEx Université de Bordeaux Investments for the future Program. S.B. acknowledges support by the French Agence Nationale de la Recherche (ANR) through the project GENESIS (ANR-16-CE92-0035-01). F.M., N.C., and Y.P. acknowledge the COSMHIC ANR and the ECOGAL ERC. A.G. acknowledges support from the National Science Foundation under grant AST-2008101. R.G.-M. acknowledges support from UNAM-PAPIIT project IN104319 and from CONACyT Ciencia de Frontera project ID: 86372. A.S. gratefully acknowledges support by the Fondecyt Regular (projectcode 1220610), and ANID BASAL projects ACE210002 and FB210003. R.A. gratefully acknowledges support from ANID Beca Doctorado Nacional 21200897. A.L.S. acknowledges funding from the European Research Council (ERC) under the European Union's Horizon 2020 research and innovation programme, for the Project "The Dawn of Organic Chemistry " (DOC), grant agreement No 741002. L.B. gratefully acknowledges support by the ANID BASAL project FB210003.

References

Allen, V., van der Tak, F. F. S., & Walsh, C. 2018, A&A, 616, A67
Anglada, G., Rodríguez, L. F., & Carrasco-González, C. 2018, A&A Rev., 26, 3
Bacmann, A., Taquet, V., Faure, A., Kahane, C., & Ceccarelli, C. 2012, A&A, 541, L12
Balucani, N., Ceccarelli, C., & Taquet, V. 2015, MNRAS, 449, L16
Balucani, N., Skouteris, D., Ceccarelli, C., et al. 2018, Mol. Astrophys., 13, 30
Belloche, A., Müller, H. S. P., Menten, K. M., Schilke, P., & Comito, C. 2013, A&A, 559, A47
Belloche, A., Müller, H. S. P., Garrod, R. T., & Menten, K. M. 2016, A&A, 587, A91
Belloche, A., Garrod, R. T., Müller, H. S. P., et al. 2019, A&A, 628, A10
Beuther, H., Zhang, Q., Bergin, E. A., & Sridharan, T. K. 2009, AJ, 137, 406
Beuther, H., Walsh, A. J., Johnston, K. G., et al. 2017, A&A, 603, A10
Bisschop, S. E., Schilke, P., Wyrowski, F., et al. 2013, A&A, 552, A122
Bonfand, M., Belloche, A., Menten, K. M., Garrod, R. T., & Müller, H. S. P. 2017, A&A, 604, A60
Bonfand, M., Belloche, A., Garrod, R. T., et al. 2019, A&A, 628, A27
Bottinelli, S., Ceccarelli, C., Lefloch, B., et al. 2004, ApJ, 615, 354
Bottinelli, S., Ceccarelli, C., Williams, J. P., & Lefloch, B. 2007, A&A, 463, 601
Bouscasse, L., Csengeri, T., Belloche, A., et al. 2022, A&A, 662, A32
Bouscasse, L., Csengeri, T., Wyrowski, F., Menten, K. M., & Bontemps, S. 2024, A&A, 686, A252
Brouillet, N., Despois, D., Lu, X. H., et al. 2015, A&A, 576, A129
Brouillet, N., Despois, D., Molet, J., et al. 2022, A&A, 665, A140
Burke, D. J., Puletti, F., Brown, W. A., et al. 2015, MNRAS, 447, 1444
Busch, L. A., Belloche, A., Garrod, R. T., Müller, H. S. P., & Menten, K. M. 2022, A&A, 665, A96
Cazaux, S., Tielens, A. G. G. M., Ceccarelli, C., et al. 2003, ApJ, 593, L51
Ceccarelli, C. 2004, ASP Conf. Ser., 323, 195
Ceccarelli, C., Loinard, L., Castets, A., Tielens, A. G. G. M., & Caux, E. 2000, A&A, 357, L9
Ceccarelli, C., Caselli, P., Herbst, E., Tielens, A. G. G. M., & Caux, E. 2007, in Protostars and Planets V, eds. B. Reipurth, D. Jewitt, & K. Keil (Tucson: University of Arizona Press), 47
Ceccarelli, C., Codella, C., Balucani, N., et al. 2022, arXiv e-prints, [arXiv:2206.13270]
Cernicharo, J., Marcelino, N., Roueff, E., et al. 2012, ApJ, 759, L43
Cernicharo, J., Kisiel, Z., Tercero, B., et al. 2016, A&A, 587, L4
Cesaroni, R. 2005, Ap&SS, 295, 5
Cesaroni, R., Hofner, P., Walmsley, C. M., & Churchwell, E. 1998, A&A, 331, 709
Chahine, L., López-Sepulcre, A., Neri, R., et al. 2022, A&A, 657, A78
Charnley, S. B., Tielens, A. G. G. M., & Millar, T. J. 1992, ApJ, 399, L71
Coletta, A., Fontani, F., Rivilla, V. M., et al. 2020, A&A, 641, A54
Cragg, D. M., Sobolev, A. M., & Godfrey, P. D. 2005, MNRAS, 360, 533
Csengeri, T., Urquhart, J. S., Schuller, F., et al. 2014, A&A, 565, A75
Csengeri, T., Bontemps, S., Wyrowski, F., et al. 2017, A&A, 601, A60
Csengeri, T., Bontemps, S., Wyrowski, F., et al. 2018, A&A, 617, A89
Csengeri, T., Belloche, A., Bontemps, S., et al. 2019, A&A, 632, A57
Cunningham, N., Ginsburg, A., Galván-Madrid, R., et al. 2023, A&A, 678, A194
Dell'ova, P., Motte, F., Gusdorf, A., et al. 2024, A&A, in press, https://doi.org/10.1051/0004-6361/202348984
Duarte-Cabral, A., Bontemps, S., Motte, F., et al. 2013, A&A, 558, A125
Ekström, S., Georgy, C., Eggenberger, P., et al. 2012, A&A, 537, A146
Fuente, A., Cernicharo, J., Caselli, P., et al. 2014, A&A, 568, A65
Galván-Madrid, R., Díaz-Gonzáles, D. J., Motte, F., et al. 2024, ApJS, submitted
Garrod, R. T. 2013, ApJ, 765, 60
Garrod, R. T., & Herbst, E. 2006, A&A, 457, 927
Garrod, R. T., Wakelam, V., & Herbst, E. 2007, A&A, 467, 1103
Garrod, R. T., Jin, M., Matis, K. A., et al. 2022, ApJS, 259, 1
Gibb, E. L., Whittet, D. C. B., Schutte, W. A., et al. 2000, ApJ, 536, 347
Gieser, C., Beuther, H., Semenov, D., et al. 2021, A&A, 648, A66
Ginsburg, A., Goss, W. M., Goddi, C., et al. 2016, A&A, 595, A27
Ginsburg, A., Goddi, C., Kruijssen, J. M. D., et al. 2017, ApJ, 842, 92
Ginsburg, A., Csengeri, T., Galván-Madrid, R., et al. 2022, A&A, 662, A9
Goddi, C., Ginsburg, A., Maud, L. T., Zhang, Q., & Zapata, L. A. 2020, ApJ, 905, 25
Goldreich, P., & Kwan, J. 1974, ApJ, 189, 441
Hasegawa, T. I., & Herbst, E. 1993, MNRAS, 263, 589
Henkel, C., Wilson, T. L., Asiri, H., & Mauersberger, R. 2013, A&A, 549, A90
Herbst, E., & van Dishoeck, E. F. 2009, ARA&A, 47, 427
Hernández-Hernández, V., Zapata, L., Kurtz, S., & Garay, G. 2014, ApJ, 786, 38
Hosokawa, T., & Omukai, K. 2009, ApJ, 691, 823
Imai, M., Oya, Y., Svoboda, B., et al. 2022, ApJ, 934, 70
Immer, K., Galván-Madrid, R., König, C., Liu, H. B., & Menten, K. M. 2014, A&A, 572, A63
Ishibashi, A., Hidaka, H., Oba, Y., Kouchi, A., & Watanabe, N. 2021, ApJ, 921, L13
Jin, M., & Garrod, R. T. 2020, ApJS, 249, 26
Jørgensen, J. K., Favre, C., Bisschop, S. E., et al. 2012, ApJ, 757, L4
Jørgensen, J. K., Belloche, A., & Garrod, R. T. 2020, ARA&A, 58, 727
Jorsater, S., & van Moorsel, G. A. 1995, AJ, 110, 2037
Keto, E., Zhang, Q., & Kurtz, S. 2008, ApJ, 672, 423
Könyves, V., André, P., Men'shchikov, A., et al. 2015, A&A, 584, A91
Kurtz, S., Cesaroni, R., Churchwell, E., Hofner, P., & Walmsley, C. M. 2000, in Protostars and Planets IV, eds. V. Mannings, A. P. Boss, & S. S. Russell (Tucson: University of Arizona Press), 299
Law, C. J., Zhang, Q., Öberg, K. I., et al. 2021, ApJ, 909, 214
Lee, C.-F., Codella, C., Ceccarelli, C., & López-Sepulcre, A. 2022, ApJ, 937, 10
Leurini, S., Hieret, C., Thorwirth, S., et al. 2008, A&A, 485, 167
Leurini, S., Herpin, F., van der Tak, F., et al. 2017, A&A, 602, A70
Liu, H. B., Chen, H.-R. V., Román-Zúñiga, C. G., et al. 2019, ApJ, 871, 185
Liu, T., Evans, N. J., Kim, K.-T., et al. 2020, MNRAS, 496, 2790
Liu, H.-L., Liu, T., Evans, Neal J., I., et al. 2021, MNRAS, 505, 2801
Lo, N., Wiles, B., Redman, M. P., et al. 2015, MNRAS, 453, 3245
Louvet, F., Motte, F., Hennebelle, P., et al. 2014, A&A, 570, A15
Louvet, F., Sanhueza, P., Stutz, A., et al. 2024, A&A, submitted
Marsh, K. A., Whitworth, A. P., & Lomax, O. 2015, MNRAS, 454, 4282
Martins, F., Schaerer, D., & Hillier, D. J. 2005, A&A, 436, 1049
McGuire, B. A. 2022, ApJS, 259, 30
Mehringer, D. M. 1994, ApJS, 91, 713
Men'shchikov, A. 2021, A&A, 649, A89
Meynet, G., & Maeder, A. 2000, A&A, 361, 101
Molinari, S., Schisano, E., Faustini, F., et al. 2011, A&A, 530, A133
Motte, F., Bontemps, S., Schilke, P., et al. 2007, A&A, 476, 1243
Motte, F., Bontemps, S., & Louvet, F. 2018a, ARA&A, 56, 41
Motte, F., Nony, T., Louvet, F., et al. 2018b, Nat. Astron., 2, 478
Motte, F., Bontemps, S., Csengeri, T., et al. 2022, A&A, 662, A8
Nony, T., Galván-Madrid, R., Motte, F., et al. 2023, A&A, 674, A75

Okoda, Y., Oya, Y., Imai, M., et al. 2022, ApJ, 935, 136
Ossenkopf, V., & Henning, T. 1994, A&A, 291, 943
Pagani, L., Favre, C., Goldsmith, P. F., et al. 2017, A&A, 604, A32
Palau, A., Walsh, C., Sánchez-Monge, Á., et al. 2017, MNRAS, 467, 2723
Pearson, J. C., Müller, H. S. P., Pickett, H. M., Cohen, E. A., & Drouin, B. J. 2010, J. Quant. Spectrosc. Radiat. Transf., 111, 1614
Pouteau, Y., Motte, F., Nony, T., et al. 2022, A&A, 664, A26
Pouteau, Y., Motte, F., Nony, T., et al. 2023, A&A, 674, A76
Richard, C., Margulès, L., Caux, E., et al. 2013, A&A, 552, A117
Rivilla, V. M., Beltrán, M. T., Martín-Pintado, J., et al. 2017, A&A, 599, A26
Rowan-Robinson, M. 1980, ApJS, 44, 403
Sánchez-Monge, Á., Beltrán, M. T., Cesaroni, R., et al. 2014, A&A, 569, A11
Sánchez-Monge, Á., Schilke, P., Ginsburg, A., Cesaroni, R., & Schmiedeke, A. 2018, A&A, 609, A101
Schuller, F., Menten, K. M., Contreras, Y., et al. 2009, A&A, 504, 415
Sobolev, A. M., Cragg, D. M., & Godfrey, P. D. 1997, A&A, 324, 211
Tan, J. C., Kong, S., Butler, M. J., Caselli, P., & Fontani, F. 2013, ApJ, 779, 96
Taniguchi, K., Sanhueza, P., Olguin, F. A., et al. 2023, ApJ, 950, 57
Taquet, V., López-Sepulcre, A., Ceccarelli, C., et al. 2015, ApJ, 804, 81
Tercero, B., Cuadrado, S., López, A., et al. 2018, A&A, 620, L6
Terebey, S., Chandler, C. J., & Andre, P. 1993, ApJ, 414, 759
Vastel, C., Ceccarelli, C., Lefloch, B., & Bachiller, R. 2014, ApJ, 795, L2
Vasyunin, A. I., & Herbst, E. 2013, ApJ, 769, 34
Widicus Weaver, S. L., Laas, J. C., Zou, L., et al. 2017, ApJS, 232, 3
Wilner, D. J., Welch, W. J., & Forster, J. R. 1995, ApJ, 449, L73
Wilner, D. J., De Pree, C. G., Welch, W. J., & Goss, W. M. 2001, ApJ, 550, L81
Wolfire, M. G., & Cassinelli, J. P. 1986, ApJ, 310, 207
Wyrowski, F., Bergman, P., Menten, K., et al. 2008, Ap&SS, 313, 69
Zhang, Q., & Ho, P. T. P. 1997, ApJ, 488, 241
Zhang, Q., Ho, P. T. P., & Ohashi, N. 1998, ApJ, 494, 636

[1] Departments of Astronomy and Chemistry, University of Virginia, Charlottesville, VA 22904, USA
e-mail: pgu4gb@virginia.edu
[2] Laboratoire d'Astrophysique de Bordeaux, Univ. Bordeaux, CNRS, B18N, allée Geoffroy Saint-Hilaire, 33615 Pessac, France
[3] Univ. Grenoble Alpes, CNRS, IPAG, 38000 Grenoble, France
[4] Department of Astronomy, University of Florida, PO Box 112055, USA
[5] Instituto de Radioastronomía y Astrofísica, Universidad Nacional Autónoma de México, Morelia, Michoacán 58089, Mexico
[6] Max-Planck Institut für Radioastronomie, Auf dem Hügel 69, 53121 Bonn, Germany
[7] Departamento de Astronomía, Universidad de Concepción, Casilla 160-C, 4030000 Concepción, Chile
[8] Max-Planck-Institute for Astronomy, Königstuhl 17, 69117 Heidelberg, Germany
[9] Herzberg Astronomy and Astrophysics Research Centre, National Research Council of Canada, 5071 West Saanich Road, Victoria, BC V9E 2E7 Canada
[10] Laboratoire de Physique de l'École Normale Supérieure, ENS, Univ. PSL, CNRS, Sorbonne Université, Université de Paris, Paris, France
[11] Observatoire de Paris, PSL University, Sorbonne Université, LERMA, 75014 Paris, France
[12] Instituto Argentino de Radioastronomía (CCT-La Plata, CONICET; CICPBA), C.C. No. 5, 1894, Villa Elisa, Buenos Aires, Argentina
[13] Department of Astronomy, Yunnan University, Kunming, 650091, PR China
[14] National Astronomical Observatory of Japan, National Institutes of Natural Sciences, 2-21-1 Osawa, Mitaka, Tokyo 181-8588, Japan
[15] Department of Astronomical Science, SOKENDAI (The Graduate University for Advanced Studies), 2-21-1 Osawa, Mitaka, Tokyo 181-8588, Japan
[16] Institute of Astronomy, National Tsing Hua University, Hsinchu 30013, Taiwan
[17] Institut de Radioastronomie Millimétrique (IRAM), 300 rue de la Piscine, 38406 Saint-Martin-D'Hères, France
[18] Steward Observatory, University of Arizona, 933 North Cherry Avenue, Tucson, AZ 85721, USA
[19] Departamento de Astronomía, Universidad de Chile, Casilla 36-D, Santiago, Chile

Appendix A: CH_3OCHO spectra

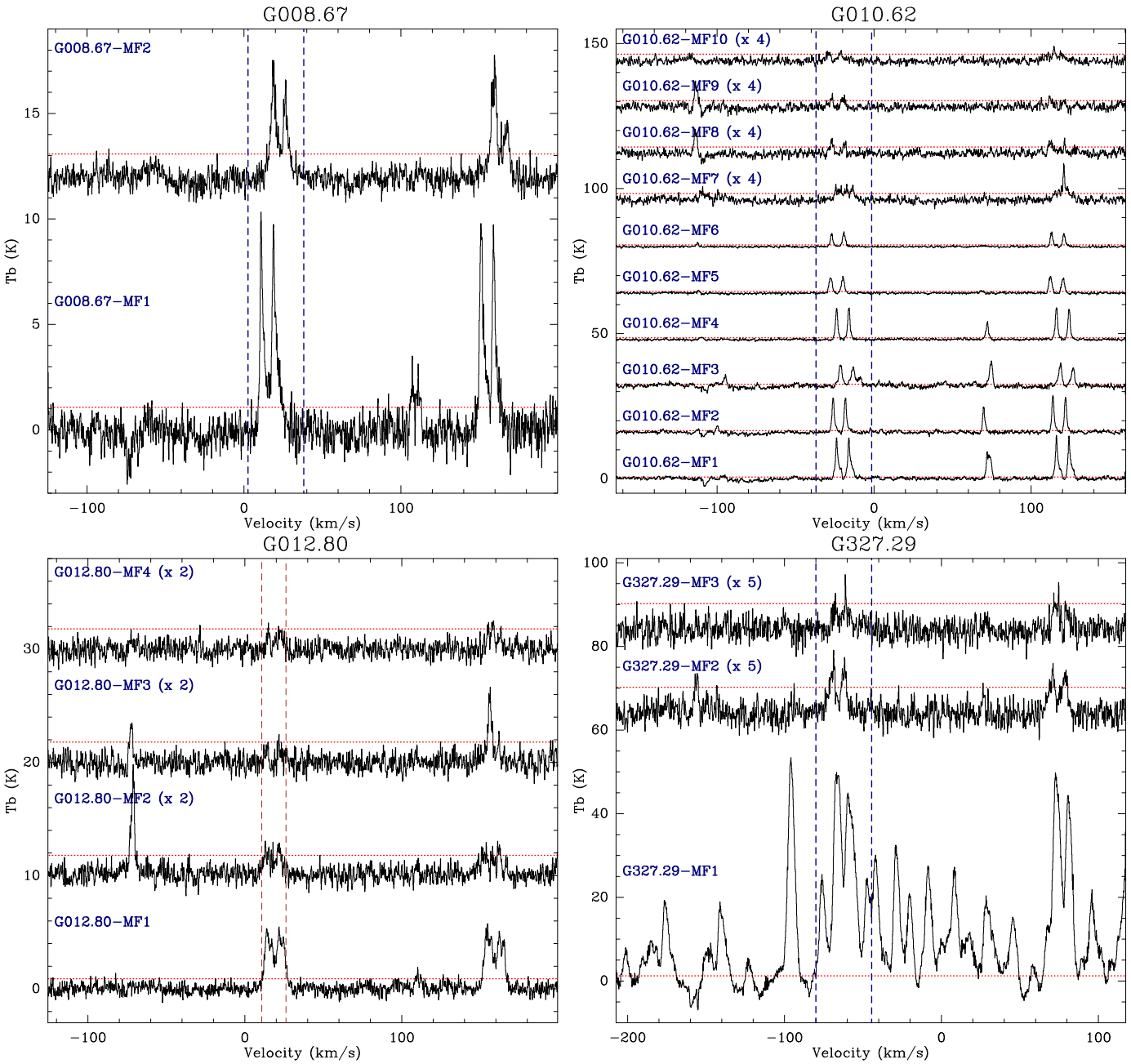

Fig. A.1: Single-pixel continuum-subtracted spectra extracted toward the peak position of the compact methyl formate sources in the ALMA-IMF protoclusters. The spectra are shifted along the y axis and the value in parentheses (if any), indicates the scaling factor applied to the spectrum. The vertical dashed lines show the velocity range used to compute the methyl formate moment 0 maps as in Fig. 2. The red horizontal dotted lines show the 3σ threshold, using the rms noise level measured in the line cubes (see Table 2). The figure continues on the next page.

In Fig. A.1 we present the single-pixel continuum-subtracted spectra extracted from the ALMA-IMF B6-spw0 line cubes toward the position of all methyl formate sources in each of the 15 protoclusters.

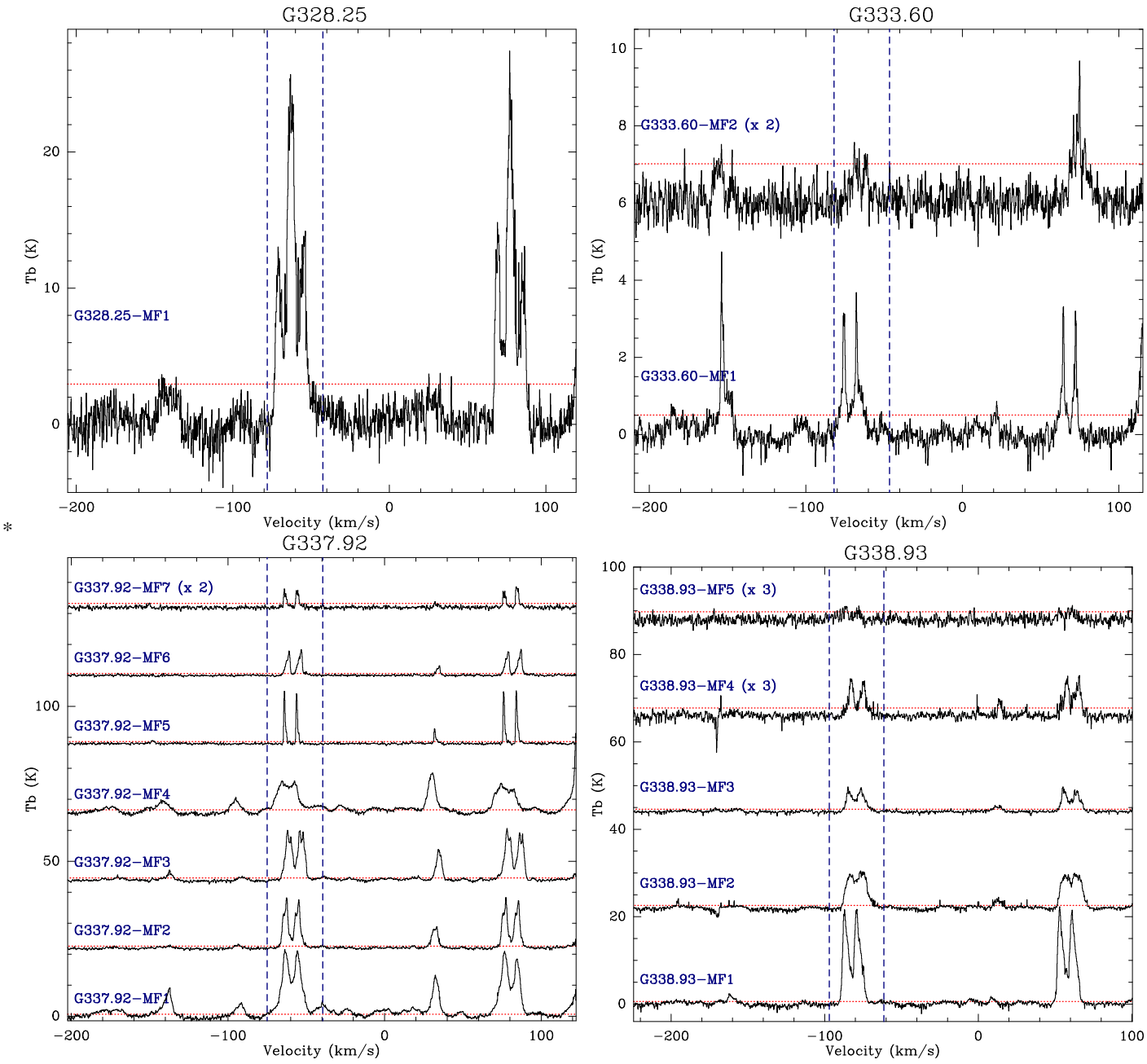

Fig. A.1: Continued.

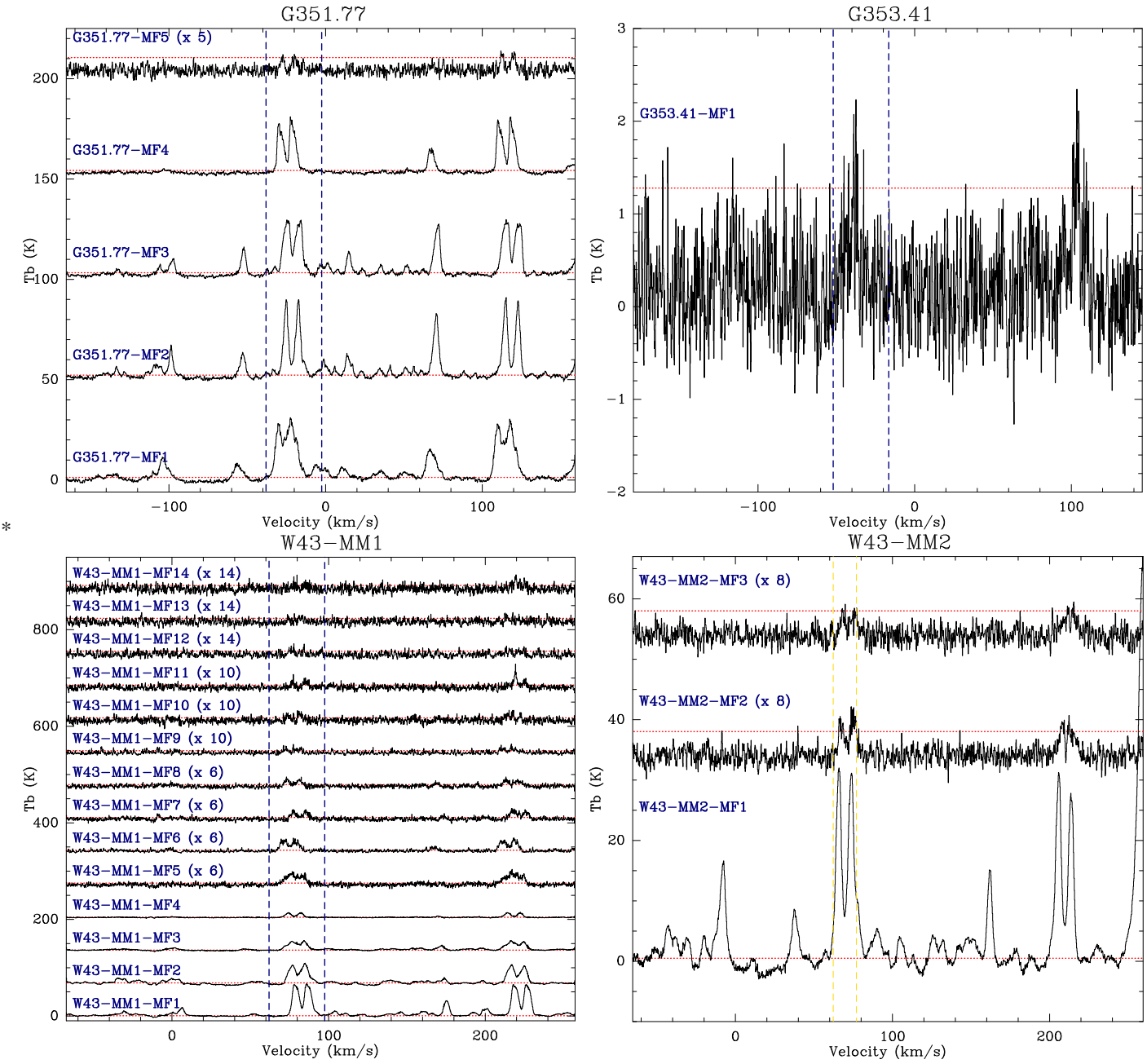

Fig. A.1: Continued.

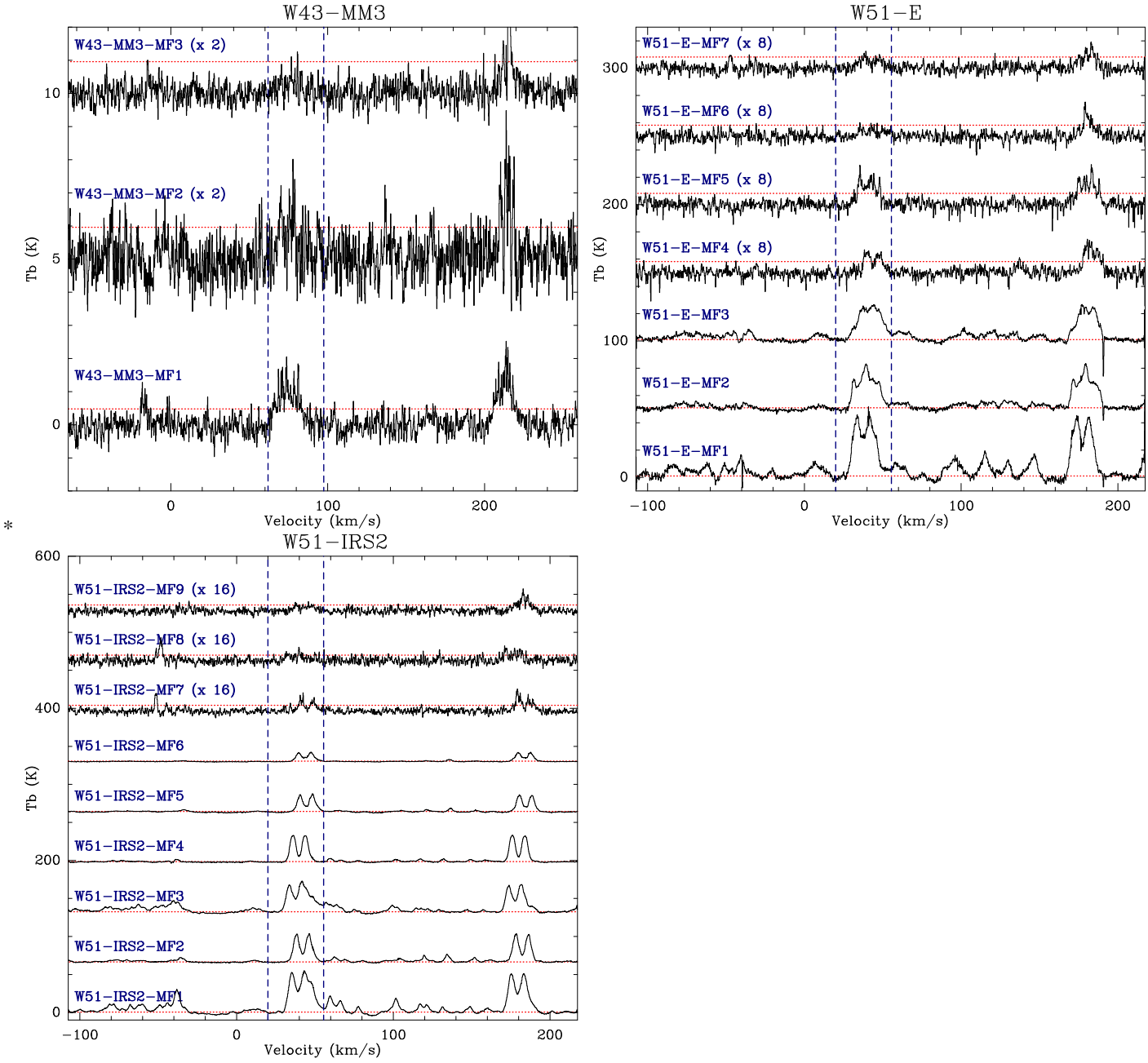

Fig. A.1: Continued.

Appendix B: Continuum emission compared with CH_3OCHO spatial distribution

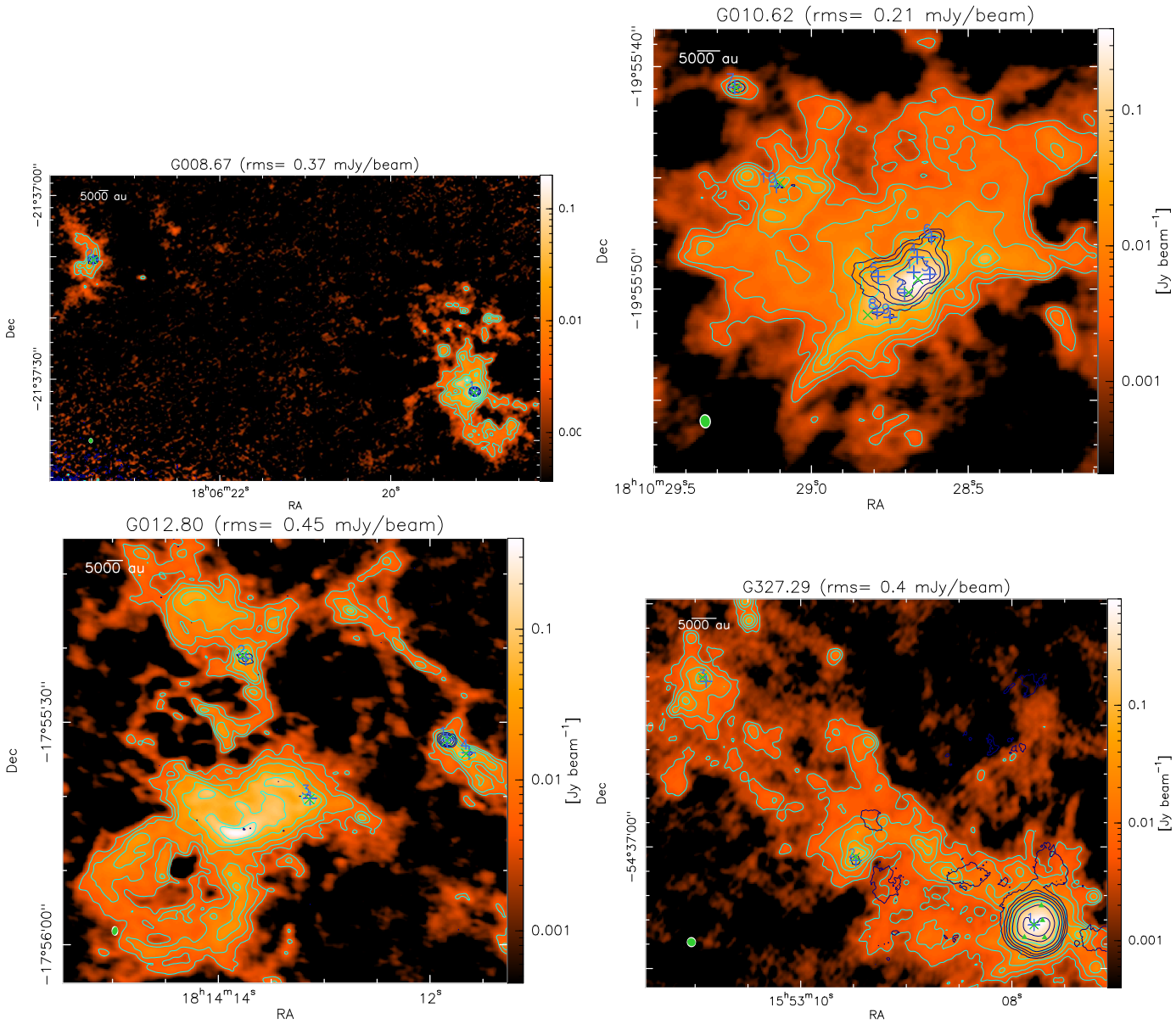

Fig. B.1: Continuum emission maps obtained at 1.3 mm toward the ALMA-IMF protoclusters (background image). The contours, shown in light blue, start at 5 σ and double in value thereafter. The 1 σ rms noise level measured in each continuum map is indicated on top of each panel. The dark blue contours show the methyl formate integrated emission as in Fig. 3. The blue crosses show the peak positions of the methyl formate sources extracted with GExt2D, while the green crosses show their associated continuum cores from the getsf-unsmoothed catalog (Paper XII). The green triangles show the continuum cores that coincide with extended methyl formate emission but are not associated with hot core candidates and as such are not shown in the lower panel of Fig. 13. The green and white ellipses represent the synthesized beam sizes of the continuum maps and the line cubes, respectively. The figure continues on the next page.

In Figs. B.1–B.4 we present the 1.3 mm ALMA-IMF continuum emission maps obtained toward the 15 protoclusters, compared to the contours of the methyl formate integrated emission.

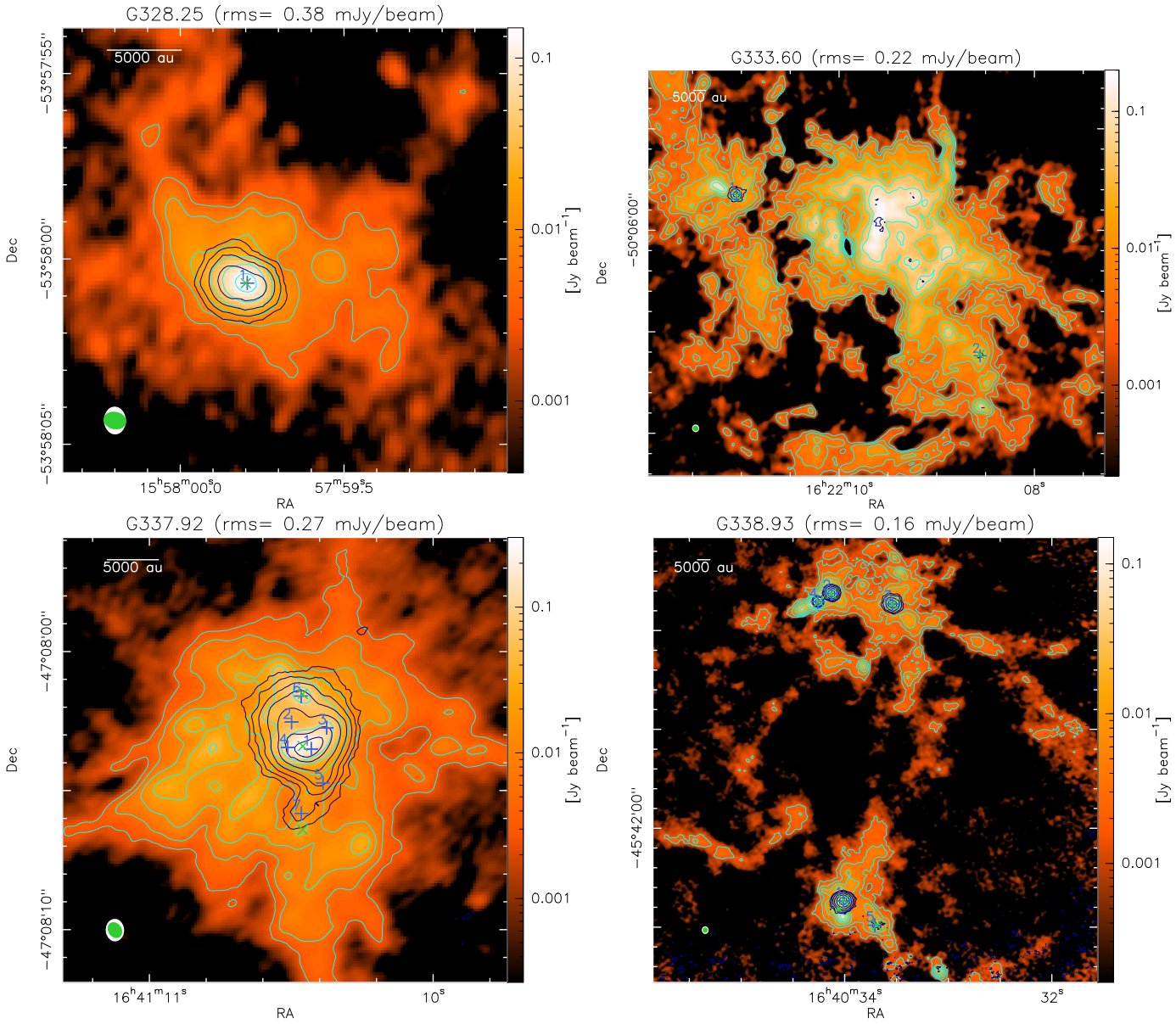

Fig. B.2: Continued.

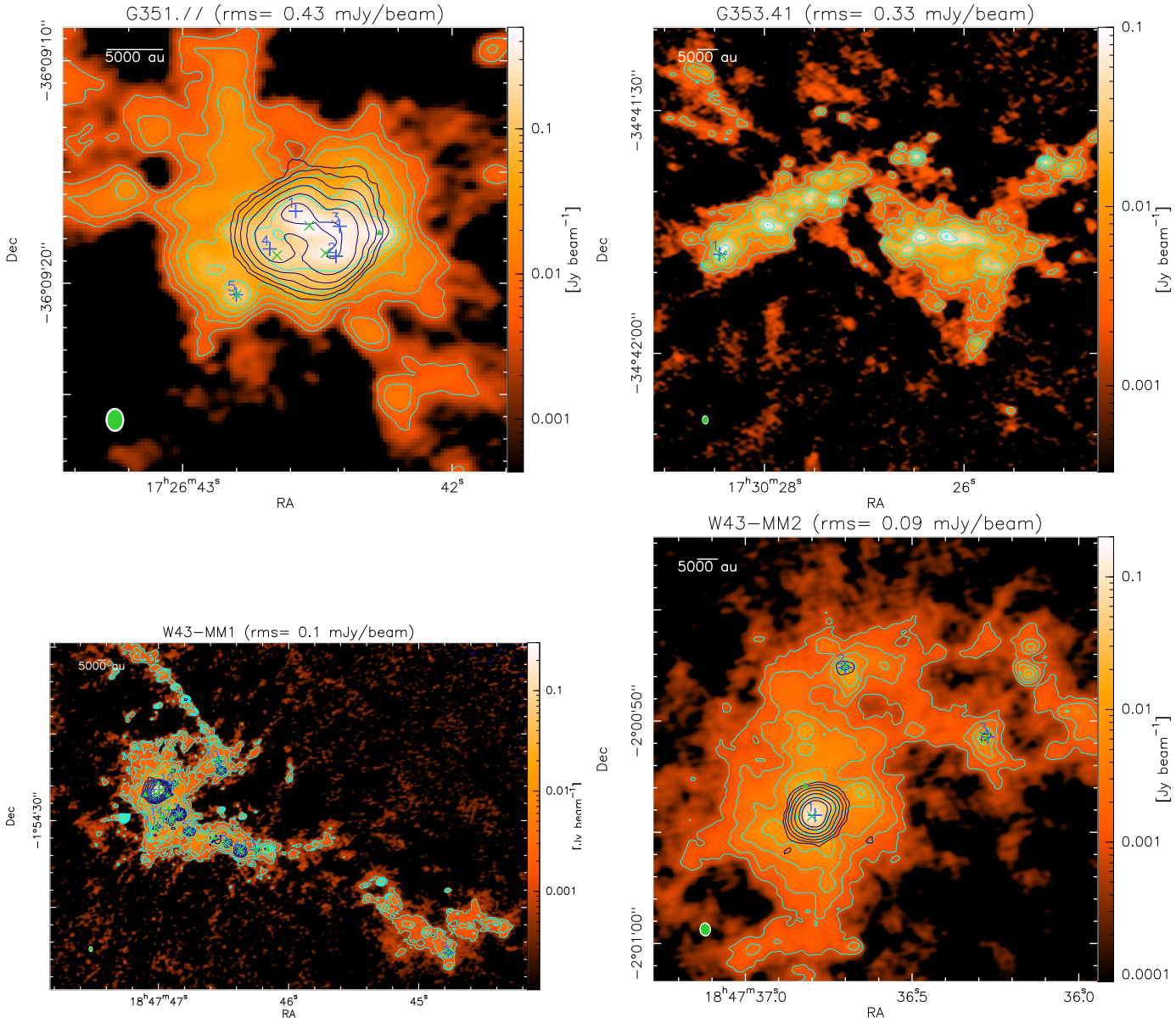

Fig. B.3: Continued.

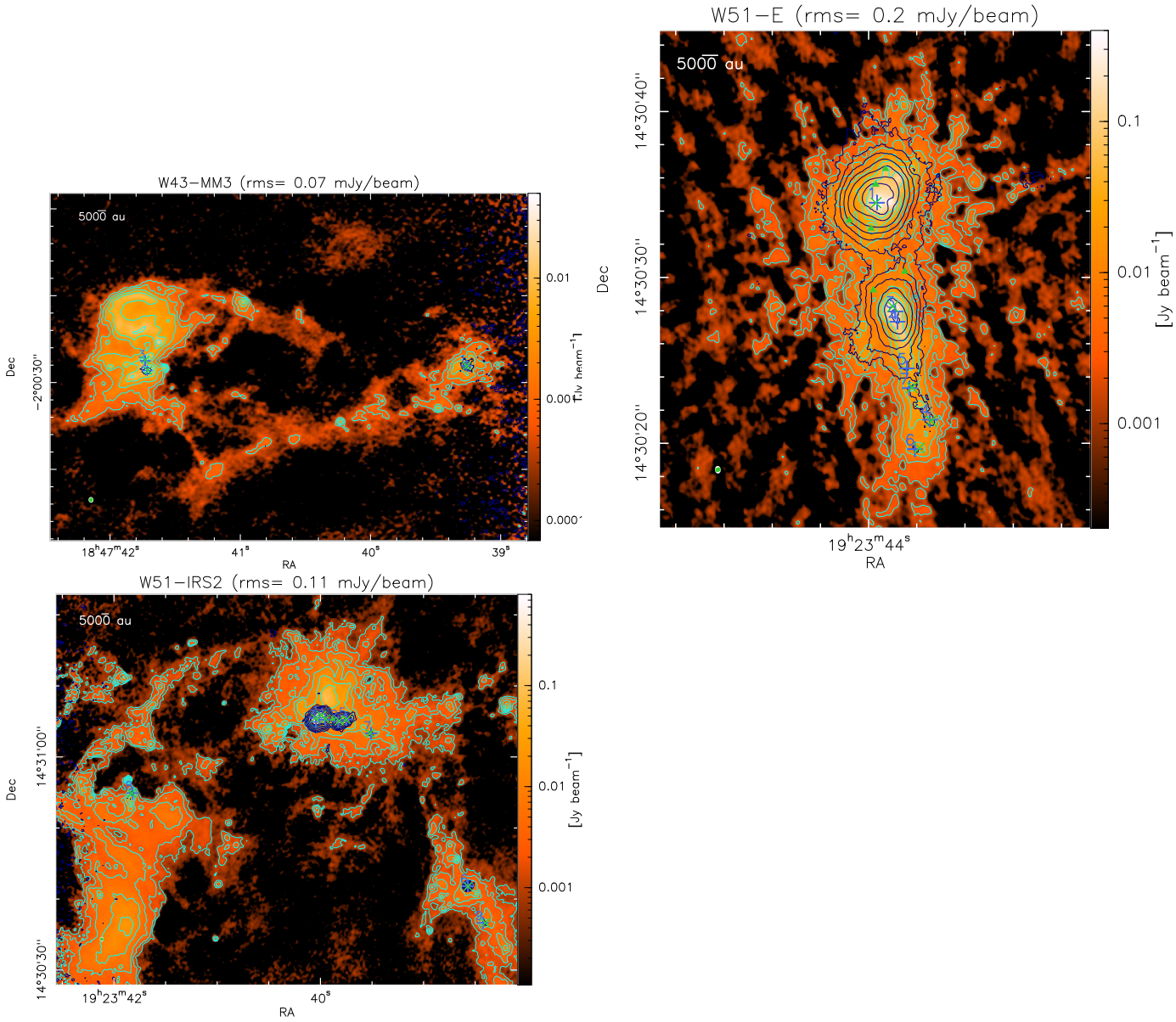

Fig. B.4: Continued.

Appendix C: Catalog of continuum cores associated with methyl formate emission and their properties

Table C.1: Properties of the continuum cores associated with the methyl formate sources toward the 15 ALMA-IMF protoclusters.

				1.3 mm					3 mm					
$ID_{MF}^{(a)}$	$RA^{(b)}$	$Dec^{(b)}$	$d^{(c)}$	$S^{peak}_{1.3mm^{(d)}}$	$S^{int}_{1.3mm^{(d)}}$	$\theta^{dec}_{maj} \times \theta^{dec^{(e)}}_{min}$	$PA^{dec^{(e)}}$	$FWHM^{dec^{(f)}}_{cont}$	$S^{int}_{3mm^{(g)}}$	$\tau^{(h)}$	Mass range$^{(i)}$	$M^{(j)}$	$\alpha^{(k)}$	$frac^{(l)}_{ff}$
	[J2000]		[″]	[mJy beam^{-1}]	[mJy]	[″ × ″]	[deg]	[au]	[mJy]		[$M_\odot$]	[$M_\odot$]		[%]
G008.67														
G008–MF1	18:06:19.02	-21:37:32.2	0.19	200.4±7.6	736.7±12.2	1.16×1.0	0.4	3675.4	557.0±1.4	0.04	21.7–5.9	9.4	0.3	65
G008–MF2	18:06:23.48	-21:37:10.5	0.02	64.4±1.5	84.5±1.4	0.37×0.31	-38.1	1166.2	9.1±0.2	0.04	6.7–2.0	3.1	2.7	0
G010.62														
G010–MF1	18:10:28.66	-19:55:49.6	0.36	316.6±13.6	1537.0±23.8	1.18×0.77	-58.7	4727.2	2448.8±14.2	_	_	_	-0.5	100
G010–MF2	18:10:28.69	-19:55:50.2	0.17	68.2±19.6	129.5±16.0	0.55×0.52	67.1	2658.1	185.8±7.1	_	_	_	-0.4	100
G010–MF3*	_	_	_	281.3±40.1	281.3±40.1	_	_	2306.7	232.6±47.2	0.09	15.4–3.9	6.2	0.2	72
G010–MF4*	_	_	_	50.7±19.2	50.7±19.2	_	_	2306.7	43.0±17.0	0.01	2.3–0.6	1.0	0.2	74
G010–MF5*	_	_	_	50.2±9.2	50.2±9.2	_	_	2306.7	44.4±11.7	0.01	2.0–0.5	0.8	0.1	77
G010–MF6*	_	_	_	24.3±11.4	24.3±11.4	_	_	2306.7	16.2±10.2	0.01	1.7–0.5	0.8	0.4	57
G010–MF7	18:10:29.24	-19:55:40.95	0.06	13.9±0.6	20.4±0.8	_	_	1153.3	3.0±0.2	0.02	3.3–1.0	1.5	2.3	0
G010–MF8	18:10:28.82	-19:55:51.17	0.42	22.9±7.0	45.0±6.3	0.6×0.44	86.6	2569.0	7.3±2.7	0.02	6.8–2.0	3.1	2.2	9
G010–MF9*	_	_	_	38.3±10.5	38.3±10.5	_	_	2306.7	16.1±7.7	0.03	4.3–1.2	1.9	1.0	34
G010–MF10	18:10:29.10	-19:55:45.23	0.21	18.3±3.2	19.6±2.5	_	_	1153.3	2.4±0.4	0.02	3.2–0.9	1.5	2.5	0
G012.80														
G012–MF1	18:14:11.84	-17:55:32.5	0.05	195.9±5.7	310.3±6.0	0.78×0.46	40.4	1442.3	16.0±0.3	0.07	12.7–3.7	5.8	3.6	0
G012–MF2	18:14:13.77	-17:55:21.0	0.59	107.6±4.9	229.9±5.7	1.07×0.72	22.2	2114.4	8.3±2.2	0.04	9.1–2.7	4.2	4.0	0
G012–MF3	18:14:13.14	-17:55:40.4	0.16	91.0±16.0	166.5±15.4	0.87×0.77	37.7	1980.0	10.3±4.7	0.03	6.5–1.9	3.0	3.3	0
G012–MF4	18:14:11.66	-17:55:34.2	0.40	61.0±6.2	159.3±7.0	1.72×0.94	-86.5	3069.6	11.5±0.6	0.02	6.2–1.9	2.9	3.2	0
G327.29														
G327–MF1	15:53:07.79	-54:37:06.4	0.01	669.3±4.8	3160.0±12.4	1.43×0.84	54.6	2755.0	171.5±1.4	0.13	33.1–15.5	21.1	3.5	0
G327–MF2	15:53:09.48	-54:37:00.8	0.28	79.3±4.0	311.2±6.0	1.46×1.00	-30.2	3040.0	33.1±0.4	0.05	13.5–4.0	6.2	2.7	0
G327–MF3	15:53:10.93	-54:36:46.1	0.44	37.6±2.8	106.3±3.6	0.94×0.89	-89.0	2307.5	10.4±0.3	0.02	4.5–1.3	2.1	2.8	0
G328.25														
G328–MF1	15:57:59.80	-53:58:00.7	0.04	147.7±1.6	406.1±2.6	0.83×0.44	71.3	1522.5	27.7±0.2	0.14	19.8–5.5	8.6	3.3	0
G333.60														
G333–MF1	16:22:11.05	-50:05:56.6	0.10	56.6±3.8	78.1±4.0	_	_	1163.4	8.6±0.1	0.04	9.1–2.7	4.2	2.6	4
G333–MF2	16:22:08.56	-50:06:12.2	0.14	25.0±3.3	87.6±4.2	1.07×0.83	36.6	3990.0	13.1±2.1	0.02	9.6–2.9	4.4	2.3	8

Notes. [(a)] ID of the methyl formate sources. [(b)] Position of the associated compact continuum core from the getsf-unsmoothed catalog presented in (XII). The sources marked with a * in the first column are not associated with any compact continuum core. [(c)] Angular offset between the peak position of the methyl formate source and its associated compact continuum core. [(d)] Peak and integrated intensities at 1.3 mm from the unsmoothed core catalog (XII). For the sources that are not associated with compact continuum cores, peak intensities have been measured in the 1.3 mm continuum maps (see Sect. 5.1). [(e)] Major × minor axis and position angle of the compact continuum core from the unsmoothed core catalog (XII). These values are deconvolved from the continuum map beam size. [(f)] Deconvolved mean size (FWHM) of the continuum cores. [(g)] 3 mm integrated intensity from the unsmoothed core catalog (XII). [(h)] Opacity computed at T_d = 100 K (except for the six most extreme sources for which we used 300 K; see Sect.5.4). [(i)] Core mass range computed with T_d ranging from 50 K to 150 K (except for the six most extreme sources for which we used 200 – 400 K; see Sect.5.4). [(j)] Core mass used to plot Figs. 13, 16 and 18, computed at T_d = 100 K for all methyl formate sources, except for the six most extreme sources for which we used 300 K (see Sect.5.4)). [(k)] Spectral index (see Sect. 5.2). [(l)] Fraction of the fluxes measured at 1.3 mm that is due to free-free emission and that are subtracted to the fluxes given in [(d)] to obtain the mass estimates given in [(i)] and [(j)]. The table continues on the next page.

Table C.1: Continued.

				1.3 mm					3 mm					
$ID_{MF}^{(a)}$	$RA^{(b)}$	$Dec^{(b)}$	$d^{(c)}$	$S^{peak}_{1.3mm^{(d)}}$	$S^{int}_{1.3mm^{(d)}}$	$\theta^{dec}_{maj} \times \theta^{dec^{(e)}}_{min}$	$PA^{dec^{(e)}}$	$FWHM^{dec^{(f)}}_{cont}$	$S^{int}_{3mm^{(g)}}$	$\tau^{(h)}$	Mass range$^{(i)}$	$M^{(j)}$	$\alpha^{(k)}$	$frac^{(l)}_{ff}$
	[J2000]		[″]	[mJy beam^{-1}]	[mJy]	[″ × ″]	[deg]	[au]	[mJy]		[$M_\odot$]	[$M_\odot$]		[%]
G337.92														
G337–MF1	16:41:10.46	-47:08:03.4	0.32	234.3±13.6	549.1±17.5	0.91×0.42	-83.4	1682.1	86.5±2.5	0.22	35.0–8.9	14.2	2.2	0
G337–MF2*	_	_	_	110.0±110.0	110.0±110.0	_	_	1460.7	8.6±8.6	0.1	6.0–1.7	2.6	3.1	0
G337–MF3*	_	_	_	240.0±65.0	240.0±65.0	_	_	1460.7	15.8±5.0	0.23	15.4–3.9	6.2	3.3	0
G337–MF4*	_	_	_	136.0±136.0	136.0±136.0	_	_	1460.7	5.6±5.6	0.12	7.6–2.1	3.3	3.9	0
G337–MF5*	_	_	_	18.4±18.4	18.4±18.4	_	_	1460.7	1.1±1.1	0.02	0.9–0.2	0.4	3.4	0
G337–MF6	16:41:10.46	-47:08:01.5	0.08	71.3±17.7	151.9±19.5	0.74×0.41	61.5	1503.9	21.9±1.8	0.06	7.9–2.3	3.6	2.4	0
G337–MF7	16:41:10.46	-47:08:06.4	0.58	13.6±3.5	16.3±2.7	_	_	731.7	2.0±0.1	0.01	0.8–0.2	0.3	2.6	0
G338.93														
G338–MF1	16:40:34.01	-45:42:07.3	0.06	103.2±1.8	148.6±1.8	0.39×0.32	67.4	1396.2	8.8±0.3	0.09	16.6–4.7	7.4	3.4	0
G338–MF2	16:40:34.13	-45:41:36.3	0.01	154.1±1.3	280.7±2.4	0.45×0.27	-86.4	1380.6	21.3±0.4	0.14	33.2-9.1	14.3	3.1	0
G338–MF3	16:40:33.54	-45:41:37.3	0.01	70.8±1.1	158.8±2.3	0.47×0.28	9.4	1450.8	13.2±0.3	0.06	17.1–5.0	7.8	3.0	0
G338–MF4	16:40:34.25	-45:41:37.1	0.10	141.5±1.3	237.4±1.4	0.53×0.25	-41.2	1443.0	31.9±0.3	0.13	27.7–7.7	12.0	2.4	0
G338–MF5	16:40:33.69	-45:42:09.8	0.22	26.9±1.4	65.0±2.0	0.67×0.49	57.7	2250.2	4.9±0.2	0.02	6.7–2.0	3.1	3.1	0
G351.77														
G351–MF1	17:26:42.53	-36:09:17.4	0.89	339.3±35.3	897.8±47.2	1.37×0.7	53.0	1972.0	35.0±1.2	0.15	28.6–7.8	12.2	3.9	0
G351–MF2	17:26:42.47	-36:09:18.7	0.49	271.7±31.9	1199.0±42.6	1.86×1.4	-66.5	3230.0	54.8±2.7	0.12	36.7–10.3	16.1	3.7	0
G351–MF3*	_	_	_	930.0±130.0	930.0±130.0	_	_	1544.0	68.4±10.0	0.49	52.1–8.9	14.9	3.1	0
G351–MF4	17:26:42.65	-36:09:18.8	0.43	94.3±34.8	254.0±35.9	1.31×0.81	35.6	2074.0	26.5±0.01	0.04	7.1–2.1	3.2	2.7	0
G351–MF5	17:26:42.80	-36:09:20.5	0.01	106.9±32.1	175.7±30.8	0.7×0.43	-16.1	1102.0	5.0±1.7	0.05	4.9–1.4	2.2	4.3	0
G353.41														
G353–MF1	17:30:28.43	-34:41:47.9	0.25	53.5±3.0	127.0±3.3	1.06×0.74	-5.1	1780.0	5.0±0.4	0.02	3.4–1.0	1.6	3.9	0
W43-MM1														
W43-MM1–MF1	18:47:46.98	-01:54:26.5	0.21	118.6±3.8	361.6±4.3	0.72×0.62	27.7	3685.0	23.8±0.4	0.18	89.0–23.6	37.3	3.2	0
W43-MM1–MF2	18:47:47.02	-01:54:26.9	0.20	311.6±3.9	640.9±5.0	0.45×0.39	42.2	2332.0	29.2±0.3	0.56	356.0–46.6	79.5	3.7	0
W43-MM1–MF3	18:47:46.84	-01:54:29.3	0.01	187.8±5.8	297.2±6.8	0.38×0.16	-1.2	1358.5	20.5±0.5	0.3	86.8–20.1	32.5	3.2	0
W43-MM1–MF4	18:47:46.37	-01:54:33.4	0.11	96.8±1.9	227.0±2.8	0.55×0.29	24.2	2205.5	17.4±0.2	0.15	53.5–14.7	23.0	3.0	0
W43-MM1–MF5	18:47:46.77	-01:54:31.2	0.07	45.5±3.1	72.5±3.1	0.4×0.25	51.5	1771.0	5.4±0.2	0.07	15.5–4.5	7.0	3.1	0
W43-MM1–MF6	18:47:46.52	-01:54:24.2	0.01	15.8±1.4	21.1±1.3	0.31×0.20	89.2	1413.5	1.4±0.1	0.02	4.3–1.3	2.0	3.2	0
W43-MM1–MF7	18:47:46.90	-01:54:30.0	0.09	26.3±5.0	33.2±3.9	0.26×0.25	31.0	1424.5	1.9±0.3	0.04	6.9–2.0	3.2	3.4	0
W43-MM1–MF8	18:47:46.48	-01:54:32.6	0.12	30.4±3.4	46.2±3.2	0.33×0.26	45.5	1644.5	3.1±0.2	0.04	9.6–2.9	4.4	3.2	0
W43-MM1–MF9	18:47:44.77	-01:54:45.2	0.04	12.2±0.9	20.7±0.9	0.37×0.34	1.8	1980.0	0.9±0.1	0.02	4.2–1.2	1.9	3.7	0
W43-MM1–MF10	18:47:46.54	-01:54:23.1	0.06	43.0±1.0	74.9±1.3	0.41×0.26	-84.0	1826.0	5.9±0.1	0.06	16.0–4.7	7.3	3.0	0
W43-MM1–MF11	18:47:47.02	-01:54:30.8	0.22	20.1±5.0	41.6±4.9	0.61×0.32	-19.7	2447.5	2.9±0.3	0.03	8.5–2.6	3.9	3.1	0
W43-MM1–MF12	18:47:46.87	-01:54:25.7	0.20	14.5±3.5	17.5±2.9	_	_	1149.5	1.3±0.2	0.02	3.5–1.0	1.6	3.1	0
W43-MM1–MF13	18:47:46.25	-01:54:33.4	0.05	17.2±1.6	25.9±1.3	0.46×0.26	-22.4	1936.0	2.5±0.1	0.02	5.3–1.6	2.4	2.8	0
W43-MM1–MF14	18:47:46.97	-01:54:29.7	0.11	18.2±5.3	18.8±4.1	_	_	1149.5	2.0±0.3	0.03	3.8–1.1	1.8	2.6	0
W43-MM2														
W43-MM2–MF1	18:47:36.80	-02:00:54.3	0.14	144.2±1.1	432.7±3.2	0.61×0.43	-15.0	2832.5	30.3±0.3	0.18	108.8–28.8	45.5	3.2	0
W43-MM2–MF2	18:47:36.70	-02:00:47.6	0.04	14.8±0.7	28.2±0.9	0.45×0.3	-49.3	2029.5	2.3±0.1	0.02	5.8–1.7	2.7	3.0	0
W43-MM2–MF3	18:47:36.28	-02:00:50.8	0.11	10.7±0.4	19.8±0.5	_	_	1270.5	2.1±0.2	0.01	4.0–1.2	1.9	2.7	0

Notes. The table continues on the next page.

Table C.1: Continued.

				1.3 mm					3 mm					
$ID_{MF}^{(a)}$	$RA^{(b)}$	$Dec^{(b)}$	$d^{(c)}$	$S^{peak}_{1.3mm^{(d)}}$	$S^{int}_{1.3mm^{(d)}}$	$\theta^{dec}_{maj} \times \theta^{dec^{(e)}}_{min}$	$PA^{dec^{(e)}}$	$FWHM^{dec^{(f)}}_{cont}$	$S^{int}_{3mm^{(g)}}$	$\tau^{(h)}$	Mass range$^{(i)}$	$M^{(j)}$	$\alpha^{(k)}$	$frac^{(l)}_{ff}$
	[J2000]		[″]	[mJy beam^{-1}]	[mJy]	[″ × ″]	[deg]	[au]	[mJy]		[$M_\odot$]	[$M_\odot$]		[%]
W43-MM3														
W43-MM3–MF1	18:47:39.26	-02:00:28.1	0.06	16.8±0.4	36.6±0.6	0.51×0.33	50.3	2277.0	1.3±0.01	0.02	7.5–2.2	3.5	4.0	0
W43-MM3–MF2	18:47:41.71	-02:00:28.6	0.07	51.1±2.0	78.3±2.5	0.38×0.21	-88.0	1589.4	6.6±0.4	0.06	16.7–4.9	7.6	3.0	0
W43-MM3–MF3	18:47:41.73	-02:00:27.4	0.10	22.5±1.7	25.8±1.5	_	_	1303.5	1.9±0.1	0.03	5.3–1.6	2.4	3.1	0
W51-E														
W51-E–MF1	19:23:43.97	14:30:34.5	0.06	363.0±8.8	2004.0±19.0	0.68×0.51	-0.2	3218.3	358.7±7.5	0.32	102.5–43.6	61.0	2.1	11
W51-E–MF2*	_	_	_	245.6±32.6	245.6±32.6	_	_	1636.2	48.3±9.3	0.24	13.2–5.8	8.1	2.0	0
W51-E–MF3	19:23:43.90	14:30:28.2	0.33	250.8±17.8	853.7±25.1	0.49×0.46	-1.2	2597.4	215.8±5.2	0.19	36.0–16.3	22.4	1.6	18
W51-E–MF4	19:23:43.74	14:30:21.3	0.11	17.9±4.9	30.0±4.4	0.32×0.24	81.2	1528.1	4.7±0.6	0.05	6.1–1.8	2.8	2.2	0
W51-E–MF5*	_	_	_	55.5±9.2	55.5±9.2	_	_	1636.2	16.8±1.4	0.12	9.6–2.6	4.1	1.4	22
W51-E–MF6	19:23:43.79	14:30:19.7	0.27	13.9±3.3	30.6±3.5	0.39×0.29	57.1	1836.0	10.5±0.9	0.04	6.1–1.8	2.8	1.3	0
W51-E–MF7	19:23:43.82	14:30:23.4	0.15	17.7±6.3	44.4±6.9	0.43×0.36	4.8	2165.4	10.3±1.0	0.05	9.0–2.7	4.1	1.7	0
W51-IRS2														
W51-IRS2–MF1	19:23:39.99	14:31:05.9	0.43	252.7±13.4	506.4±12.4	0.55×0.52	60.6	2910.6	49.7±6.4	0.09	23.3–11.1	15.0	2.8	3
W51-IRS2–MF2	19:23:39.82	14:31:05.1	0.18	223.5±14.9	393.5±13.0	0.56×0.39	46.4	2554.2	104.0±2.7	0.22	81.2–20.8	32.5	1.6	19
W51-IRS2–MF3	19:23:40.05	14:31:05.5	0.53	847.2±15.2	1789.0±20.7	0.52×0.39	75.1	2457.0	368.0±12.6	0.3	87.1–37.6	52.4	1.9	14
W51-IRS2–MF4	19:23:39.95	14:31:05.4	0.14	333.2±13.7	488.3±11.9	0.39×0.27	85.6	1771.2	128.4±7.0	0.35	123.0–26.3	43.0	1.6	19
W51-IRS2–MF5	19:23:39.75	14:31:05.3	0.04	141.1±14.3	196.0±11.1	0.46×0.25	63.5	1857.6	17.3±2.8	0.16	44.8–12.0	19.0	2.9	2
W51-IRS2–MF6	19:23:38.57	14:30:41.8	0.01	68.2±1.0	197.3±2.6	0.49×0.36	-32.4	2284.2	21.7±0.6	0.08	41.8–12.1	18.8	2.7	0
W51-IRS2–MF7	19:23:39.52	14:31:03.4	0.17	17.7±2.5	29.9±2.9	0.43×0.14	67.7	1360.8	1.1±1.7	0.02	5.9–1.8	2.7	4.0	0
W51-IRS2–MF8	19:23:41.83	14:30:54.9	0.17	12.2±1.1	15.9±0.9	0.39×0.17	9.8	1409.4	4.2±0.4	0.01	3.1–0.9	1.4	1.6	0
W51-IRS2–MF9	19:23:38.40	14:30:36.7	0.36	11.5±1.1	35.7±1.5	0.80×0.52	49.9	3515.4	2.5±0.1	0.01	7.0–2.1	3.3	3.2	0

Appendix D: Correction for the free-free contribution

As mentioned already in Sect. 5.2, the ALMA-IMF dataset covers the $H_{41\alpha}$ recombination line at 92.0 GHz that we use here to trace ionized gas coming from HII regions. Figures D.1–D.4 show the regions that are expected to be contaminated by free-free emission based on the emission contours of $H_{41\alpha}$ (see the pink contours). We identify 17 methyl formate sources, in G008.67, G010.62, G012.80, G333.60, W51-E, and W51-IRS2, that lie in regions containing free-free emission. In order to estimate the contribution of free-free emission to the 1.3 mm flux densities measured for these 17 cores, we proceeded as follows.

First the 3 mm integrated fluxes were rescaled to the 1.3 mm sizes to allow a direct comparison of these fluxes, as described in Paper III. Then we computed the theoretical flux ratio expected for thermal dust emission ($\gamma_{\rm th}^{\rm dust}$) under the optically thin assumption and considering that the fluxes arise from the same area:

$$\gamma_{\rm th}^{\rm dust} = \frac{S^{\rm int}_{\rm 1.3mm}}{S^{\rm int}_{\rm 3mm}} \tag{D.1}$$

$$= \frac{\kappa_{\rm 1.3mm}}{\kappa_{\rm 3mm}} \frac{B_{\rm 1.3mm}(T_{\rm d})}{B_{\rm 3mm}(T_{\rm d})} = \frac{\kappa_{\rm 1.3mm}}{\kappa_{\rm 3mm}} \times \left(\frac{\nu_{3mm}}{\nu_{1.3mm}}\right)^3 \frac{e^{h\nu_{\rm 3mm}/k_{\rm b}T_{\rm d}} - 1}{e^{h\nu_{\rm 1.3mm}/k_{\rm b}T_{\rm d}} - 1}, \tag{D.2}$$

where $B_{\rm 1.3mm}(T_{\rm d})$ and $B_{\rm 3mm}(T_{\rm d})$ are the Planck function for the dust temperature T_d at 1.3 mm and 3 mm, respectively, k_b is the Boltzmann constant, h is the Planck constant, $\nu_{\rm 1.3mm}$ and $\nu_{\rm 3mm}$ the central frequencies of the continuum maps at 1.3 mm and 3 mm, respectively (see Table 2). Following Paper III, we adopted a dust opacity per unit of mass (gas + dust) $\kappa_{\rm 1.3mm}$ = 0.01 cm g^{-1}. The dust mass opacity at 3 mm, $\kappa_{\rm 3mm}$ was computed as follows:

$$\kappa_{\rm 3mm} = \kappa_{\rm 1.3mm} \times \left(\frac{\nu_{3mm}}{\nu_{1.3mm}}\right)^{\beta}, \tag{D.3}$$

where $\beta = \alpha$ - 2 (Terebey et al. 1993). Following Paper III, we assume $\alpha_{\rm dust}$ = 3.5, which corresponds to $\beta_{\rm dust}$ = 1.5, suitable for optically thin dense gas at the core scale (Ossenkopf & Henning 1994). Then by combining Eqs. D.3 and D.1, we obtain

$$\gamma_{\rm th}^{\rm dust} = \left(\frac{\nu_{\rm 1.3mm}}{\nu_{\rm 3mm}}\right)^{\alpha_{\rm dust}+1} \times \frac{e^{h\nu_{\rm 3mm}/k_{\rm b}T_{\rm d}} - 1}{e^{h\nu_{\rm 1.3mm}/k_{\rm b}T_{\rm d}} - 1}, \tag{D.4}$$

where $\gamma_{\rm th}^{\rm dust}$ = 16.62 – 17.34, for $T_{\rm d}$ = 50 – 150K. This is valid if the integrated flux measured at 1.3 mm ($S^{\rm int}_{\rm 1.3mm}$) and 3 mm ($S^{\rm int}_{\rm 3mm}$) are only due to thermal dust emission. However, at 3 mm we expect that a non-negligible fraction of the measured flux is due to free-free emission, such that

$$S^{\rm int}_{\rm 3mm} = S^{\rm int-corr}_{\rm 3mm} - S^{\rm int-freefree}_{\rm 3mm}, \tag{D.5}$$

where $S^{\rm int-corr}_{\rm 3mm}$ is the 3 mm integrated flux corrected from the free-free contribution, and $S^{\rm int-freefree}_{\rm 3mm}$ the flux due to free-free emission, such that

$$\gamma_{\rm th}^{\rm freefree} = \frac{S^{\rm int-freefree}_{\rm 1.3mm}}{S^{\rm int-freefree}_{\rm 3mm}}, \tag{D.6}$$

with $\gamma_{\rm th}^{\rm freefree}$ = 0.86 – 0.90, for $T_{\rm d}$ = 50 – 150 K, and for a spectral index $\alpha_{\rm freefree}$ = -0.1 that corresponds to optically thin free-free emission (see, e.g., Keto et al. 2008).

In order to estimate integrated fluxes corrected from the free-free contribution, we assume in first approximation that the flux measured at 1.3 mm is optically thin and is only due to dust thermal emission, such that

$$S^{\rm int-corr}_{\rm 3mm} = \frac{S^{\rm int}_{\rm 1.3mm}}{\gamma_{\rm th}^{\rm dust}}. \tag{D.7}$$

However, for the sources contaminated by free-free emission, we expect $S^{\rm int-corr}_{\rm 1.3mm} \neq S^{\rm int}_{\rm 1.3mm}$, which implies that the integrated flux measured at 1.3 mm is not fully due to dust thermal emission like assumed above. From Eqs. D.5, D.6, and D.7, we derive the 1.3 mm flux corrected for the free-free contribution:

$$S^{\rm int-corr}_{\rm 1.3mm} = S^{\rm int}_{\rm 1.3mm} - \gamma_{\rm th}^{\rm freefree}(S^{\rm int}_{\rm 3mm} - S^{\rm int-corr}_{\rm 3mm}). \tag{D.8}$$

For more consistency, those calculations are performed in an iterative way, by replacing $S^{\rm int}_{\rm 1.3mm}$ in Eq. D.5 by its corrected value, $S^{\rm int-corr}_{\rm 1.3mm}$. Then Eqs. D.7 and D.8 are computed until the calculations converge onto a final value for $S^{\rm int-corr}_{\rm 1.3mm}$. The resulting values are given in the last column of Table C as a correction factor, frac$_{ff}$, that indicates the fraction of the flux initially measured that is due to free-free emission for each continuum core. This correction factor must be applied to both the peak and integrated flux measured at 1.3 mm for the 17 methyl formate sources that are contaminated by free-free emission.

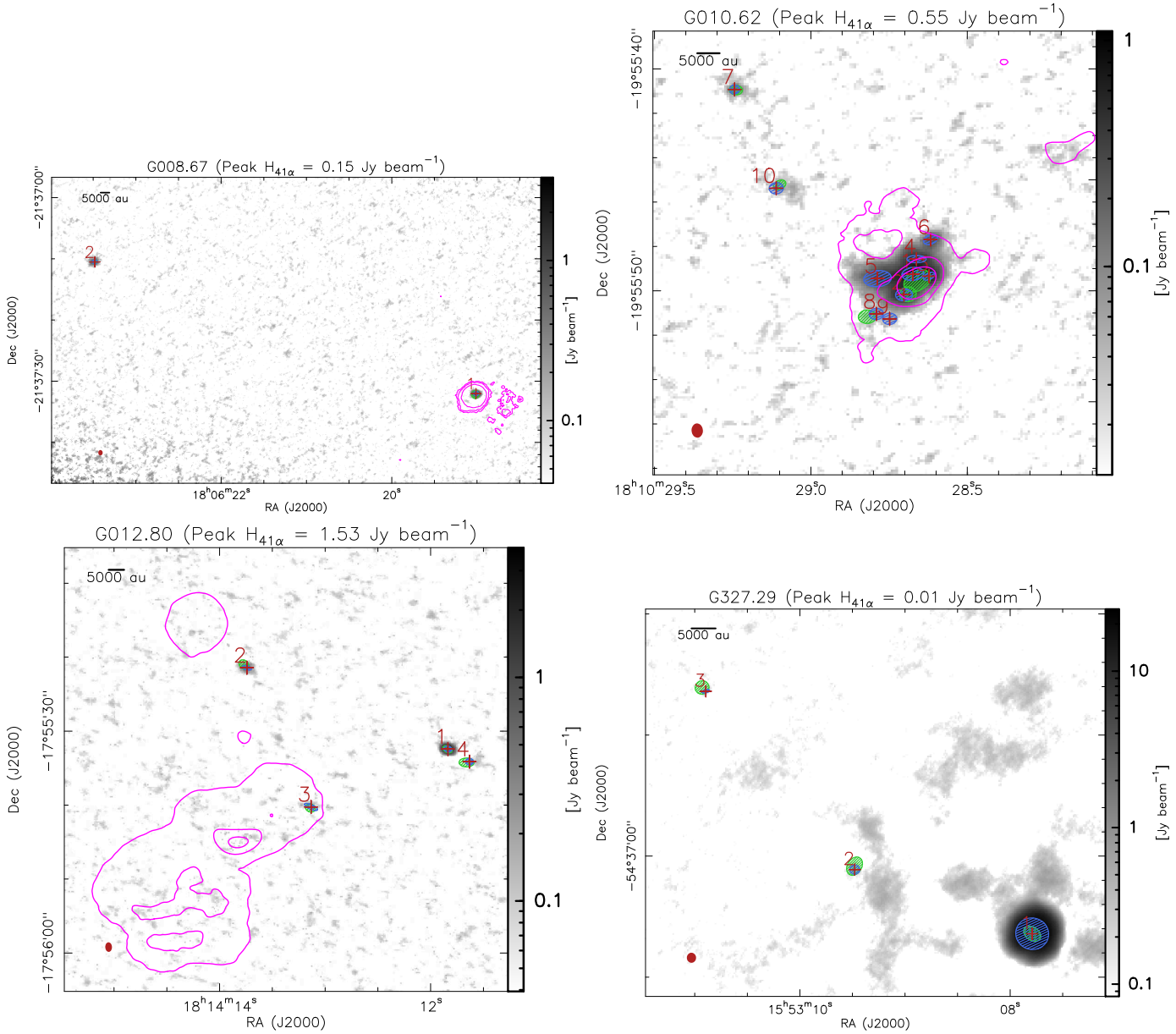

Fig. D.1: Methyl formate moment 0 maps (background image) as shown in Fig. 3. The red crosses indicate the peak positions of the methyl formate sources, while the blue ellipses show the deconvolved emission sizes. The green ellipses show the deconvolved source sizes of the associated compact continuum cores. The synthesized beam size on the ALMA-IMF B6-SPW0 line cubes are shown with a red ellipse in the bottom left corner of each panel. Contours of the $H_{41\alpha}$ emission are overlaid in magenta on top of the moment 0 maps of methyl formate, showing 2, 20, and 50% of the peak intensity, indicated on top of each panel. The figure continues on the next page.

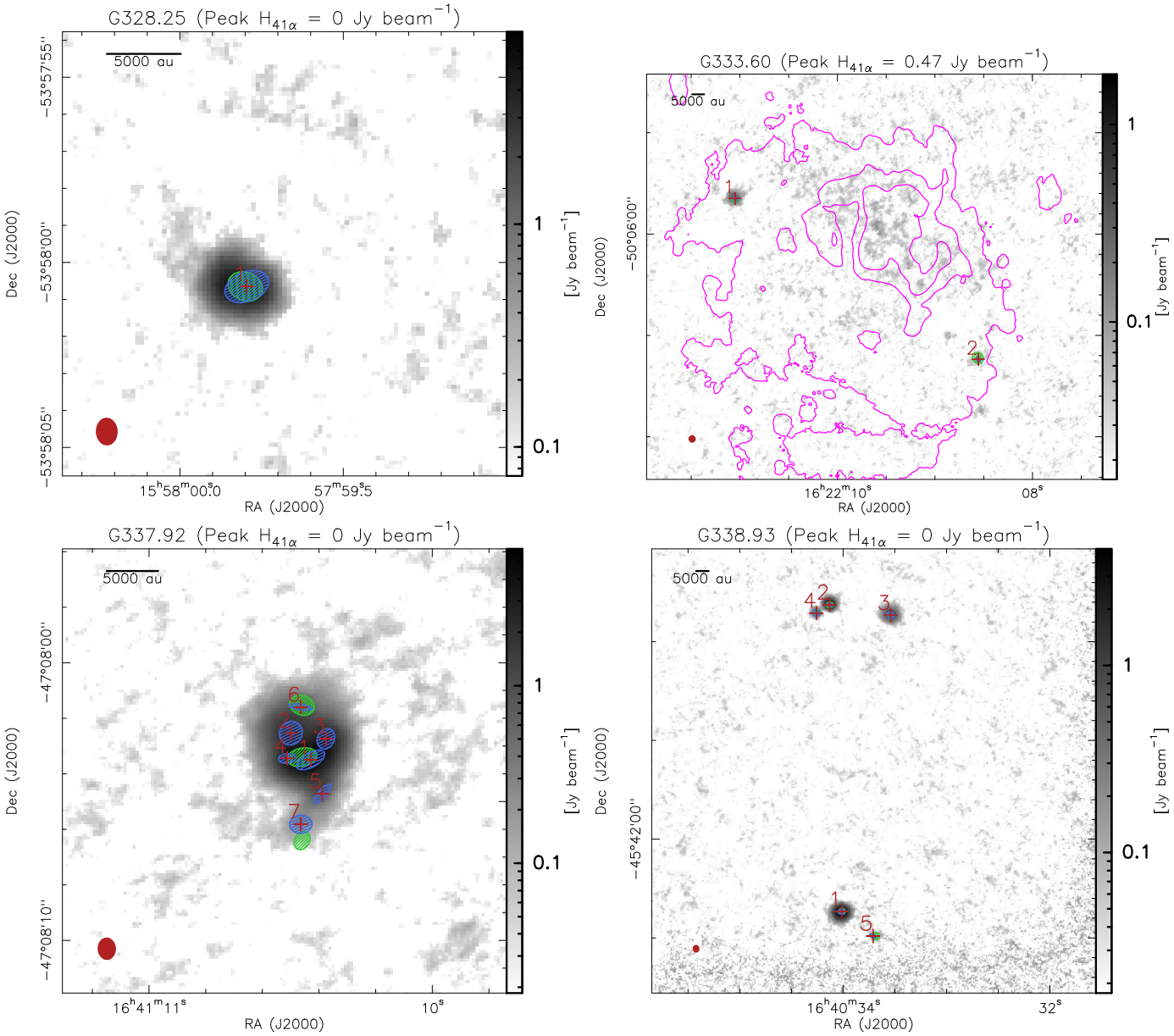

Fig. D.2: Continued.

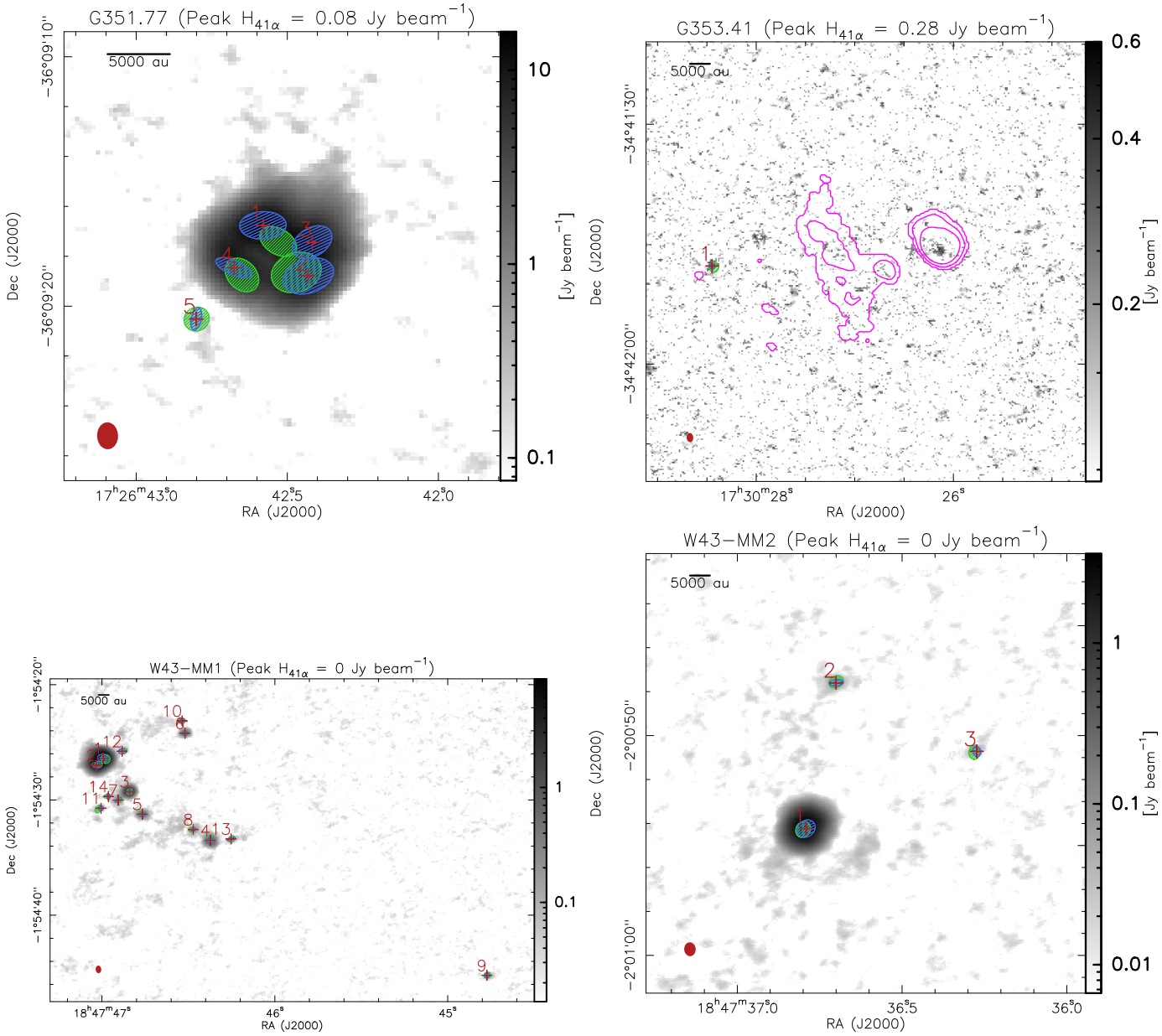

Fig. D.3: Continued.

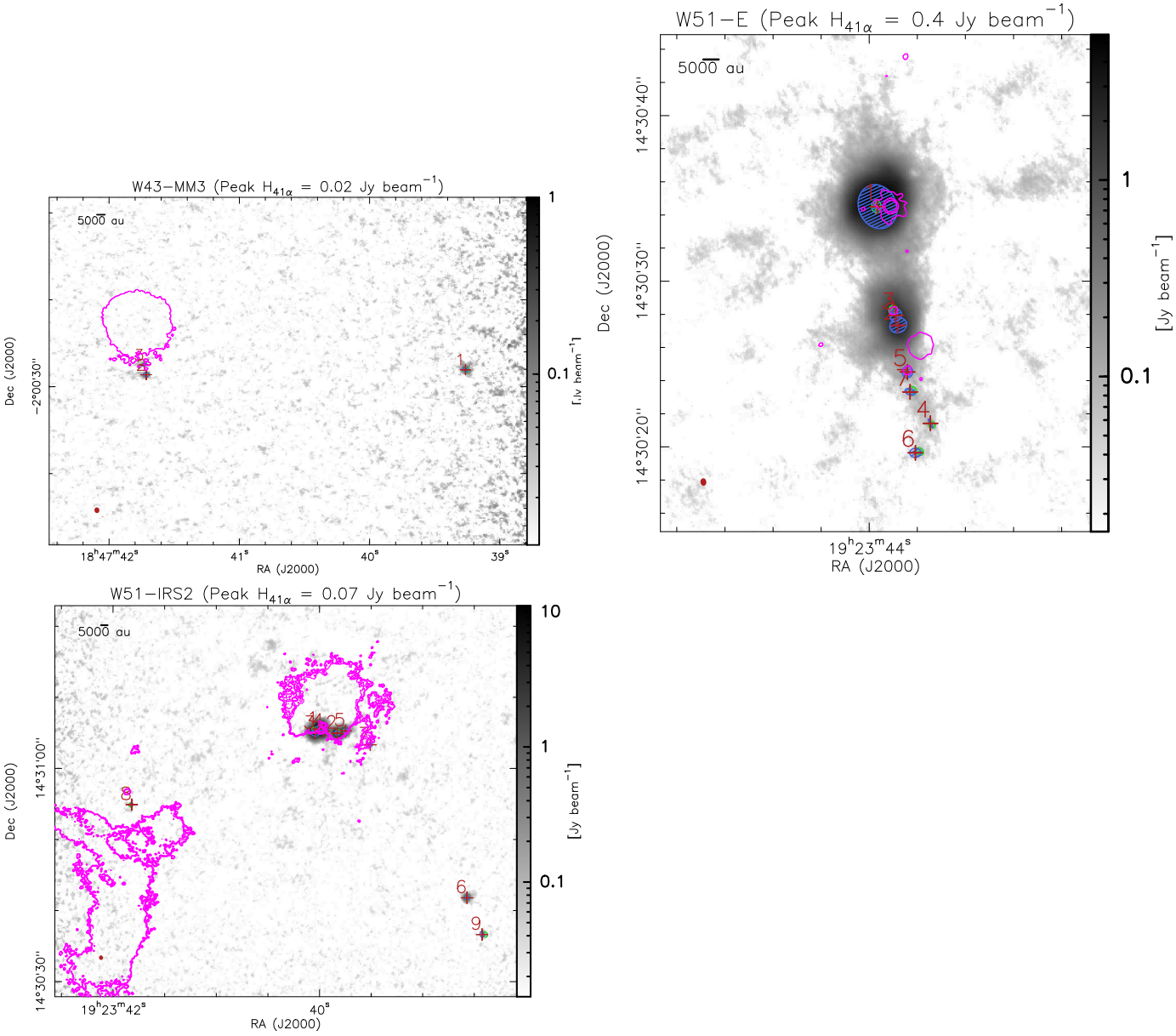

Fig. D.4: Continued.

Appendix E: Source size deconvolution

The source sizes derived for the 76 hot core candidates are presented in Sect. 5.3. They were obtained by fitting 2D Gaussians to the methyl formate moment 0 maps of the 15 ALMA-IMF protoclusters (Sect. 3.2), using the source extraction algorithm GExt2D. In order to to retrieve the actual source sizes, we deconvolve the source sizes inferred from the Gaussian fits, from the beam size of the line cubes as follows (Pety, priv. comm.). First we defined

$$a = [\theta_{\rm maj} \times cos(\phi_{\rm s})]^2 + [\theta_{\rm min} \times sin(\phi_{\rm s})]^2 - [\theta_{\rm maj}^{\rm beam} \times cos(\phi_{\rm beam})]^2 - [\theta_{\rm min}^{\rm beam} \times sin(\phi_{\rm beam})]^2 \,, \tag{E.1}$$

$$b = [\theta_{\rm maj} \times sin(\phi_{\rm s})]^2 + [\theta_{\rm min} \times cos(\phi_{\rm s})]^2 - [\theta_{\rm maj}^{\rm beam} \times sin(\phi_{\rm beam})]^2 - [\theta_{\rm min}^{\rm beam} \times cos(\phi_{\rm beam})]^2 \,, \tag{E.2}$$

$$c = 2 \times [(\theta_{\rm min}^2 - \theta_{\rm maj}^2) \times sin(\phi_{\rm s}) \times cos(\phi_{\rm s}) - (\theta_{\rm min}^{\rm beam\ 2} - \theta_{\rm min}^{\rm beam\ 2}) \times sin(\phi_{\rm beam}) \times cos(\phi_{\rm beam})] \,, \tag{E.3}$$

where

$$\phi_{\rm s} = {\rm PA} \times \frac{\pi}{180} \tag{E.4}$$

and

$$\phi_{\rm beam} = {\rm PA}_{\rm beam} \times \frac{\pi}{180} \tag{E.5}$$

are expressed in radians. The major ($\theta_{\rm maj}$) and minor ($\theta_{\rm min}$) axes of the measured source size (FWHM$_{\rm MF}$), as well as the major ($\theta_{\rm maj}^{\rm beam}$) and minor ($\theta_{\rm min}^{\rm beam}$) axes of the synthesized beam size of the line cubes, are expressed in arcseconds. The beam parameters ($\theta_{\rm min}^{\rm beam} \times \theta_{\rm maj}^{\rm beam}$, PA$_{\rm beam}$) are taken from Table 2, while the parameters for the methyl formate source sizes ($\theta_{\rm min} \times \theta_{\rm maj}$, PA) are taken from Table 4. We also defined

$$d = a + b, \tag{E.6}$$

and

$$e = \sqrt{(a-b)^2 + c^2}, \tag{E.7}$$

such that the deconvolved source sizes parameters ($\theta_{\rm min}^{\rm dec} \times \theta_{\rm maj}^{\rm dec}$, PA$_{\rm dec}$) are given by

$$\theta_{\rm maj}^{\rm dec} = \sqrt{\frac{|d+e|}{2}}, \tag{E.8}$$

$$\theta_{\rm min}^{\rm dec} = \sqrt{\frac{|d-e|}{2}}, \tag{E.9}$$

in arcseconds, and

$${\rm PA}^{\rm dec} = \frac{180}{\pi} \times \frac{atan2(-{\rm c}, {\rm a}-{\rm b})}{2}. \tag{E.10}$$

in degrees, which uses the two-argument arctangent (*atan2*) function of the GILDAS[5] software.

Finally, the deconvolved source size is given by

$$\theta_{\rm MF}^{\rm dec} = \sqrt{\theta_{\rm maj}^{\rm dec} \times \theta_{\rm min}^{\rm dec}}, \tag{E.11}$$

which may also be expressed in astronomical units, as the physical size of the source ($FWHM_{\rm MF}^{\rm dec}$) at the distance of the protocluster. As mentioned already in Sect. 5.3, we set a minimum deconvolved size for each region that is equal to half the FWHM of the synthesized beam of the line cube in order to limit deconvolution effects that may give excessively small and thus unrealistic sizes. The resulting methyl formate deconvolved source sizes are shown in Figs. D.1–D.4 together with the deconvolved continuum core sizes for the comparison.

Figure E.1 shows the deconvolved source sizes ($\theta_{\rm MF}^{\rm dec}$, Eq. E.11), plotted as a function of the source ellipticity (ϵ), which is given by

$$\epsilon = 1 - \frac{\theta_{\rm min}^{\rm dec}}{\theta_{\rm maj}^{\rm dec}}. \tag{E.12}$$

It shows that most methyl formate sources have an ellipticity $\epsilon < 0.5$.

[5] https://www.iram.fr/IRAMFR/GILDAS/

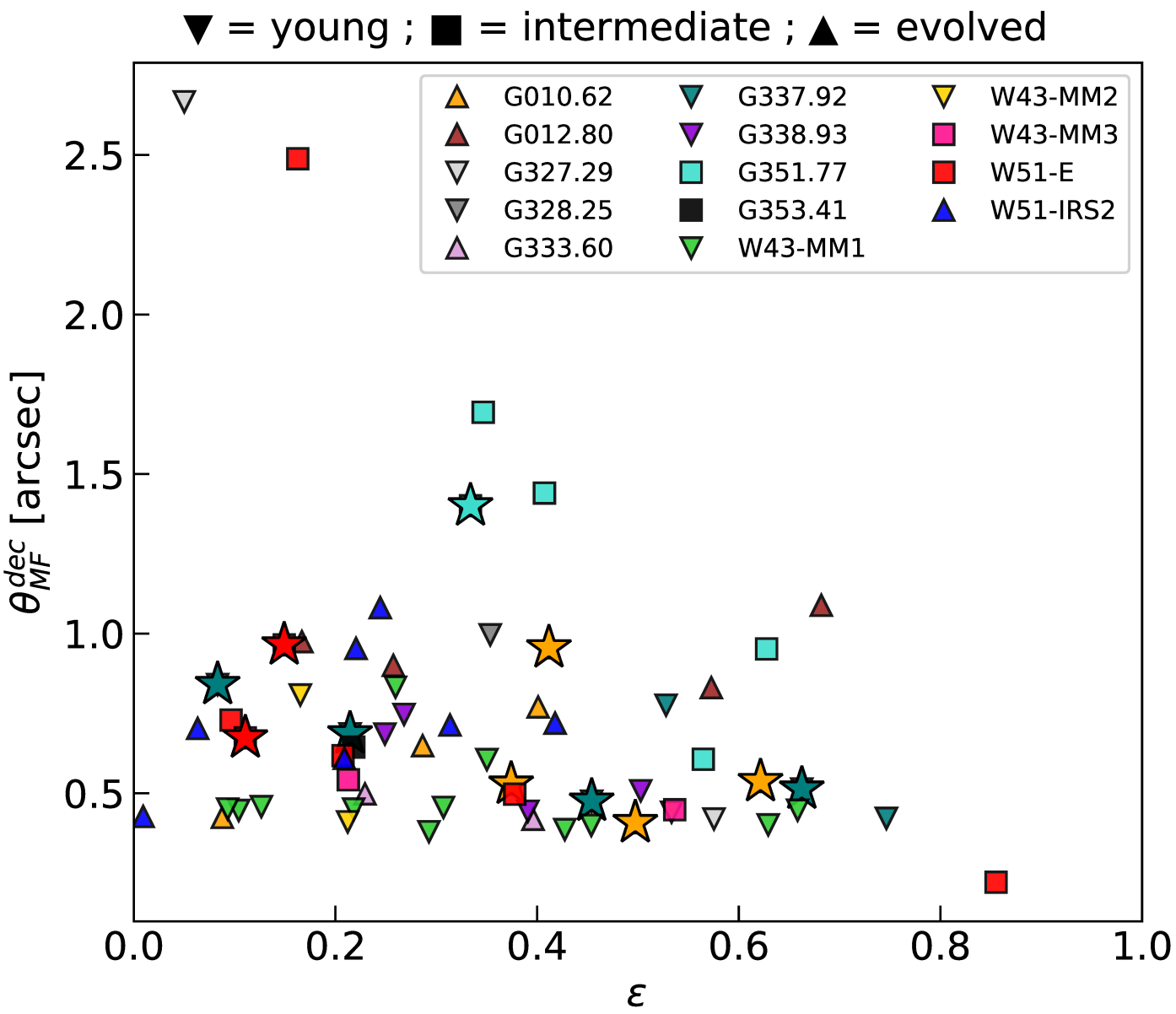

Fig. E.1: Methyl formate deconvolved source sizes ($\theta_{\rm MF}^{\rm dec}$) as a function of their ellipticity (ϵ). The different symbols represent the different evolutionary stages of the protoclusters: young, intermediate, or evolved, as shown on top of the figure. The methyl formate sources that are not associated with compact continuum cores are shown with stars. The sources for which $\theta_{\rm MF}^{\rm dec}$ is lower than half of the line cube beam size are not shown in the figure.